LUND UNIVERSITY

Experimental and Computational Analysis of Mode I Fracture in Wood

Likelihood-based inference and finite element model updating

Jonasson, Johannes

2025

Document Version:
Publisher's PDF, also known as Version of record

Link to publication

Citation for published version (APA):
Jonasson, J. (2025). *Experimental and Computational Analysis of Mode I Fracture in Wood: Likelihood-based inference and finite element model updating*. Division of Structural Mechanics, Lund university.

Total number of authors:
1

General rights
Unless other specific re-use rights are stated the following general rights apply:
Copyright and moral rights for the publications made accessible in the public portal are retained by the authors and/or other copyright owners and it is a condition of accessing publications that users recognise and abide by the legal requirements associated with these rights.
- Users may download and print one copy of any publication from the public portal for the purpose of private study or research.
- You may not further distribute the material or use it for any profit-making activity or commercial gain
- You may freely distribute the URL identifying the publication in the public portal

Read more about Creative commons licenses: https://creativecommons.org/licenses/

Take down policy
If you believe that this document breaches copyright please contact us providing details, and we will remove access to the work immediately and investigate your claim.

LUND UNIVERSITY

PO Box 117
221 00 Lund
+46 46-222 00 00

LUND
UNIVERSITY

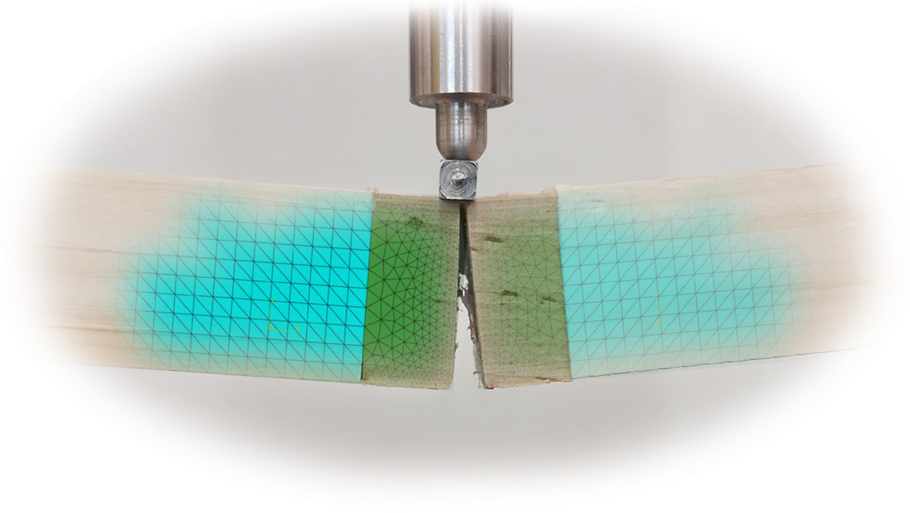

EXPERIMENTAL AND COMPUTATIONAL ANALYSIS OF MODE I FRACTURE IN WOOD

Likelihood-based inference and finite element model updating

JOHANNES JONASSON

Structural
Mechanics

Licentiate Dissertation

DEPARTMENT OF CONSTRUCTION SCIENCES
DIVISION OF STRUCTURAL MECHANICS

ISRN LUTVDG/TVSM--25/3083--SE (1-101) | ISSN 0281-6679
ISBN 978-91-8104-413-3 (Print) | 978-91-8104-414-0 (Pdf)
LICENTIATE DISSERTATION

EXPERIMENTAL AND COMPUTATIONAL ANALYSIS OF MODE I FRACTURE IN WOOD

Likelihood-based inference and finite element model updating

JOHANNES JONASSON

Copyright © 2025 Division of Structural Mechanics,
Faculty of Engineering LTH, Lund University, Sweden.
Printed by V-husets tryckeri LTH, Lund, Sweden, February 2025 *(Pl)*.

For information, address:
Div. of Structural Mechanics,
Faculty of Engineering LTH, Lund University, Box 118, SE-221 00 Lund, Sweden.
Homepage: www.byggmek.lth.se

Abstract

This thesis covers the estimation of the fracture behaviour of the European wood species Norway spruce and birch. The fracture behavior of wood can be quantified through three material parameters: the stiffness, the strength, and the specific fracture energy. In the present work, these parameters are characterized through two methods.

The first method is purely experimental and only estimates one parameter, by use of the so-called work-of-fracture method. In this procedure, a single-edge-notched beam is loaded in three-point-bending under stable crack propagation until complete failure. The specific fracture energy, i.e. the energy dissipated during the creation of a unit crack surface, can then be evaluated as the work carried out to complete fracture, divided by the fractured area. This method has previously been used in a large number of studies to establish the specific fracture energy of various wood species. In the present work, this experimental procedure is used to test 80 specimens, divided into four different series.

The second method employed is based on the same experimental tests, but in combination with numerical models. The difference between the numerically and experimentally obtained force-displacement responses is quantified in a so-called cost function, which further is minimized through a finite element model updating (FEMU) procedure using a Bayesian optimization framework, to establish the optimal set of material parameters. In addition, two commonly employed cost functions employed in FEMU are reformulated in the context of likelihood-based inference to estimate the uncertainty in the optimal set of parameters.

It is shown that neither of the two commonly employed cost functions can recover the variance in the experimental load-displacement curves. However, the mean behaviour is captured fairly well for both cost functions.

Keywords: fracture mechanics, finite element modeling, wood, cohesive zone modeling, finite element model updating, likelihood inference, optimization

Acknowledgements

The work presented in this thesis was conducted at the Division of Structural Mechanics, Lund University. The financial support from FORMAS, the Södra Foundation for Research, Development and Education, the ÅForsk Foundation, the Crafoord Foundation, and the Nils & Dorthi Troëdsson Foundation, are all gratefully acknowledged.

The people who have in some form or shape contributed with non-financial support to this thesis are (fortunately for me) too many to mention. However, a few mentions are necessary.

I am grateful to Josef Füssl for his hospitality during my research visit in Vienna, and to Sebastian Pech for his inspiring insights into computational mechanics and software development.

I also extend my deepest gratitude to my main supervisor, Henrik Danielsson, for his unwavering support and availability to always answer questions, even before I became a doctoral student. I also wish to thank my assistant supervisor, Erik Serrano. Both Henrik and Erik's responsive supervision has made the first half of this PhD project very enjoyable. Additionally, I want to thank Johan Lindström, assistant supervisor, for his patience when answering questions such as ”what is a convex hull?”, and for increasing the mathematical precision of this work. I also extend my appreciations to all my colleagues at the division for creating a great workplace.

To all my friends who have positively impacted my life and contributed to this thesis, implicitly or explicitly, I am deeply thankful.

Lastly, I express my love and gratitude to my mom, dad, and sister for providing me with a safe and happy upbringing filled with love. With each passing year, I become increasingly aware of how not everyone is as fortunate.

Johannes Jonasson, Lund, February 14th

Contents

Publication I

Fracture energy of birch in tension perpendicular to grain: experimental evaluation and comparative numerical simulations
Johannes Jonasson, Henrik Danielsson, Erik Serrano.
Wood Science and Technology 58(5), 1925-1949.
DOI: https://doi.org/10.1007/s00226-024-01595-6

Contributions
J. Jonasson: Conceptualisation, methodology, software, investigation, validation, writing—original draft, laboratory work.
H. Danielsson: Conceptualisation, methodology, investigation, writing—review and editing, and funding acquisition.
E. Serrano: Conceptualisation, methodology, investigation, writing—review and editing, and funding acquisition.

Publication II

Estimation of mode I fracture parameters in birch using likelihood-based inference
Johannes Jonasson, Johan Lindström, Henrik Danielsson, Erik Serrano.
Unpublished manuscript.

Contributions
J. Jonasson: Conceptualisation, methodology, software, investigation, validation, writing—original draft, laboratory work.
J. Lindström: Conceptualisation, methodology, software, investigation, writing—review and editing.
H. Danielsson: Conceptualisation, methodology, investigation, writing—review and editing, and funding acquisition.
E. Serrano: Conceptualisation, methodology, investigation, writing—review and editing, and funding acquisition.

Other publications not part of thesis

Mitigating footfall-induced vibrations in cross-laminated timber floor-panels by using beech or birch

Johannes Jonasson, Peter Persson, Henrik Danielsson.
Journal of Building Engineering, 86(108751).
DOI: https://doi.org/10.1016/j.jobe.2024.108751

Contributions

J. Jonasson: Conceptualisation, methodology, software, investigation, validation, formal analysis, writing – original Draft.
P. Persson: Conceptualisation, methodology, investigation, validation, formal analysis, writing – original draft, funding acquisition.
H. Danielsson: Conceptualisation, methodology, investigation, validation, formal analysis, writing – review & editing, funding acquisition.

Part I

Introduction and Overview

1 Introduction

1.1 Background

The use of timber in structural applications has grown exponentially in recent decades, mainly due to the environmental benefits associated with the use of timber in construction. Timber is both renewable and acts as a carbon dioxide sink during the entire life cycle of a timber structure. These are clearly desirable properties in times when reducing emission of greenhouse gases is necessary.

Wood species can be divided into two groups based on anatomical differences: coniferous and deciduous species, often referred to as softwoods and hardwoods, respectively. In Sweden, most of the forest stock, around 80%, consists of the softwood species Scots pine and Norway spruce. Birch, which is the most abundant hardwood species in Sweden, makes up 13% of the stock (Sveriges Lantbruksuniversitet, 2022). Naturally, coniferous species have been utilized the most for structural purposes due to their abundance. In contrast, birch is currently mostly used for pulpwood, and to some extent for flooring and furniture. This, despite that increased stiffness and strength can be identified in birch, compared to pine and spruce. High strength and stiffness are in general appealing properties for construction materials, and thus birch could potentially contribute to structures with improved load-bearing capacity, material efficiency and a diverse selection of construction materials. Due to these reasons, the interest in using birch in structural applications has increased in recent years. However, using wood can still be detrimental to the environment, since the acquisition of timber is directly dependent on forestry. In other words, sustainable timber construction cannot be achieved without sustainable forestry.

A key component in sustainable forestry is biodiversity. The more biodiverse an ecosystem is the more resilient the ecosystem becomes against environmental fluctuations (Hong et al., 2022) induced by for example climate change. To promote the biodiversity of Swedish forests, growing forests with a broad mix of wood species might be a viable option; more than 900 living species (of which some are threatened) are in some way benefiting from both living and dead birch trees (Fahlvik et al., 2021). Consequently, deciduous species, such as birch, seem to play a crucial role in promoting a biodiverse forestry, and can thus by extension also promote biodiverse timber construction.

Various studies have examined the effect of hardwood species in structural applications in recent years. For example, the effect of using birch in glued laminated timber (GLT) and cross laminated timber (CLT) has been examined by Obernosterer et al. (2023), and the effect seems promising with respect to stiffness and strength. In addition, the mechanical behaviour of birch plywood has been investigated by Wang et al. (2022a, 2022b). The dynamic response of CLT slabs constructed entirely with birch was evaluated by Jonasson et al. (2024b), and the results indicated that the dynamic response, in terms of vibrations and frequency response, was reduced markedly compared to conventional CLT slabs made of Norway spruce.

Increased strength and stiffness are in general desirable properties in structural applications. However, this usually comes at the expense of increased brittleness, i.e. risk of abrupt, and possibly catastrophic failure, which clearly is undesirable. One typical cause of brittle failure in timber applications is tensile stresses perpendicular to grain. For example, stresses perpendicular to grain arise in beams with notches or holes (Thelandersson & Larsen, 2003, Chap 4). In such applications, sharp edges give rise to stress concentrations, which in turn may result in crack propagation along the grain. In addition, mechanical and adhesive joints also give rise to stresses perpendicular to grain. Beams with holes and notches, and mechanical joints are often essential for aesthetic or practical purposes. Consequently, despite the potential increase of strength and stiffness in birch, the failure behaviour of birch needs to be properly understood to ensure that load-bearing capacities can be properly assessed.

The failure behaviour of materials in terms of the ultimate load-carrying capacity is a problem of instability (Gustafsson, 1985). For example, slender columns may fail in a sudden manner due to large displacements. In steel, plastic hinges may form which are a consequence of another instability phenomena, large strains. However, as Gustafsson (1985) argues, the most common failure mechanism is likely fracture. Fracture is the separation of a solid into more than one part and is a field that has been subject to large efforts of research in the last 100 years.

The fracture behaviour of wood is mainly governed by three material parameters: the elasticity, E, the ultimate strength, f, and the energy that is dissipated during fracture, G_f (often called the specific fracture energy). These three parameters also characterize a materials' brittleness, which can be quantified by a parameter called *the characteristic length*. For perfectly brittle materials, the characteristic length is close to zero. For perfectly plastic material, the characteristic length is infinite. Material which are between these two extremes are generally referred to as *quasi-brittle*. Wood is often considered to be a quasi-brittle material. To fully understand the fracture behaviour of a given material, and how it impacts load-bearing applications, the parameters E, f and G_f needs to be established and well-understood. Another key component which is crucial to establish in quasi-brittle materials is the strain-softening behaviour, which is a function describing the diminishing stress carrying capacity of the material during increased crack opening deformation.

A commonly applied experimental method to evaluate the tensile strength and the stiffness is the so-called direct tension test. This method has been utilized in numerous studies to evaluate the stiffness and strength of various wood species. For example, Forsman et al. (2020) determined the stiffness and strength perpendicular to grain of unmodified and acetylated Scots pine with this method. Direct tension tests can also be utilized to determine the strain-softening behaviour of wood, which was shown by Boström in his doctoral thesis (Boström, 1992).

A commonly employed method to evaluate the specific fracture energy is a single edge notched beam (SENB) loaded in three-point-bending. The method was originally developed for steel and concrete, and later adapted for wood by Gustafsson (1988).

Several studies have used this method to evaluate the specific fracture energy of various wood species (Dourado et al., 2015, 2008; Forsman et al., 2021). In addition, the use of this method has been extended in a few studies, to not only estimate the fracture energy, but also the stiffness, strength and the strain-softening behaviour (De Moura et al., 2008; Dourado et al., 2008; Kunecký et al., 2024). In these previous studies, an optimisation problem has been formulated, where the difference between some experimental and numerical quantity is minimised. This methodology is usually referred to as finite element model updating (FEMU) (Chen et al., 2024). Estimating several parameters through the SENB method instead of only one is of great value since more knowledge about a given material can be acquired from a single test. However, the methods to estimate the parameters that have been proposed thus far for wood (De Moura et al., 2008; Kunecký et al., 2024) provide only deterministic estimates of the established parameters. Wood exhibits a large variability in mechanical behaviour, and a deterministic set of parameters is not sufficient to accurately predict and understand the failure behaviour in load-bearing applications. As such, further development of current methods to allow for capturing the variance of the fracture parameters would be greatly beneficial. This is the focus of the present work.

1.2 Aim and objectives

As mentioned in the previous section, using birch in load-bearing applications might be beneficial for several reasons. It could enhance load-bearing capabilities while simultaneously improving the biodiversity of Swedish forests and the sustainability of the timber construction industry. However, for birch to be used in such applications its fracture behaviour needs to be well understood. The aim of this thesis is to establish the fracture behaviour of birch in terms of the three previously introduced fracture parameters. In contrast to previous work, the aim of this thesis is to estimate a non-deterministic set of the fracture parameters in wood. To successfully achieve this, current experimental methods may need to be modified or improved. Therefore, the objectives of this work are as follows:

- Assess if the conventionally used SENB specimens are suitable for evaluating the specific fracture energy of birch. If birch exhibits a more brittle behaviour than spruce, modifications to the current experimental set-up might be needed.
- Develop a FEMU procedure based on the theory of statistical inference in order to assess the possibility to accurately capture the inherent variability in the constitutive parameters in wood.
- With the SENB specimens, estimate the specific fracture energy for both Norway spruce (*Picea abies*) and birch (*Betula pendula)* with the conventional work-of-fracture method.
- With the developed FEMU method, estimate strength and the stiffness of both Norway spruce and birch, in addition to the specific fracture energy.

1.3 Research approach and limitations

Wood is a material which may be characterized at many different levels (Dinwoodie, 2000, Chap 1). In the present work, the fracture behaviour of wood is studied solely at the *clear wood* level. At this level, the material is seen as homogeneous and continuous. In addition, imperfections like knots and fiber deviations are not considered. The aim is however to enable the propagation of the herein determined fracture behaviour to a semi-structural or structural system level.

In the present work, the fracture behaviour has been determined through two different methodologies, see Figure 1.1. Out of the two methods, the SENB method is likely the most used method, and this method has been employed in Paper I. With this method it is only the specific fracture energy that is estimated. As such, the SENB method is used to evaluate the specific fracture energy in mode I of both Norway spruce and birch, in the TL crack propagation system. Four different series of specimens are constructed, with two different geometries. In total, the specific fracture energy is estimated for 80 specimens.

The second method estimates two additional parameters through FEMU, in addition to the specific fracture energy. With this method, a numerical model is sequentially updated based on the minimisation of the difference between experimentally and numerically obtained load-displacement curves. The difference is quantified through a so-called *cost function*. With this approach, all three relevant fracture parameters can be estimated, as long as the cost function is sensitive to the estimated parameters. The formulation of the cost function is usually carried out in a straightforward manner, for example, through the least squares error between the measured experimental and numerical quantities.

In the present work, two commonly used cost functions in FEMU are reformulated in the context of *likelihood-based inference*. By assuming a statistical model of the difference between the experimental and numerical load-displacement curves, it is possible to determine an approximate statistical distribution of the parameters that are subjected to optimisation.

The determination of these approximate statistical distributions enables the analysis of load-bearing structures made from birch and the uncertainties stemming from the

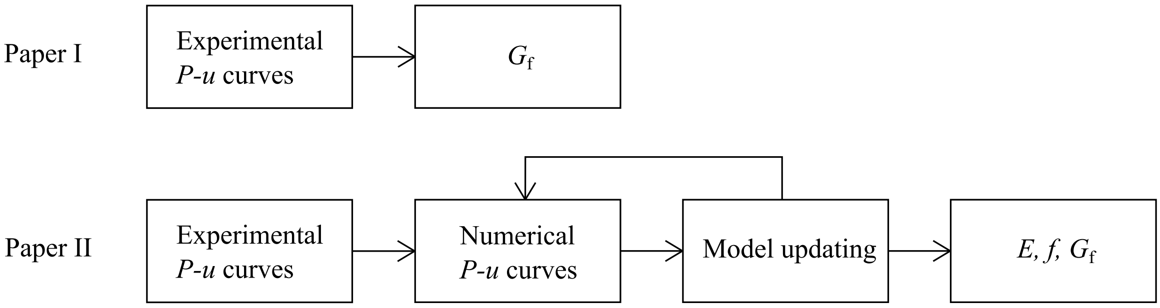

Figure 1.1: Flow-chart of the two different parameter estimation methods employed in the present work.

material variability. By propagating the estimated distributions of the parameters to the semi-structural or structural scale, studies at these scales can be carried out with realistic combinations of fracture parameters.

2 Wood for structural purposes

Given the numerous benefits of using wood in construction, it is no surprise that its use in structural applications dates back nearly 500 000 years (Barham et al., 2023). Wood is renewable, has a high strength-to-stiffness ratio, and is found aesthetically pleasing by many. In addition, the benefits of wood from an environmental perspective are convincing.

Structural wood is usually referred to as *timber*. In Sweden, the oldest preserved timber structure is from the 13th century (Gullbrandsson, 2010), and timber has for long been the dominating construction material in single-family dwellings and smaller multi-family dwellings. Buildings higher than two stories were not permitted in urban areas from 1874 up until 1994 by national building regulations. In the latter part of the 20th century, knowledge of timber increased, especially with respect to fire safety, which is crucial in timber structures, since timber is combustible. Conveniently, timber burns at a predictable rate, and it is thus possible to predict somewhat accurately when the structural integrity is compromised.

In addition to the problems with fire safety, wood suffers from several other drawbacks. For example, it is a lightweight material, making it prone to comfort issues due to vibrations and sound emissions. The mechanical behaviour is largely dependent on the moisture content, which might become problematic since wood can absorb large amounts of moisture. Absorption of moisture may also decrease durability and increase the risk for mold growth. It is also difficult to accommodate larger spans with timber structures, in comparison to steel and concrete. In addition, as mentioned in Chapter 1, timber is in general weak when stressed perpendicular to grain.

2.1 The micro- and ultrastructure of wood

The microstructure of all wood species is made up out of tube-like, hollow cells (Bodig & Jayne, 1982). The tube-like, hollow cells approximately run in the length direction of the tree trunk. The individual cells in softwoods are called tracheids. The tracheids have two tasks in the living tree: to transport water and to ensure the structural integrity of the tree. In hardwoods, the tasks related to structural integrity and moisture transport are carried out by two different cell types. The structural integrity is ensured by so-called fibers, whereas the water transport is carried out by vessels. In addition to tracheids, fibers and vessels, a cell called parenchyma is found both in softwoods and hardwoods. Its main task is to store nutrients.

The formation of the tracheids is different depending on what time of the year the cell growth takes place. During the early parts of the growing seasons, the wood cells grow relatively fast since the availability of water is usually high. In turn, this yields larger, more thin-walled tracheids. In contrast, the growth slows down during summer and the wood cells the grow during this time are denser and more thick-walled. The lighter, thin-walled part is called *earlywood*, whereas the denser part is called *latewood*. The denser latewood usually has a dominating effect on the mechanical behaviour of wood. This alternating, reoccurring growth, is what creates *growth rings* in wood.

In temperate climates, such as Europe, one growth ring per year is most often found, and the growth rings can thus be used to estimate the age of a tree. The identification of growth rings is in general easier in softwoods, since the tracheids in softwoods generally are organized in a regular and well-structured matrix-like pattern. In contrast, the organization of vessels, fibers and tracheids in hardwoods is less structured.

A single softwood tracheid consists of five different layers, illustrated in Figure 2.1c. The two outer layers, the primary wall (P) and the middle lamella (M) are generally lumped into one layer called the *compound middle lamella* (Bodig & Jayne, 1982, Chap 1). The three remaining layers, denoted S1, S2 and S3, are part of the secondary wall. The S2 layer has the largest influence on the macroscopic mechanical behaviour, since the so-called microfibrils are mainly oriented in the length direction of the tracheid in that layer. The thread-like microfibrils consist of molecular cellulose chains, which are embedded in a matrix of lignin and hemi-cellulose (Persson, 2000).

2.2 The macroscopic wood scale

Even though the microstructure of wood is crucial for understanding the mechanical behaviour, it is usually not the scale that is modeled or experimentally tested in civil engineering applications. Instead, the macroscopic scale is often of interest. The macroscopic scale can be divided further into two sub-scales. The first one, called the *clear wood scale*, includes wood at the growth ring level, but free from defects such as grain deviations and knots. The second one, the *structural scale*, is usually not considered free from defects. Growth rings are usually not explicitly modeled at either level and the material is thus considered to be homogeneous and continuous. In addition, wood is often considered to be defined by a rectilinear or a cylindrical coordinate system. Both coordinate systems are defined by the three principal directions of wood: the longitudinal direction, L, the radial direction, R, and the tangential direction, T. For a piece of wood (timber) that is cut far away from the pith, the assumption of a rectilinear coordinate system can be considered as quite accurate.

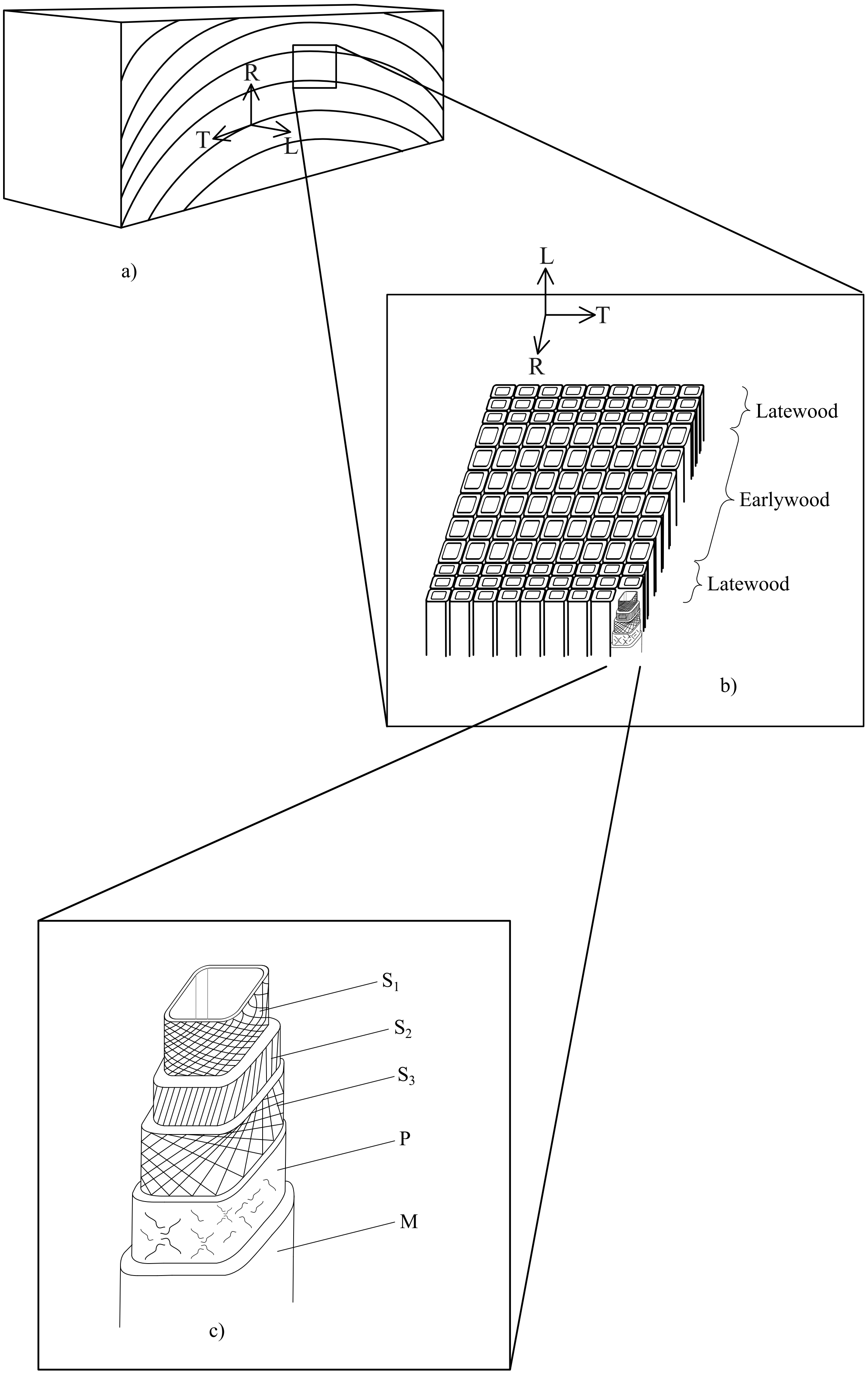

Figure 2.1: Illustration of (a) the growth rings on the macroscopic level, (b), the growth rings at the microstructural level and, (c), a single softwood tracheid cell, i.e. the ultrastructural level.

2.3 Constitutive modelling of wood

Consider a three-dimensional infinitesimal element cube with material orientations according to the three principal directions of wood: the longitudinal directions (or the fiber direction), denoted L, the radial direction, R, and the tangential direction, T, see Figure 2.2. For such a cube, three normal stresses and three shear stresses may be identified and subsequently collected in the so-called stress tensor, σ_{ij}, with the following components:

$$[\sigma_{ij}] = \begin{bmatrix} \sigma_{\mathrm{LL}} & \tau_{\mathrm{LR}} & \tau_{\mathrm{LT}} \\ \tau_{\mathrm{RL}} & \sigma_{\mathrm{RR}} & \tau_{\mathrm{RT}} \\ \tau_{\mathrm{TL}} & \tau_{\mathrm{TR}} & \sigma_{\mathrm{TT}} \end{bmatrix} \tag{2.1}$$

By moment equilibrium, it can be identified that $\sigma_{ij} = \sigma_{ji}$. The corresponding strains may be collected in the (small) strain tensor:

$$[\varepsilon_{ij}] = \begin{bmatrix} \varepsilon_{\mathrm{LL}} & \varepsilon_{\mathrm{LR}} & \varepsilon_{\mathrm{LT}} \\ \varepsilon_{\mathrm{RL}} & \varepsilon_{\mathrm{RR}} & \varepsilon_{\mathrm{RT}} \\ \varepsilon_{\mathrm{TL}} & \varepsilon_{\mathrm{TR}} & \varepsilon_{\mathrm{TT}} \end{bmatrix} \tag{2.2}$$

Similarly to the stress tensor, the strain tensor is also symmetric, such that $\varepsilon_{ij} = \varepsilon_{ji}$. Assuming linear elastic conditions, the relation between the stress and the strain tensor is linear according to Hooke's law:

$$\varepsilon_{ij} = C_{ijkl}\sigma_{ij}, \ \forall i,j = \{\mathrm{L,R,T}\} \tag{2.3}$$

where C_{ijkl} is the fourth order compliance tensor, which contains 21 unknowns. For orthotropic materials the number of unknowns is reduced to nine (Ristinmaa & Ottosen, 2005, Chap 4). By introducing Voigt notation, the tensors may be written as vectors, such that

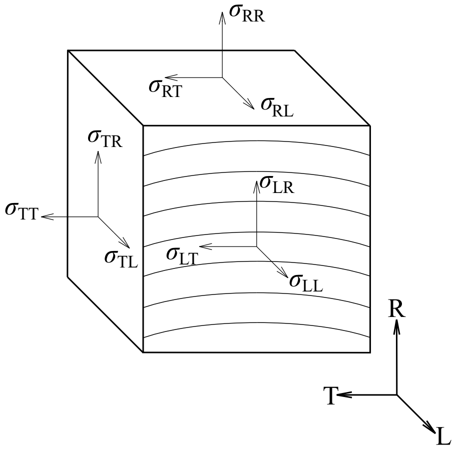

Figure 2.2: An infinitesimal wooden element cube.

$$
\begin{bmatrix} \varepsilon_{\mathrm{LL}} \\ \varepsilon_{\mathrm{RR}} \\ \varepsilon_{\mathrm{TT}} \\ \gamma_{\mathrm{LR}} \\ \gamma_{\mathrm{LT}} \\ \gamma_{\mathrm{RT}} \end{bmatrix}
=
\begin{bmatrix}
\frac{1}{E_{\mathrm{L}}} & \frac{-\nu_{\mathrm{RL}}}{E_{\mathrm{R}}} & \frac{-\nu_{\mathrm{TL}}}{E_{\mathrm{T}}} & 0 & 0 & 0 \\
\frac{-\nu_{\mathrm{LR}}}{E_{\mathrm{L}}} & \frac{1}{E_{\mathrm{R}}} & \frac{-\nu_{\mathrm{TR}}}{E_{\mathrm{T}}} & 0 & 0 & 0 \\
\frac{-\nu_{\mathrm{LT}}}{E_{\mathrm{L}}} & \frac{-\nu_{\mathrm{RT}}}{E_{\mathrm{R}}} & \frac{1}{E_{\mathrm{T}}} & 0 & 0 & 0 \\
0 & 0 & 0 & \frac{1}{G_{\mathrm{LR}}} & 0 & 0 \\
0 & 0 & 0 & 0 & \frac{1}{G_{\mathrm{LT}}} & 0 \\
0 & 0 & 0 & 0 & 0 & \frac{1}{G_{\mathrm{RT}}}
\end{bmatrix}
\begin{bmatrix} \sigma_{\mathrm{LL}} \\ \sigma_{\mathrm{RR}} \\ \sigma_{\mathrm{TT}} \\ \tau_{\mathrm{LR}} \\ \tau_{\mathrm{LT}} \\ \tau_{\mathrm{RT}} \end{bmatrix}
\tag{2.4}
$$

where the *engineering sheer strains* have been introduced according to

$$\gamma_{\mathrm{LR}} = \varepsilon_{\mathrm{LR}} + \varepsilon_{\mathrm{RL}} = 2\varepsilon_{\mathrm{LR}} \tag{2.5a}$$

$$\gamma_{\mathrm{LT}} = \varepsilon_{\mathrm{LT}} + \varepsilon_{\mathrm{TL}} = 2\varepsilon_{\mathrm{LT}} \tag{2.5b}$$

$$\gamma_{\mathrm{RT}} = \varepsilon_{\mathrm{RT}} + \varepsilon_{\mathrm{TR}} = 2\varepsilon_{\mathrm{RT}} \tag{2.5c}$$

Hooke's law can then be written in matrix form as:

$$\boldsymbol{\varepsilon} = \mathbf{C}\boldsymbol{\sigma} \tag{2.6}$$

where the inverse relation also holds

$$\boldsymbol{\sigma} = \mathbf{D}\boldsymbol{\varepsilon} \tag{2.7}$$

where $\mathbf{D} = \mathbf{C}^{-1}$, is the stiffness matrix.

3 Fracture mechanics

The birth of fracture mechanics is usually attributed to Alan Arnold Griffith's work published in 1921 (Griffith, 1921). Griffith observed that the experimental failure strength of glass was several orders of magnitude lower than the theoretically calculated inter-atomic bonding strength. By testing glass fibers with varying diameters, he noticed that when the diameter approached the limit of zero, the theoretical inter-atomic yield strength was also approached. He thus concluded that the failure strength must be governed by a size-effect, and classical failure theory, based on the ultimate tensile strength of the material, was not a sufficient failure criterion.

Based on his observations, Griffith formulated an energetic criterion to predict crack growth in ideally brittle bodies with a pre-existing sharp crack. He postulated that when the rate of reduction in potential energy with respect to a virtual crack increase is larger than the surface energy created by a new set of traction-free crack surfaces, the pre-existing crack will propagate. The reduction in potential energy when a crack is propagating a virtual distance s is called the *energy release rate* and is given by

$$G = -\frac{\partial \Pi}{\partial s} \tag{3.1}$$

where Π is the total potential energy of a solid body. When G reaches a critical value called *the critical energy release rate*, G_{c}, the crack propagates. In the coming decades, the field of linear elastic fracture mechanics (LEFM) was developed based on Griffith's postulate. In LEFM, three main modes of crack propagation can be identified, see Figure 3.1. Mode I is a pure opening mode, and generally the most common failure mode. Both mode II and III are shearing modes, with mode II being in-plane shear, and mode III being out-of-plane shear.

3.1 Linear elastic fracture mechanics

In LEFM, the body that is subjected to crack propagation is assumed to be ideal elastic. In addition, no upper limit on the stresses or strains are enforced. This causes stress and strain singularities to occur around the crack tip in the body, as illustrated in Figure 3.1 (right). This is clearly not physically reasonable, and means that single point stresses and strains can not be used to evaluate crack propagation. Instead, other quantities have to be used, for example the energy as in the previously described approach, which often is called *the energetic approach.* In addition, LEFM assumes that a crack is already existing in the body *a priori*, and can thus not be used to predict crack initiation, only crack propagation.

Another quantity often used to predict crack propagation in LEFM is *stress intensity*

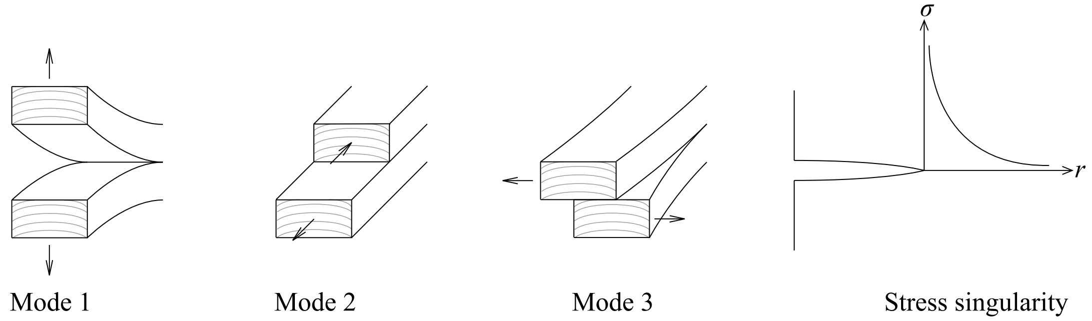

Figure 3.1: The three modes of fracture and an illustration of the stress singularity around the crack tip in LEFM.

factors, which were introduced by Irwin (1957). The stress intensity factors are usually expressed as a power series of several terms. Close to the crack tip, the first term of the power series dominates. The first term can be written by using a scaling factor, referred to as the stress intensity factor. One such factor for each mode of fracture can be defined and denoted by K_{I}, K_{II} and K_{III}:

$$K_{\mathrm{I}} = \lim_{r \to 0} \sigma_{\mathrm{I}}(r)\sqrt{2\pi r} \tag{3.2}$$

$$K_{\mathrm{II}} = \lim_{r \to 0} \sigma_{\mathrm{II}}(r)\sqrt{2\pi r} \tag{3.3}$$

$$K_{\mathrm{III}} = \lim_{r \to 0} \sigma_{\mathrm{III}}(r)\sqrt{2\pi r} \tag{3.4}$$

Here, r, is the distance away from the crack tip, see Figure 3.1 (right). At the crack tip, there is a stress singularity of type $1/\sqrt{2\pi r}$. Irwin (1957) tried to remedy the stress singularity, by limiting the stress ahead of the crack tip to the yield stress of the material. The extension of the plastic zone ahead of the crack tip could then be determined by equilibrium. However, the equilibrium considered only included the first term of the power series mentioned above. This assumption can only be valid close to the crack-tip, where this term approaches infinity, and thereby dominates the power series. Consequently, Irwin's approach limited the infinite stresses to the yield strength of the material, but the approach is only valid for cases when the plastic zone ahead of the crack tip is highly localized. This phenomenon of a highly localized plasticity zone ahead of the crack tip is referred to as *small-scale yielding* and is only valid for ideally brittle materials.

For wood, which is quasi-brittle, an assumption of small-scale yielding is in general not accurate, since the fracture process zone (FPZ) can be quite large in relation to characteristic dimensions of the structure. The fracture process zone here refers to the region around the crack-tip where the dissipation due to fracture takes place. For ideally brittle materials, i.e. in LEFM, it is assumed that all the dissipation essentially occurs in a single point, i.e. small-scale yielding discussed above. To remedy this, the concept of cohesive forces was first introduced by Barenblatt (1962). He assumed that there was a cohesive force some distance ahead of the crack tip. In contrast to Irwin (1957), who assumed that the stress ahead of the crack-tip was constant, Barenblatt modelled the stress ahead of the crack tip as varying with the width of the crack

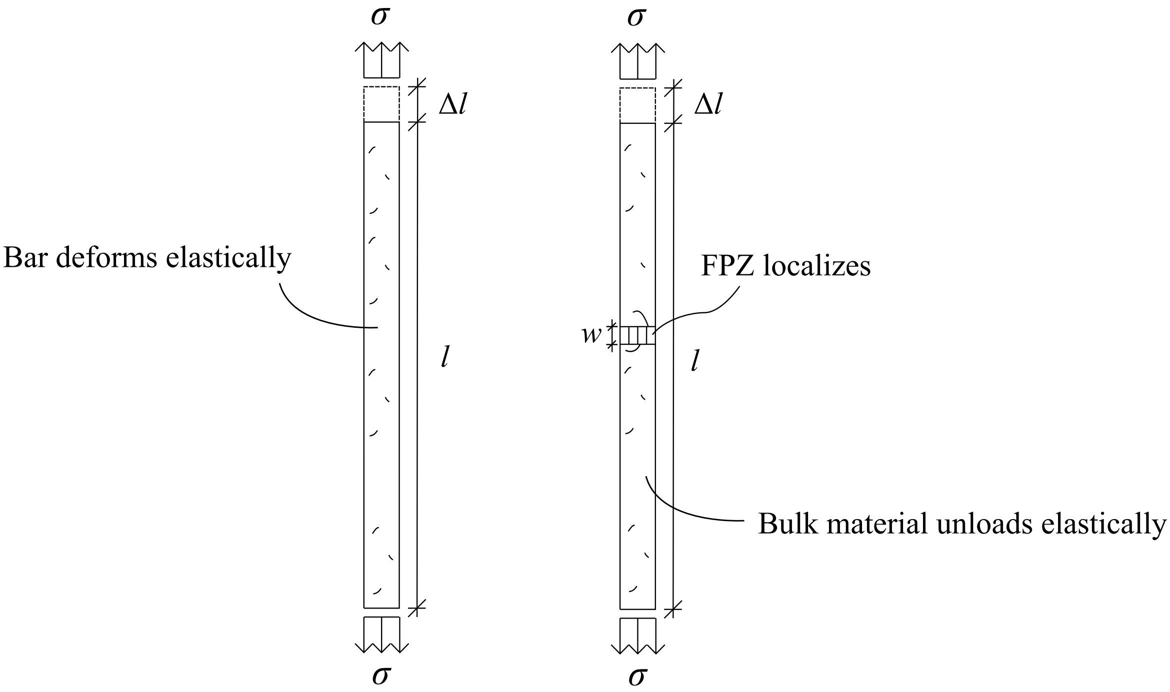

Figure 3.2: A bar loaded in uni-axial tension. Initially, the bar deforms elastically (right), but after the tensile strength has been reached, a fracture process zone localizes (left).

opening. However, Barenblatt never realized that this type of model could be used not only to predict crack propagation, but also crack initiation. To this end, Hillerborg et al. (1976) implemented the so-called *fictitious crack model* in combination with finite element models.

3.2 Non-linear fracture mechanics

The fictitious crack model introduced by Hillerborg et al. (1976) uses two constitutive relations for a body that undergoes fracture. A stress-strain (σ-ε) relation governs the response of the bulk material, whereas the response of the fracture process zone is governed by a stress-deformation (σ-w) relationship. The model is often conceptualized through studying a one-dimensional bar loaded in uni-axial tension, see Figure 3.2. The bar is assumed to have a uniform stress and strain distribution over its entire cross-section. As the bar is loaded, the elongation, Δl, is equal to:

$$\Delta l = \varepsilon l + w \tag{3.5}$$

where l is the initial length of the bar, ε is the elastic strain, and w is the deformation in the FPZ. Before the tensile strength has been reached, $w = 0$, and the total elongation of the bar is thus equal to the elastic elongation. When the tensile strength is reached, a *fracture process zone* localizes across the entire cross-section simultaneously, due to the assumption of a uniform stress- and strain distribution. The deformation of the localized FPZ is now governed by a stress-deformation relationship. As the bar un-

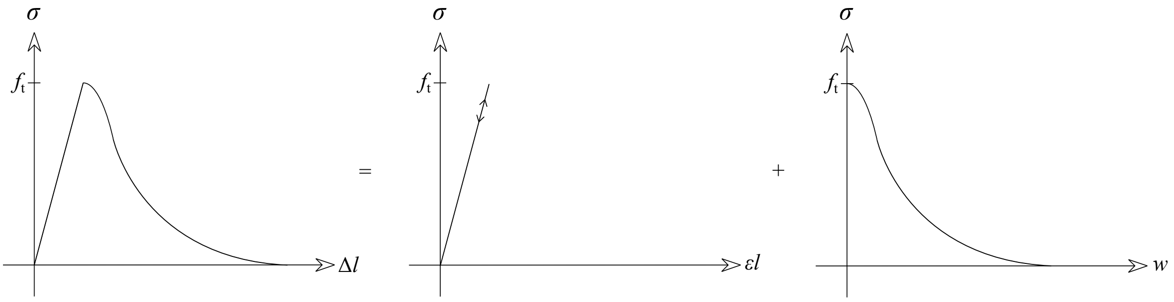

Figure 3.3: Load-displacement curve of the uni-axial bar in Figure 3.2. In the left part, global force-displacement response is shown. In the middle and right picture, the decomposition of the global force-displacement curve into the linear elastic bulk material and the FPZ is shown.

dergoes increasing deformation after peak-load, the deformation of the FPZ increases while the stress in the FPZ decreases. It should be noted that the material in the FPZ is not unloading, since w is increasing. Instead, the material in the FPZ is *softening*. In the elastic bulk material, both stresses and strains are elastically unloaded.

The area under the σ-w-curve is equal to the separation work per fractured unit area, often called the *specific fracture energy*. In the remainder of this work, the specific fracture energy may sometimes be referred to as just the *fracture energy*, and denoted G_f. The unit of the specific fracture energy is $[\mathrm{J/m^2}]$. The σ-w relationship is often called the *strain-softening* behaviour of the material and is assumed to be a material parameter. To properly understand how quasi-brittle materials behave during fracture, proper understanding of the strain-softening behaviour is crucial.

The shape of the strain-softening curve may be approximated in many ways, but the most common is arguably to assume a linear softening. The linear softening is uniquely defined by two parameters in theory, but three in practice. In theory, the two parameters are the specific fracture energy, G_f, and the ultimate strength, f_t. However, due to issues with convergence in numerical applications, a finite initial stiffness, here denoted k_init, must be introduced in the σ-w relation, instead of the theoretical infinite stiffness (see Figure 3.3 (right)). Other types of common strain-softening behaviours include bi-linear softening, piece-wise multi-linear softening and various forms of exponential softening, however, the present work is constrained to simply linear softening. In recent times, the fictitious crack model is often referred to as a *cohesive zone model* (CZM).

3.3 Experimental fracture mechanics

The orthotropic nature of wood means that the fracture behaviour is different in different directions, both due to the mode of loading, but also due to the orientation of the material. Six different crack propagation systems may be identified in wood, see Figure 3.4. They are denoted LR, RL, TL, LT, RT and TR. The first letter denotes the direction perpendicular to the crack plane, whereas the second letter denotes the direction of crack propagation. In addition, each propagation system may be loaded in

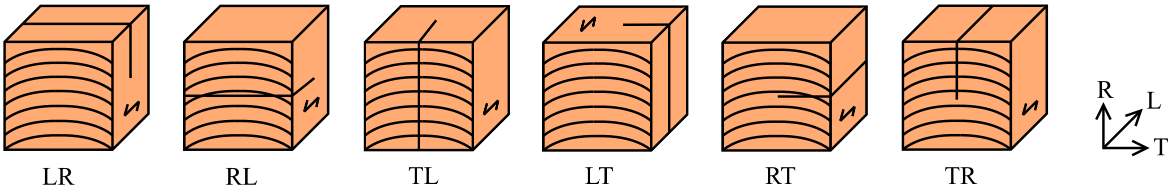

Figure 3.4: The six different crack propagation systems in wood.

different modes of loading, or combinations of different modes of loading. Generally, wood is weak when stressed perpendicular to grain, and thus it is the TL and RL crack propagation systems that have been the main focus of the wood fracture mechanics community.

Different experimental methods have been developed to determine the fracture behaviour of wood in various propagation systems. Originally, most methods were developed for steel and concrete, but later adapted for wood. For example, numerous studies have been carried out with the double cantilever beam (DCB), see Figure 3.5a) (De Moura et al., 2008; Todorović et al., 2023; Yoshihara & Kawamura, 2006) and the modified version of the same beam, the tapered double cantilever beam (TDCB) (De Moura & Dourado, 2018).

Another popular method is the wedge splitting test which has been employed in a number of studies. Various specimen geometries can be used to determine the fracture behaviour through a wedge splitting test, but a common choice is illustrated in Figure 3.5, which is a modification of a compact tension (CT) specimen. For example, Stanzl-Tschegg et al. (1995) studied the fracture behaviour of spruce in the TL- and RL-propagation systems by means of a wedge splitting test. They characterized the critical energy release rate, the specific fracture energy, and cohesive laws for both propagation systems. In addition, they studied the difference between using LEFM and non-linear fracture mechanics, showing the infeasibility of the former for small wood specimens which in general cannot be characterized as ideally brittle. The mean values of the fracture energy were determined to 240 and 150 J/m^2, for the RL and TL-propagation systems, respectively. They also determined the tensile strengths in the radial and tangential directions. In the radial direction, the mean value of the tensile strength was found to be 2.8 MPa, and in the tangential direction 1.7 MPa.

The fracture behaviour of spruce, alder, oak and ash (the three latter are hardwoods) were studied by Reiterer et al. (2002), in the TL and RL-propagation systems, using a wedge splitting test. Unstable crack propagation was identified for all hardwood species, whereas the crack propagation for the spruce specimens was stable. For the spruce specimens, the fracture energy was found to be 337 J/m^2 in the RL-system and 213 J/m^2 in the TL-system.

Reiterer (2001) also determined the fracture energy of spruce at different temperatures in the RL-crack propagation system. For a temperature equal to 20 °C, the fracture energy in mode I was evaluated to 180 J/m^2. By acoustic emission techniques, Reiterer et al. (2000) also determined the mode I fracture energy in the RL-propagation system for spruce. In that study, the specific fracture energy was evaluated to 260 J/m^2.

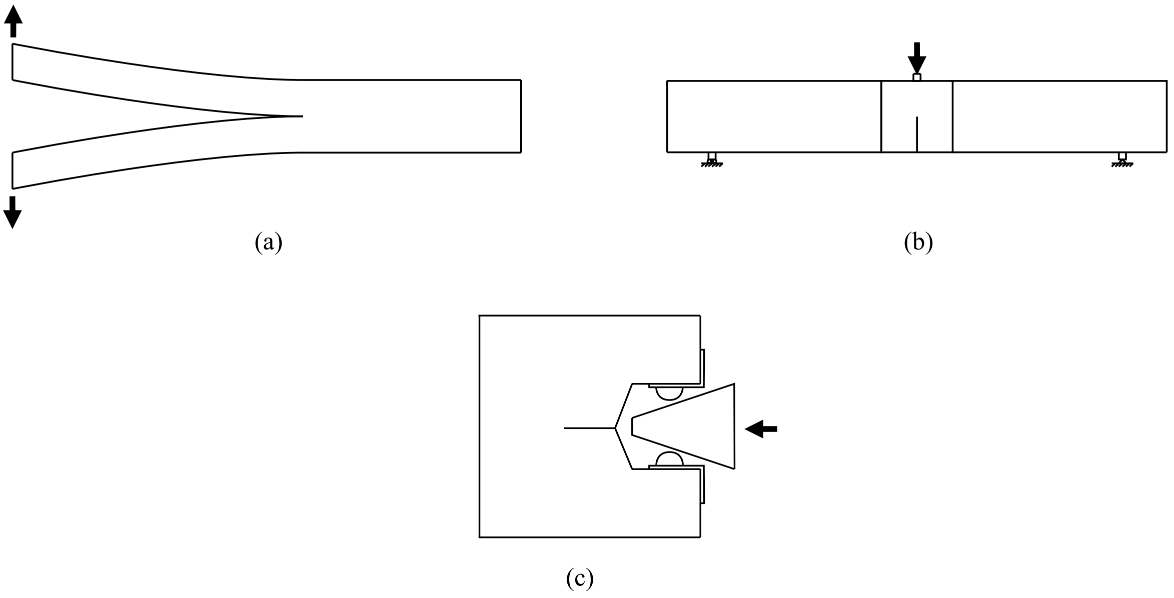
(a) (b) (c)

Figure 3.5: (a) Double cantilever beam, (b) single-edge-notched bream loaded in three-point-bending, and (c) wedge splitting test.

The fracture energy of different wood species has also been studied by using single-edge-notched beam (SENB) specimens, which have been modified and adopted to wood in the Nordtest standard (Nordtest, 1993). The method is arguably very convenient to use when evaluating the specific fracture energy, since no monitoring of crack-extension nor of crack-opening is needed. Instead, the force and the displacement at the load introduction point are the only needed quantities. The specific fracture energy can then be evaluated as the area under the load-displacement (P-u) curve, divided by the area of the fracture surface, A_c:

$$G_\mathrm{f} = \frac{1}{A_c} \int P(u)\ du \tag{3.6}$$

To accurately evaluate the fracture energy, the recorded load-displacement curves need be stable. That is, no sudden large jumps in the force can be present. If this objective is not achieved, the results might be misleading (Boström, 1992).

SENB specimens were used by Riberholt et al. (1992) to evaluate the fracture energy of spruce to 298 J/m^2, in the TL-crack propagation system. Similarly, it was evaluated to 293 J/m^2 by Stefansson (2001), in the same propagation system. Another study was carried out by Dourado et al. (2015), which determine the specific fracture energy in the TL-crack propagation system to 150 J/m^2.

SENB specimens were also used to evaluate the fracture energy in several hardwood species, for example by Forsman et al. (2021). In that study, the fracture energy of Scots pine and birch at different moisture levels was studied under mode I loading in the TL-crack propagation system. At a relative humidity of 70% (corresponding to a moisture content of 13.6%) the fracture energy was evaluated to 460 J/m^2 for the birch specimens.

4 Parameter estimation

4.1 Finite element model updating

In engineering sciences, solving for the response of a model for which the initial conditions are known constitutes a *forward problem*. The opposite problem, i.e. to calculate the initial conditions given the response of the model, may be denoted *an inverse problem*. If the initial conditions are relatively few, the procedure may be referred as *parameter estimation* (Aster et al., 2013). In addition, if the model is a finite element model, the name *finite element model updating* (FEMU) is often used (Chen et al., 2024). In mathematical notation, the output of the model may be denoted $y_{\mathcal{M}}$ and formulated as:

$$y_{\mathcal{M}} = \mathcal{M}(\mathbf{x}) \tag{4.1}$$

where the model, $\mathcal{M}(\mathbf{x})$, is a function of a set of input parameters collected in a *feature vector*, denoted $\mathbf{x}$. The input parameters, or features, may for example be geometrical parameters or material parameters. Based on this notation, the forward problem constitutes solving for the response $y_{\mathcal{M}}$ given a certain set of mechanical and/or geometrical parameters, $\mathbf{x}$. In contrast, the inverse problem constitutes finding the set of parameters $\mathbf{x}$, given the model response $y_{\mathcal{M}}$.

Parameter estimation in finite element (FE) modelling usually consists of calibrating a model after experimentally measured quantities, for example the global force response or local strain fields. The difference between the physical and numerical quantity is quantified in a *cost function*, often also called an *objective function*, or a *loss function*. In the present work, such a function will from now on be referred to as a *cost function*. The cost function, denoted $f(\mathbf{x})$, may further be minimised to find the optimal set of parameters, such that

$$\hat{\mathbf{x}} = \operatorname{argmin} f(y_{\mathcal{M}}(\mathbf{x}) - y_{\mathcal{E}}) \tag{4.2}$$

where $\hat{\mathbf{x}}$ denotes the optimal set of parameters and $y_{\mathcal{E}}$ denotes the experimental quantity of interest. Cost functions in FEMU may be divided into two major groups: *global* and *local* cost functions. Global cost functions are constructed based on measured global physical quantities, such as the global force-response. Local cost functions are based on local quantities, such as strain fields, that are usually captured with digital image correlation (DIC) software. In addition, global and local cost functions may be combined to account for both local and global phenomena.

One of the most common force-based cost functions is the least squares error between the numerical model and the experiments:

$$f(\mathbf{x}) = \sum_{j=1}^{N} (P_{\text{num},j}(\mathbf{x}) - P_{\text{exp},j})^2 \tag{4.3}$$

Here, $P_{\text{num},j}$, refers to the numerically obtained force at a given displacement, and $P_{\text{exp},j}$, refers to the experimentally obtained force given at the same displacement. This cost function may also be modified by some normalisation factor, $P_{\text{norm},j}$, such that:

$$f(\mathbf{x}) = \sum_{j=1}^{N} \left(\frac{P_{\text{num},j}(\mathbf{x}) - P_{\text{exp},j}}{P_{\text{norm},j}} \right)^2 \tag{4.4}$$

The normalisation factor may for example be the point-wise standard deviation captured in the experiments.

The minimisation problem described in Equation 4.2 may be solved with various optimisation methods, for example gradient-based methods. During certain conditions, such as *convexity* and *compactness*, such methods converge relatively quickly. In addition, implementations of many gradient-based optimisation methods are readily available in popular programming languages, such as Matlab (MATLAB, 2022) and Python (Van Rossum & Drake Jr, 1995). A clear drawback with such methods is that they rely on the evaluation of first- and second-order derivatives of the cost function, which may be computationally expensive if the cost function is not analytically tractable.

To reduce the dependency on gradient and Hessian evaluations, different derivative-free optimisation methods have been developed. For example, genetic algorithms, the Nelder-mead (simplex) algorithm and Bayesian optimisation exist, all which are methods that have been used in FEMU and inverse parameter estimation in recent years.

Regardless of whether a gradient-based or derivative-free optimisation method is used, evaluation of the cost function in FEMU is generally computationally expensive. In addition, the number of simulations available may be limited, both with respect to time and computational power. Indeed, when carrying out inverse procedures such as FEMU, it is often of interest to reduce the number of simulations as much as possible. To this end, Bayesian optimisation (BO) is a well-established technique (Brochu et al., 2010; Garnett, 2023; Regis & Shoemaker, 2005; Shahriari et al., 2016).

4.2 Bayesian optimisation

BO can be seen as an optimisation algorithm which sequentially samples the cost function, $f(x)$, at the most optimal location to solve the optimisation problem in Equation 4.2. The most optimal location is chosen based on combining the knowledge from all previous iterations through an *acquisition function.* The acquisition function is usually constructed based on a Gaussian process (GP), denoted $g(x)$, which approximates the cost function. The GP and the acquisition function are thus sequentially updated at each iteration, based on all observations of the cost functions thus far. The data-set, which may initially be empty, is at iteration i denoted $\mathcal{D}_i$. The sequential procedure is carried out until termination, which usually is determined by max number of function evaluations in BO. A pseudo-algorithm of the BO procedure is shown in Algorithm 1.

Algorithm 1 Pseudo-algorithm for Bayesian optimisation.

```
Input: $f(\mathbf{x}),\ \mathcal{D}_i,\ \alpha(\mathbf{x}),\ n_{\max},\ n_{\text{pre}}$
  Sample $n_{\text{pre}}$ points $\mathbf{x}_i,\ i = 1, \dots, n_{\text{pre}}$
  Create $\mathcal{D} = \bigcup_{i=1}^{n_{\text{pre}}} \{\mathbf{x}_i, f(\mathbf{x}_i)\}$
  $i \leftarrow n_{\text{pre}}$
  while $i < N_{\max}$ do
      Use $\mathcal{D}$ to create GP approximation, $g(\mathbf{x})$, and acquisition function $\alpha(\mathbf{x})$.
      $x_{i+1} \leftarrow \operatorname{argmin} \alpha(\mathbf{x})$
      $y_{i+1} \leftarrow f(\mathbf{x}_{i+1})$
      $\mathcal{D} \leftarrow \mathcal{D} \cup \{x_{i+1}, y_{i+1}\}$
      $i \leftarrow i + 1$
  end while
```

Gaussian process regression

A Gaussian process, g, is a stochastic process which is completely defined by its mean function and its covariance function, such that

$$g \sim \mathcal{GP}(m(\mathbf{x}), k(\mathbf{x}, \mathbf{x}')) \tag{4.5}$$

where $m(\mathbf{x})$ is the *mean function* and $k(\mathbf{x}, \mathbf{x}')$ is the *covariance function*. Here, $\mathbf{x}$ and $\mathbf{x}'$ denotes two (potentially different) feature vectors, where each feature vector has n_{dim} elements. The covariance function will be specified in detail in the next section.

The Gaussian process, g, may be distorted by some additive noise, which often is independent and identically distributed. Assuming the noise is Gaussian distributed with a zero mean, the i:th observation y_i may be denoted as:

$$y_i = g(\mathbf{x}_i) + \epsilon, \qquad \epsilon \sim \mathcal{N}(0, \sigma_n^2) \tag{4.6}$$

Here $\mathbf{x}_i$ is the feature vector of the i:th observation. In the case of exact observations, $\sigma_n = 0$, and the observation is equal to the process, such that

$$y_{\text{i}} = g(\mathbf{x}_i) \tag{4.7}$$

Now, assume that a number of observations, denoted n, have been made of the process. For each observation, there exists a feature vector $\mathbf{x}_i$. To each feature vector, there exists a corresponding observed function value, y_i. All function values may be collected in a column vector $\mathbf{f}$, called *training values*, and all feature vectors (called *training points*) may be collected in a matrix $\mathbf{X}$, such that:

$$\mathbf{f} = \begin{bmatrix} y_1 & y_2 & \dots & y_n \end{bmatrix}^\mathsf{T} \tag{4.8a}$$

$$\mathbf{X} = \begin{bmatrix} \mathbf{x}_1 & \mathbf{x}_2 & \dots & \mathbf{x}_n \end{bmatrix}^\mathsf{T} \tag{4.8b}$$

Thus, $\mathbf{f}$ is a vector of dimension $n \times 1$, and $\mathbf{X}$ is a matrix of dimension $n \times n_{\text{dim}}$. Here $\bullet^\mathsf{T}$ denotes the transpose of a matrix or a vector. Further, by using the knowledge in $\mathbf{X}$ and $\mathbf{f}$, it is of interest to make predictions for a new set of feature vectors, called *test points*, which are collected in a matrix $\mathbf{X}_*$. For now, it is assumed that predictions are carried out for a single test point, such that $\mathbf{X}_* = \mathbf{x}_*$. In this point, we wish to learn about the unknown function value. We call this unknown function value our *test value* and denote it $g(\mathbf{x}_*)$. $g(\mathbf{x}_*)$ is an approximation of the cost function in the test point, such that $g(\mathbf{x}_*) \approx f(\mathbf{x}_*)$. The joint Gaussian distribution between all training points and the test point may now be defined as:

$$\begin{bmatrix} \mathbf{y} \\ g_* \end{bmatrix} \sim \mathcal{N}\left(\mathbf{0}, \begin{bmatrix} \mathbf{K}_y & k(\mathbf{X}, \mathbf{x}_*) \\ k(\mathbf{X}, \mathbf{x}_*)^\mathsf{T} & k(\mathbf{x}_*, \mathbf{x}_*) \end{bmatrix}\right), \quad \mathbf{K}_y = k(\mathbf{X}, \mathbf{X}) + \sigma_n^2 \mathbf{I} \tag{4.9}$$

where a zero mean prior has been assumed. Based on the joint Gaussian distribution, the posterior distribution for the test point is:

$$g_* | \mathbf{X}, \mathbf{y}, \mathbf{x}_* \sim \mathcal{N}(\mu(\mathbf{x}_*), \sigma^2(\mathbf{x}_*)) \tag{4.10}$$

where

$$\mathbb{E}[g_* | \mathbf{X}, \mathbf{y}, \mathbf{x}_*] = \mu(\mathbf{x}_*) = k(\mathbf{X}_*, \mathbf{X}) \mathbf{K}_y^{-1} \mathbf{y} \tag{4.11a}$$

$$\mathbb{V}[g_* | \mathbf{X}, \mathbf{y}, \mathbf{x}_*] = \sigma^2(\mathbf{x}_*) = k(\mathbf{x}_*, \mathbf{x}_*) - k(\mathbf{x}_*, \mathbf{X}) \mathbf{K}_y^{-1} k(\mathbf{X}, \mathbf{x}_*) \tag{4.11b}$$

$\mu(\mathbf{x}_*)$ is thus the approximation of the cost function, $f(x)$, in the test point $\mathbf{x}_*$, and $\sigma^2(\mathbf{x}_*)$ is the standard deviation (i.e. the uncertainty) of the approximation of the cost function in the same test point.

Covariance functions

The covariance function was previously introduced in Equation 4.5, as a function that takes two feature vectors as inputs. However, in the most general case, the arguments to the covariance function may be two (potentially different) sets of feature vectors. For now, we will assume that the two sets are the same. The set may for example be the set previously denoted as $\mathbf{X}$ of dimension $n \times n_{\text{dim}}$. For two such (potentially different) sets, the covariance function evaluates the covariance for all combinations of rows in $\mathbf{X}$. This results in a covariance matrix of dimension $n \times n$, where the element at location i, j is the covariance between the i:th and j:th feature vectors:

$$k(\mathbf{X},\mathbf{X}) = \Sigma \tag{4.12}$$

$$k(x_i,x_j) = \Sigma_{ij} \tag{4.13}$$

A covariance function is called stationary if it is a function of a measure of distance, r:

$$r = \sqrt{(\mathbf{x}-\mathbf{x}')^\mathsf{T}\mathbf{A}(\mathbf{x}-\mathbf{x}')} \tag{4.14}$$

Here, $\mathbf{A}$, is a positive definite matrix which allows for scaling the distance in specific directions. If $\mathbf{A} = \mathrm{diag}(\mathbf{l}^{-2})\mathbf{I}$, the kernel is an axis-aligned anisotropic kernel. If $\mathbf{A} = l^{-2}\mathbf{I}$, an isotropic kernel is acquired, where the length-scale factor is the same in every direction. One of the most common covariance functions is the squared exponential (SE) covariance function, which may also be called the Gaussian covariance function, and is given by the following expression:

$$k(r) = \sigma_v^2 \exp\left(-\frac{1}{2}\frac{r^2}{\rho^2}\right) \tag{4.15}$$

Here σ_v^2 is the signal variance and ρ is a general length-scale parameter which in the following is set to one since length-scale factors are already included in $\mathbf{A}$. The SE covariance function suffers from the drawback of being infinitely differentiable and thus results in a smooth process. Despite this, the SE covariance function is most likely the most used covariance function in applications of GPs. An alternative to the SE covariance function is the Matérn covariance function (Matérn, 1986) which is given by

$$k(r) = \sigma_v^2 \frac{2^{1-\nu}}{\Gamma(\nu)}\left(\sqrt{2\nu}r\right)^{\nu} K_\nu\left(\sqrt{2\nu}r\right) \tag{4.16}$$

where K_ν is a modified Bessel function of the second kind, and $\Gamma(\nu)$ is the Gamma function. Here, ν, is a strictly positive, non-zero, smoothness parameter, which enables the possibility to model different levels of smoothness. In practical applications, this parameter is often taken as a half integer, such that $\nu = k + \frac{1}{2}$ for $k \in \mathbb{Z}$. The covariance function then reduces to a convenient polynomial form, and is solely a function of the distance, r. Two values of ν often adopted in the machine learning community are $\nu = \frac{3}{2}$ and $\nu = \frac{5}{2}$, for which the Matérn covariance function takes the following two forms:

$$k_{\nu=3/2}(r) = \sigma_v^2(1+\sqrt{3}r)\exp(-\sqrt{3}r) \tag{4.17a}$$

$$k_{\nu=5/2}(r) = \sigma_v^2(1+\sqrt{5}r+\frac{5}{3}r^2)\exp(-\sqrt{5}r) \tag{4.17b}$$

Acquisition function

As mentioned previously, the task of the acquisition function is to determine where to sample the cost function next. This choice is often carried out by combining the knowledge of the posterior mean, Equation 4.11a, and the uncertainty around the posterior mean, i.e. the posterior variance, Equation 4.11b. An acquisition function is thus minimized in order to estimate the next sample point. A common acquisition function is the lower confidence bound (LCB) acquisition function:

$$\alpha_{\text{LCB}}(\mathbf{x}_*) = \mu(\mathbf{x}_*) - \sqrt{\beta}\sigma^2(\mathbf{x}_*)) \tag{4.18}$$

Here, β is a factor which weighs the mean against the uncertainty. If $\beta = 0$, no uncertainty is considered when determining the next sample point. If $\beta > 0$, regions with uncertainty are given more weight, in turn favouring exploration of the cost function, i.e. sampling in regions where previous samples are scarce.

Likelihood-based inference

It is clear that a material which has formed naturally displays a rather large variation in constitutive behaviour. In wood, this variability is apparent on all system levels, and it is often of interest to quantify this variation to fully understand the material. In statistical modelling, it is common that some experiment is carried out, and observations of a (often stochastic) variable is made. Based on the observations, it is desirable to make predictions that are more general, and as stated by Pawitan (2013):

> We say we wish to ’infer’ something from the data.

This inference can be carried out with *likelihood-based inference*. In likelihood-based inference, the likelihood, a concept coined by Fisher (1922), plays a central role. The likelihood is defined as follows (Pawitan, 2013):

Definition of Likelihood. *Assuming a statistical model parameterized by a fixed and unknown x, the likelihood $L(x)$ is the probability of the observed data considered as a function of x.*

In other words, the likelihood is a function that describes how likely a certain parameter set is to have generated the observed data. Given a formulated likelihood, denoted $L(x)$, the optimal parameter, $\hat{x}$, may then be determined by *maximum likelihood estimation* (MLE). In practice, the MLE is carried out for the *log-likelihood*, which is denoted $l(x) = \log L(x)$. If certain regularity conditions are fulfilled, the second derivative at the MLE can be used to reason about the uncertainty of $\hat{x}$ (Pawitan, 2013). To this end, a *score function* is defined as the first derivative of the log-likelihood, such that

$$S(x) = \frac{\partial l(x)}{\partial x} \tag{4.19}$$

The MLE of x is then given by setting the score function to 0. Further, the curvature, $I(x)$, is defined as the negative second derivative of the log-likelihood, evaluated at the MLE, such that:

$$I(\hat{x}) = -\frac{\partial^2 l(x)}{\partial x^2}\bigg|_{x=\hat{x}} \tag{4.20}$$

which is the observed *Fisher information* (FI). The variance of $\hat{x}$ may then be defined as the inverse of the observed FI:

$$\mathbb{V}(\hat{x}) = I(\hat{x})^{-1} \tag{4.21}$$

These concepts directly generalize to higher dimensions by replacing the first- and second derivatives with their higher-dimensional counterparts, i.e. the gradient and the Hessian. It should also be noted that this section has been using the term *maximum likelihood estimation*, meaning the log-likelihood is maximised. To maintain a minimisation problem, it is the *negative log-likelihood* that is minimised in the remainder of this work.

In the context of FEMU, the consequence of the score function and the Fisher information is the following. If the error (i.e. the cost function) that is minimised in FEMU is formulated as a proper statistical model, it is possible to, through MLE, both reason about the optimal set of parameters, and the uncertainty in the optimal set of parameters. Consequently, through the combination of FEMU and likelihood-based inference, it is possible to determine not only a deterministic set of optimal material parameters, but also their variance and covariance.

5 Overview, summary and outlook

The aim of the following chapter is to provide an overview of the scientific contributions of the present work. The contributions will for clarity be split up into three subsections. The first section will mainly cover the experimental campaign reported in Paper I (Jonasson et al., 2024a). The second section will focus on the estimation of the fracture behaviour in terms of the stiffness, strength and the fracture energy, covered in Paper II. The third section will provide a summary and an outlook for future work.

5.1 Experimental campaign

The experimental campaign reported in Paper I has been carried out with SENB specimens loaded in three-point-bending according to the Nordtest method (Nordtest, 1993), see Figure 5.1. With this method, the only two quantities that are needed in order to estimate the fracture energy are the load, P, and the displacement, u, at the load introduction point. The specific fracture energy can then be evaluated as the mechanical work carried out to completely fracture the specimen, divided by the area of the fracture surface. Depending on how the middle piece of the SENB specimen is oriented, the specific fracture energy may be evaluated for various crack propagation systems. In the present work, the aim has only been to characterize the fracture behaviour in the TL-crack propagation system (the reader is referred to Chapter 3 for an illustration of the different crack propagation systems in wood).

SENB specimens are most commonly manufactured with a rectangular fracture surface. This is also what is prescribed in the Nordtest standard. However, when the tested material exhibits high brittleness, this notch geometry might yield unstable

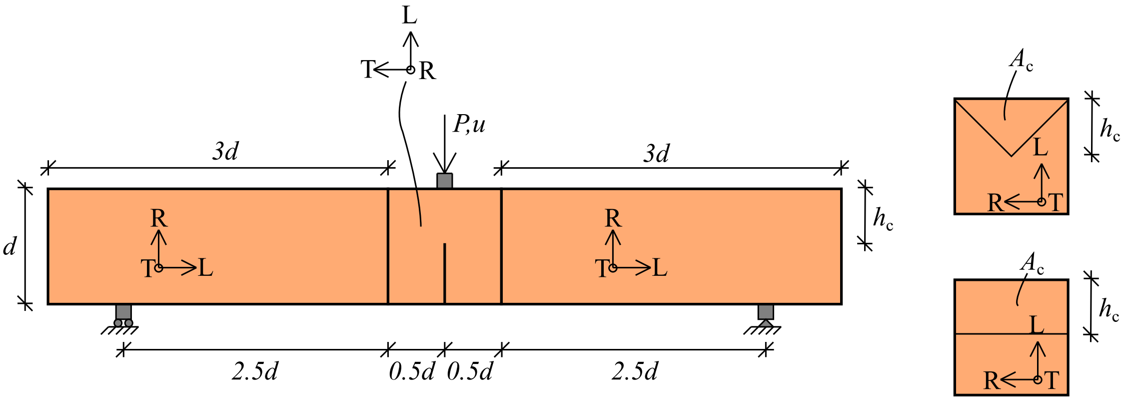

(a) (b)

Figure 5.1: (a) Experimental set-up of the SENB specimen and (b) the two different notch geometries.

crack propagation. This has been shown by Lai and Plönning (2019), where birch specimens with a rectangular fracture surface resulted in unstable crack propagation. To mitigate this, a triangular fracture surface has successfully been used by Forsman et al. (2021, 2020). The triangular fracture surface is often called a *chevron notch*, and is often employed for ceramics (Anderson, 1995), which generally exhibit very brittle fracture behaviour. An illustration of the two fracture surfaces is shown in Figure 5.1b. Theoretically, the shape of the fracture surface should not influence the evaluation of the specific fracture energy. However, this effect has not been studied exhaustively for wood. Thus, one of the main objectives of the experimental campaign has been to compare the evaluated specific fracture energy for the two different geometries of the fracture surface.

The second main objective of the experimental campaign was to characterize the specific fracture energy of birch and compare it to the specific fracture energy of Norway spruce. Although some studies have previously characterized the specific fracture energy of birch (Forsman et al., 2021) and spruce (Reiterer, 2001; Reiterer et al., 2002) separately, comparative studies are still scarce. In the present work, a rather extensive comparison of the fracture energy between the two different wood species is provided. In total, 80 specimens were tested, of which 41 specimens were spruce specimens and 39 specimens were birch specimens. For each species, the two different geometries of the fracture surfaces described above were adopted. As such, four series were tested in total.

The evaluated specific fracture energy for the four series is shown in Table 5.1. The mean specific fracture energy for all spruce specimens was evaluated to 222 J/m^2. This is a reasonable value compared to previous studies, which in general reports values ranging between 150 and 300 J/m^2, see Chapter 3. The evaluated mean specific fracture energy for all birch specimens was higher compared to what has been found in previous studies. However, it should be noted that comparable studies are very few. Nonetheless, Forsman et al. (2021) evaluated the specific fracture energy to 460 J/m^2. In the present work, the mean fracture energy for all birch specimens was determined to 657 J/m^2. Although this discrepancy is rather large, it can not be deemed to be outside the natural variation of the mechanical behaviour of wood, especially when considering that the comparison is made with only a single study. Further experimental investigations are recommended.

Table 5.1: Evaluated fracture energies for the our different test series. The fracture energy is expressed in J/m2^2. The coefficient of variation is shown in the paranthesis.

	Rectangular	Triangular	All
Spruce	188 (11%)	257 (14%)	222 (20%)
Birch	700 (17%)	611 (19%)	657 (19%)

Remarks on the effect of geometry of fracture surface

As mentioned previously, the type of fracture surface should not impact the evaluated specific fracture energy in theory, given an assumption of negligible plastic dissipation in the bulk material of the specimens. However, as seen in Table 5.1, a difference was observed in the present work. In addition, the difference was not consistent between the two different species. For the spruce specimens, using the triangular fracture surface resulted in a higher specific fracture energy compared to using the rectangular fracture surface. For the birch specimens, the inverse relation was found: the specimens with a triangular fracture surface yielded a lower specific fracture energy than the specimens with a rectangular fracture surface.

It is difficult to unambiguously determine the source of this discrepancy in evaluated fracture energy between the different geometries of the fracture surface. However, one reason that is discussed in Paper I is the manufacturing process. Overall, the manufacturing process of the specimens with a triangular fracture surface was deemed more difficult, which could induce inconsistent errors. Because of the manufacturing difficulties in combination with all specimens exhibiting more or less stable crack propagation, it was concluded that for estimating the specific fracture energy of birch (or spruce) in mode I loading, specimens with a triangular fracture surface are not necessary for the TL-crack propagation system. However, further studies with respect to how the notch geometry affects the evaluated specific fracture energy are recommended.

5.2 Estimation of fracture parameters

The aim of the work carried out in Paper II was manifold. The first objective was to reformulate two commonly used cost functions in FEMU based on the theory of likelihood-based inference. This reformulation is necessary if it is of interest to estimate the uncertainty in the parameters, and not only establish deterministic values. By using the FEMU procedure, the second objective was to establish the three relevant fracture parameter for both Norway spruce and birch: the tangential elastic stiffness, E_{T}, the tensile strength, f_{t}, and the specific fracture energy G_{f}, and assess if it is possible to accurately recover the variance from the experimental load-displacement curves.

Likelihood-based inference in finite element model updating

As described in Chapter 4, the cost function is of central importance in a FEMU procedure. In order to properly understand the cost functions adopted in the present work, this section starts by defining all relevant experimentally and numerically obtained quantities in a (hopefully) mathematical precise manner.

First, consider a single experimental series, for which several SENB specimens have been tested and hence several load-displacement curves have been acquired. The number of experimental load-displacement curves in a specific series is denoted n_k. Each load-displacement curve thus consists of a number of displacement values, and corresponding force values. The displacement values of different raw load-displacement curves do, in general, not align. This is a problem, since when comparing the numerically and experimentally obtained force, they need to be compared at the same displacement value. Thus, the raw, measured data is resampled (interpolated) so that the displacement values of all curves fall on the same grid. Each displacement point on the interpolated grid is referred to as a *discretisation point*, and denoted s_i. The total number of discretisation points of the uniform grid are denoted n_i. With this in mind, we introduce the term y_{ik}, which denotes the force in discretisation point s_i for the k:th experimental load-displacement curve.

In addition to the experimentally obtained force, the numerical model yields a numerical load-displacement curve which is dependent on the set of material parameters subjected to optimisation. These parameters are collected in a vector, and denoted $\mathbf{x}$. The numerical load-displacement curve is discretised in the same discretisation points as the interpolated experimental load-displacement curves. Thus, the force of the numerical model, based on the (known) set of material parameters $\mathbf{x}$, in discretisation point s_i, is denoted $p(s_i;\mathbf{x})$.

Now, it is assumed that an observation is made of the difference between the force obtained from the numerical model, and the force for any given experimental curve, in any given discretisation point, s_i. This difference is the *observation error* and denoted as ε_{ik}:

$$\varepsilon_{ik} = p(s_i;\mathbf{x}) - y_{ik} \tag{5.1}$$

It is now possible to assume that the error ε_{ik} is distributed according to some statistical model. In the present work, two different statistical models are assumed, which yields two different cost functions. The first statistical model assumes that the observation error is normally distributed with a zero mean, and constant variance across all discretisation points. ε_{ik} is then normally distributed according to:

$$\varepsilon_{ik} \sim \mathcal{N}(0, \sigma^2) \tag{5.2}$$

The optimal set of parameters, denoted $\hat{\mathbf{x}}$, can then be acquired through maximum likelihood estimation (MLE) of the following log-likelihood (refer to Paper II for the mathematical derivations):

$$l_1(\mathbf{x}) = -\frac{n_k n_i}{2} \log\left(\sum_{ik} (y_{ik} - p(s_i;\mathbf{x}))^2\right) \tag{5.3}$$

As can be seen, this likelihood function corresponds to the least squares error, and is the same as the so-called FEMU-F cost function (Chen et al., 2024), except for the term $\frac{n_k n_i}{2}$ and the natural logarithm.

The second model for the observation error again assumes a zero mean, but with a variance which may be different in each discretisation point s_i, such that

$$\varepsilon_{ik} \sim \mathcal{N}(0, \sigma_i^2) \tag{5.4}$$

Once again, the log-likelihood may be derived through MLE (see paper II for mathematical derivations):

$$l_2(\mathbf{x}) = -\sum_i \frac{n_k}{2} \log \left(\sum_k (y_{ik} - p(s_i; \mathbf{x}))^2 \right) \tag{5.5}$$

As can be seen, both Equations 5.3 and 5.5 are dependent on the discretisation in terms of n_i in l_1 and the summation over the index i in l_2. In addition, the underlying assumption of the statistical models for l_1 and l_2 is that the observation errors are independently distributed. As discussed in Paper II, it is unlikely that this is a reasonable assumption. If a certain point, say s_i, has a positive observation error, it is highly likely that the surrounding points, say s_{i+1}, and s_{i-1}, also have positive observation errors. The observation errors are thus in all likelihood correlated, which means that neither cost function l_1 nor l_2 should be able to accurately recover the variance in the experimental load-displacement curves. This is shown in the next section.

Estimated fracture parameters and uncertainty quantification

The optimal set of parameters acquired with the two different cost functions are presented in Table 5.2, and as discussed in Paper II, these show relatively good agreement with previous studies. With respect to the fracture energy, which is the only quantity that has been experimentally evaluated in the present work, the fracture energy evaluated with FEMU for the spruce specimens shows relatively good agreement with the specific fracture energy as evaluated with the conventional work-of-fracture method. The difference in evaluated specific fracture energy is less than 10% for both spruce series, regardless of cost function used.

For the birch specimens, this discrepancy is larger. The fracture energy estimated with cost function l_2 for the birch specimens with a triangular fracture surface is 20% higher than the fracture energy evaluated with the work-of-fracture method in Paper I. For cost function l_2, the difference is 15%. For the birch specimens with a rectangular fracture surface, the difference is smaller. For these specimens, the fracture energy estimated with cost function l_1 is 13% compared to the work-of-fracture method, whereas for cost function l_2 the estimated fracture energy is 7% higher than with the work-of-fracture method.

For most series, the fracture energy evaluated with the FEMU procedure is higher than the fracture energy estimated with the work-of-fracture method. This is true for all series, and all cost functions, except for the spruce specimens when using cost function l_2. As discussed in Paper II, a potential cause for this could be that the birch specimens have not been loaded with large enough displacement. In total, a displacement of 7

Table 5.2: Estimated fracture parameters based on the FEMU method with two different cost functions, and the conventional work-of-fracture method.

	$l_1(\mathbf{x})$			$l_2(\mathbf{x})$			Work-of-fracture
	G_f [J/m^2]	f_t [MPa]	E_T [MPa]	G_f [J/m^2]	f_t [MPa]	E_T [MPa]	G_f [J/m^2]
Spruce rect	172	3.06	238	198	2.21	241	188
Spruce tri	256	3.22	233	269	2.38	244	257
Birch rect	747	8.37	761	789	6.56	735	700
Birch tri	700	7.39	551	735	4.49	656	611

mm was applied for the birch specimens. On average, the residual force at this point was around 1 N for all specimens. Given the large number of specimens tested in this study, it was considered impractical from a time perspective.

In addition to mean values, it has also been of interest to quantify the inherent material variability in the specimens. With the method described in Chapter 4, the uncertainty of the optimised parameters could be established through the Fisher information evaluated at the MLE estimate of the parameters, i.e. $\hat{\mathbf{x}}$. With this method, an approximate normal distribution of the parameters could thus be acquired for each experimental series, such that

$$\log \mathbf{x} \sim \mathcal{N}(\hat{\mathbf{x}}, \Sigma_{\hat{\mathbf{x}}}) \tag{5.6}$$

Here, it is the log of the parameters that is normally distributed, which in turn means that the actual parameters are log-normally distributed. This is a consequence of the minimisation being carried out in the log-scale to ensure positive material parameters. One approximate statistical distribution was acquired for each cost function, and for each series. For each approximate statistical distributions, 1000 samples were drawn of the parameters. Based on these samples, the corresponding stress-deformation relations with linear softening could be established. These are shown in the left column in Figure 5.2 for cost function l_1 and in the left column in Figure 5.3 for cost function l_2. Furthermore, from the 1000 samples, the global load-displacement curves was calculated for ten randomly selected stress-deformation relations. The ten corresponding load-displacement curves are shown in comparison to the experimental data in the right columns of Figures 5.2 and 5.3, for cost functions l_1 and l_2, respectively. As can be seen, some variability is recovered in certain series, but overall, the variance is never recovered accurately.

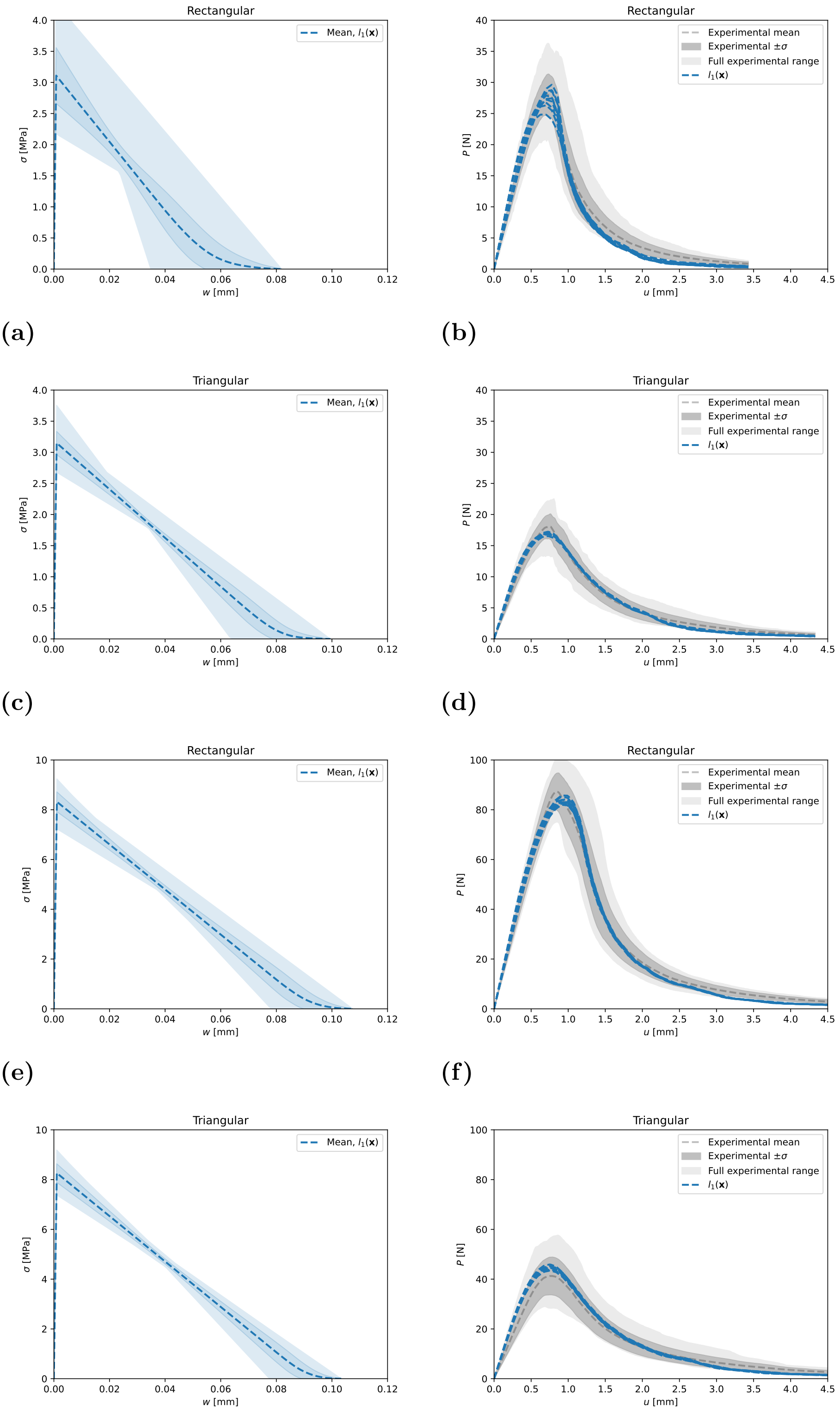

(a) **(b)**

(c) **(d)**

(e) **(f)**

(g) **(h)**

Figure 5.2: Stress-deformation relation for all experimental series (left column) based on estimated parameters with cost function l_1, and the corresponding global load-displacement curves in comparison to the experimental load-displacement curves (right column). Note that the scales are different.

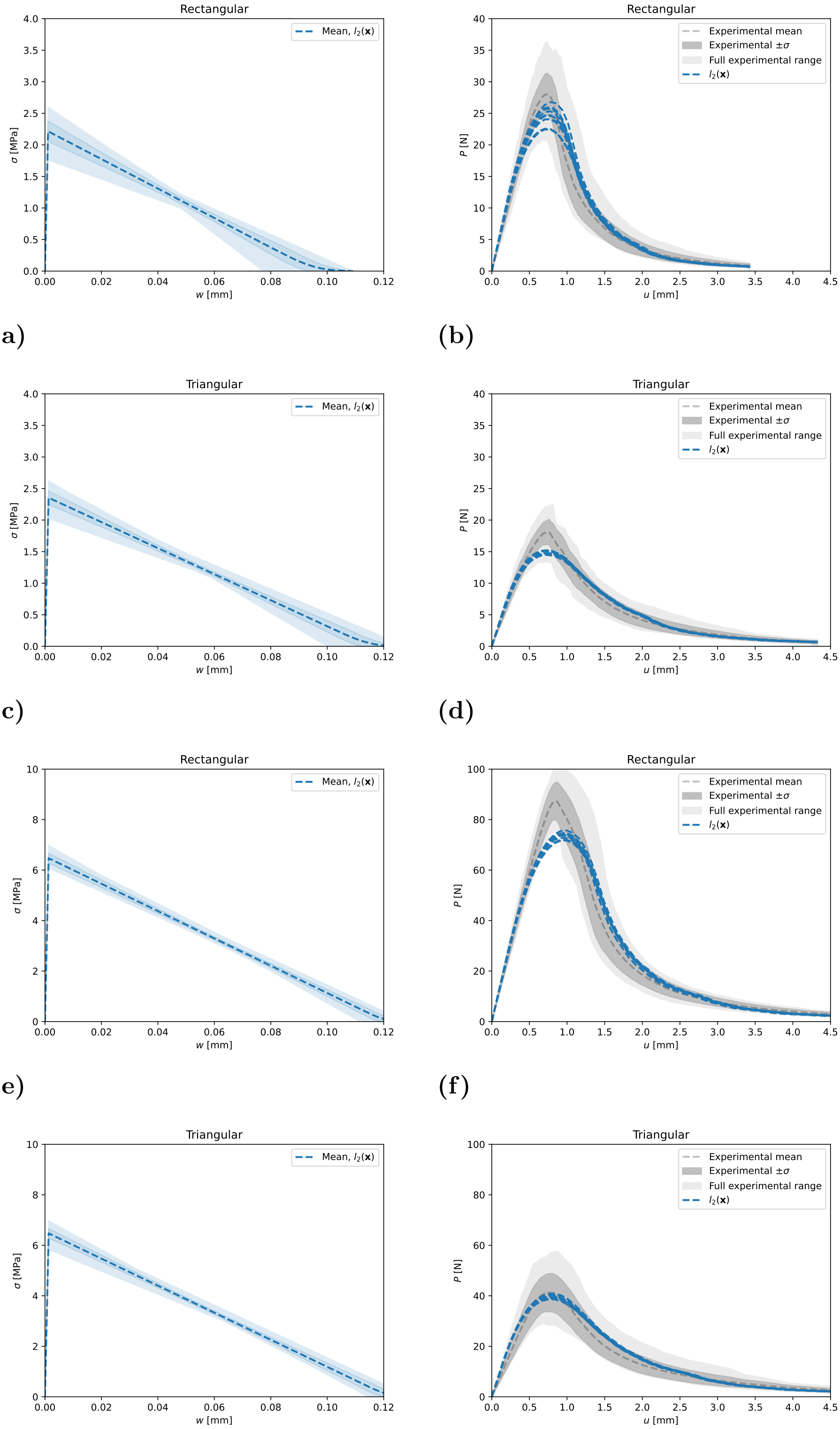

(a) **(b)**

(c) **(d)**

(e) **(f)**

(g) **(h)**

Figure 5.3: Stress-deformation relation for all experimental series (left column) based on estimated parameters with cost function l_2, and the corresponding global load-displacement curves in comparison to the experimental load-displacement curves (right column). Note that the scales are different.

Derivation of a new cost function in conjunction with FEMU

The theory of the cost functions has been developed in the context of Paper II, and as such all authors of Paper II have contributed two the development, with Johan Lindström providing the most important ideas. As can be seen from the results presented in previous sections, neither cost function l_1 nor cost function l_2 were able to accurately recover the variance. To remedy this, a third cost function is introduced. This cost function assumes that the observation error is distributed as a multivariable normal distribution with a zero mean, $\mathbf{0}$, and a covariance matrix across all discretisation points, $\mathbf{\Sigma}$:

$$\varepsilon_{ik} \sim \mathcal{N}(\mathbf{0}, \mathbf{\Sigma}) \tag{5.7}$$

For a multivariate normal distribution, the log-likelihood assumes the following form (Casella & Berger, 2002, Chap 7):

$$\log L_3 = -\frac{n_i n_k}{2}\log(2\pi) - \frac{n_k}{2}\log|\mathbf{\Sigma}| - \frac{1}{2}\sum_k (\mathbf{y}_k - \mathbf{p}(\mathbf{x}))^{\mathsf{T}}\mathbf{\Sigma}^{-1}(\mathbf{y}_k - \mathbf{p}(\mathbf{x})) \tag{5.8}$$

Here, $\mathbf{y}_k$ and $\mathbf{p}(\mathbf{x})$ are the column vectors of the n_i discretisation points, such that

$$\mathbf{y}_k = \begin{bmatrix} y_{1k} & y_{2k} & \dots & y_{ik} \end{bmatrix}^{\mathsf{T}} \tag{5.9a}$$

$$\mathbf{p}(\mathbf{x}) = \begin{bmatrix} p_1 & p_2 & \dots & p_i \end{bmatrix}^{\mathsf{T}} \tag{5.9b}$$

The MLE estimate of the variance of a multivariate normal distribution is given by (Casella & Berger, 2002, Chap 7):

$$\mathbf{\Sigma}^* = \frac{\sum_k (\mathbf{y}_k - \mathbf{p}(\mathbf{x}))(\mathbf{y}_k - \mathbf{p}(\mathbf{x}))^{\mathsf{T}}}{n_k} \tag{5.10}$$

which yields the following expression for the log-likelihood in Equation 5.8, given that additive constants are ignored:

$$\log L_3 = -\frac{n_k}{2}\log\left|\sum_k (\mathbf{y}_k - \mathbf{p}(\mathbf{x}))(\mathbf{y}_k - \mathbf{p}(\mathbf{x}))^{\mathsf{T}}\right| \tag{5.11}$$

The expression inside the determinant may be reformulated from a sum, into a broadcasted matrix expression, such that

$$\sum_k (\mathbf{y}_k - \mathbf{p}(\mathbf{x}))(\mathbf{y}_k - \mathbf{p}(\mathbf{x}))^{\mathsf{T}} = (\mathbf{Y} - \mathbf{p}(\mathbf{x})\mathbf{1}^{\mathsf{T}})(\mathbf{Y} - \mathbf{p}(\mathbf{x})\mathbf{1}^{\mathsf{T}})^{\mathsf{T}} \tag{5.12}$$

Here, $\mathbf{p}(\mathbf{x})\mathbf{1}^{\mathsf{T}}$ is a matrix of dimensions $n_i \times n_k$ with identical columns and $\mathbf{Y}$ is a $n_i \times n_k$ matrix with all observed load-displacement curves. Using a singular value decomposition (SVD) (Bisgard, 2021) of the right hand side, the determinant in Equation 5.11 may be simplified to

$$\left|(\mathbf{Y}-\mathbf{p}(\mathbf{x})\mathbf{1}^\mathsf{T})(\mathbf{Y}-\mathbf{p}(\mathbf{x})\mathbf{1}^\mathsf{T})^\mathsf{T}\right| = |\mathbf{USV}^\mathsf{T}(\mathbf{USV}^\mathsf{T})^\mathsf{T}| = |\mathbf{US}^2\mathbf{U}^\mathsf{T}| = \prod_i s_i^2 \tag{5.13}$$

Here, $\mathbf{U}$ and $\mathbf{V}^\mathsf{T}$ are the right and left unitary matrices of the following SVD:

$$(\mathbf{Y}-\mathbf{p}(\mathbf{x})\mathbf{1}^\mathsf{T}) = \mathbf{USV}^\mathsf{T} \tag{5.14}$$

where $\mathbf{S}$ is the diagonal matrix containing the k non-zero singular values s_i. The log-likelihood, Equation 5.11, may then be rewritten as:

$$\log L_3 = -\frac{n_k}{2}\log\prod_i s_i^2 = -n_k\sum\log s_i \tag{5.15}$$

This cost function is, as can be seen in Equation 5.15 independent of the number of discretisation points n_i. In addition, this cost functions is based on the assumption that the observation error is correlated between discretisation points. At the time of writing this thesis, this cost function has not been fully implemented yet, and thus, no results are shown here.

5.3 Summary and outlook

The aim of the present work has been to characterize the fracture behaviour of wood in mode I loading and in the TL-crack propagation system. The wood species Norway spruce and birch have been studied. In Paper I, the fracture behaviour was characterized in terms of the specific fracture energy, whereas in Paper II, the fracture behaviour was characterized in terms of all three relevant fracture parameters for mode I fracture in the TL-crack propagation system: the tangential stiffness, E_T, the tensile strength, f_t, and the specific fracture energy, G_f. In addition, stress-deformation relations with linear softening behaviour were established in paper II for both wood species, based on the estimated tensile strength and fracture energy. The main scientific contributions of the present work are the following:

- The fracture behaviour of birch and spruce has been established in terms of the following material parameters: the specific fracture energy, G_f, the tensile strength, f_t, and the tangential elastic stiffness, E_T.
- The specific fracture energy seems to be markedly higher for birch compared to spruce. In addition, birch was not found to be more brittle than spruce in the present work. Thus, the higher fracture energy in birch could have a positive impact on load-bearing applications with birch, potentially increasing the load-capacity without increasing the risk of brittle failure.
- Two common cost functions used in FEMU have been reformulated in the context of likelihood-based inference. It has been shown that neither of these two

cost functions can accurately capture the variance of the experimental load-displacement curves in the present work.

- To accurately capture the variance in the parameters, a third cost-function has been proposed, also based on likelihood-based inference. However, at the current point in time, this cost function has not been fully implemented, but the theoretical framework is in place.

The above contributions enable the possibility to further understand how using birch affects the fracture behaviour in load-bearing applications in mode I fracture. However, pure mode I fracture is rare at the structural scale. Instead, mixed-mode fracture is almost always the case. As such, a natural extension of the present work is to establish the fracture behaviour of birch in shear as well, i.e. mode II and III fracture.

A natural extension of the present work is to fully implement the third cost function, in order to properly assess if it possible to capture the variance of the experimental load-displacement curves accurately with it.

In the present work, the stress-deformation relation describing the strain-softening behaviour of the material has only been modelled with a linear softening behaviour. It would be beneficial to extend the work to other types of softening, such as bilinear or exponential softening, to see if it is possible to recover the experimental load-displacement curves better with such relations.

Another natural extension of the present work is to propagate the estimated fracture behaviour to a semi-structural or structural level, when the variance of the experimental load-displacement curves has been captured accurately. By doing this, it is possible to perform large-scale computations of how wooden structures behave during crack propagation in load-bearing structures. This could potentially aid in the creation of robust and accurate design methods for other wood species than spruce.

The continuation of this PhD-project will focus on both experimental and numerical procedures. The experimental part will put more emphasis on the semi-structural or structural scale, in addition to the clear wood level that has been studied thus far. The emphasis in the numerical modelling will be on the development of numerical models for predicting both pure mode I fracture, but also mixed-mode fracture, in addition to potentially accounting for plasticity and other dissipative phenomena in wood.

Bibliography

Anderson, T. L. (1995). *Fracture mechanics: Fundamentals and applications* (2. ed.). CRC Press.

Aster, R. C., Borchers, B., & Thurber, C. H. (2013). *Parameter estimation and inverse problems*. Elsevier. https://doi.org/10.1016/C2009-0-61134-X

Barenblatt, G. I. (1962). The mathematical theory of equilibrium cracks in brittle fracture. *Advances in Applied Mechanics*, *7*, 55–129.

Barham, L., Duller, G. A. T., Candy, I., Scott, C., Cartwright, C. R., Peterson, J. R., Kabukcu, C., Chapot, M. S., Melia, F., Rots, V., George, N., Taipale, N., Gethin, P., & Nkombwe, P. (2023). Evidence for the earliest structural use of wood at least 476,000 years ago. *Nature*, *622*, 107–111. https://doi.org/10.1038/s41586-023-06557-9

Bisgard, J. (2021). *Analysis and linear algebra : The singular value decomposition and applications*. American Mathematical Society.

Bodig, J., & Jayne, B. A. (1982). *Mechanics of wood and wood composites*. Van Nostrand Reinhold.

Boström, L. (1992). *Method for determination of the softening behaviour of wood and the applicability of a nonlinear fracture mechanics model* [Doctoral Thesis, Division of Building Materials, LTH].

Brochu, E., Cora, V. M., & de Freitas, N. (2010). *A tutorial on Bayesian Optimization of expensive cost functions, with application to active user modeling and hierarchical reinforcement learning*. https://doi.org/10.48550/arXiv.1012.2599

Casella, G., & Berger, R. L. (2002). *Statistical inference* (2. ed.). Duxbury.

Chen, B., Starman, B., Halilovič, M., Berglund, L. A., & Coppieters, S. (2024). Finite element model updating for material model calibration: A review and guide to practice. *Archives of Computational Methods in Engineering*. https://doi.org/10.1007/s11831-024-10200-9

De Moura, M., & Dourado, N. (2018). Mode I fracture characterization of wood using the TDCB test. *Theoretical and Applied Fracture Mechanics*, *94*, 40–45. https://doi.org/10.1016/j.tafmec.2018.01.005

De Moura, M., Morais, J., & Dourado, N. (2008). A new data reduction scheme for mode I wood fracture characterization using the double cantilever beam test. *Engineering Fracture Mechanics*, *75*(13), 3852–3865. https://doi.org/10.1016/j.engfracmech.2008.02.006

Dinwoodie, J. (2000). *Timber - Its Nature and Behaviour*. CRC Press. https://doi.org/10.4324/9780203477878

Dourado, N., De Moura, M. F. S. F., Morel, S., & Morais, J. (2015). Wood fracture characterization under mode I loading using the three-point-bending test. Experimental investigation of Picea abies L. *International Journal of Fracture*, *194*(1), 1–9. https://doi.org/10.1007/s10704-015-0029-y

Dourado, N., Morel, S., De Moura, M., Valentin, G., & Morais, J. (2008). Comparison of fracture properties of two wood species through cohesive crack simulations.

Composites Part A: Applied Science and Manufacturing, *39*(2), 415–427. https://doi.org/10.1016/j.compositesa.2007.08.025

Fahlvik, N., Hannerz, M., Högbom, L., Jacobsson, S., Liziniewicz, M., Palm, J., Rytter, L., Sonessson, J., Wallgren, M., & Weslien, J.-O. (2021). *Björkens möjligheter i ett framtida klimatanpassat brukande av skog* (tech. rep.). Skogforsk. Gävle.

Fisher, R. A. (1922). On the Mathematical Foundations of Theoretical Statistics [Publisher: Royal Society]. *Philosophical Transactions of the Royal Society of London. Series A, Containing Papers of a Mathematical or Physical Character*, *222*, 309–368.

Forsman, K., Fredriksson, M., Serrano, E., & Danielsson, H. (2021). Moisture-dependency of the fracture energy of wood: A comparison of unmodified and acetylated Scots pine and birch. *Holzforschung*, *75*(8), 731–741. https://doi.org/10.1515/hf-2020-0174

Forsman, K., Serrano, E., Danielsson, H., & Engqvist, J. (2020). Fracture characteristics of acetylated young Scots pine. *European Journal of Wood and Wood Products*, *78*, 693–703. https://doi.org/10.1007/s00107-020-01548-3

Garnett, R. (2023). *Bayesian Optimization* (1st ed.). Cambridge University Press. https://doi.org/10.1017/9781108348973

Griffith, A. A. (1921). VI. The phenomena of rupture and flow in solids. *Philosophical Transactions of the Royal Society of London. Series A, Containing Papers of a Mathematical or Physical Character*, *221*(582-593), 163–198. https://doi.org/10.1098/rsta.1921.0006

Gullbrandsson, R. (2010). *Ingatorps kyrkbod.*

Gustafsson, P. J. (1988). A study of strength of notched beams. *CIB-W18A*.

Gustafsson, P. J. (1985). *Fracture mechanics studies of non-yielding materials like concrete : Modelling of tensile fracture and applied strength analyses* [Doctoral thesis, Division of Building Materials, LTH].

Hillerborg, A., Modéer, M., & Petersson, P.-E. (1976). Analysis of crack formation and crack growth in concrete by means of fracture mechanics and finite elements. *Cement and Concrete Research*, *6*(6), 773–781. https://doi.org/10.1016/0008-8846(76)90007-7

Hong, P., Schmid, B., De Laender, F., Eisenhauer, N., Zhang, X., Chen, H., Craven, D., De Boeck, H. J., Hautier, Y., Petchey, O. L., Reich, P. B., Steudel, B., Striebel, M., Thakur, M. P., & Wang, S. (2022). Biodiversity promotes ecosystem functioning despite environmental change (A. Mori, Ed.). *Ecology Letters*, *25*(2), 555–569. https://doi.org/10.1111/ele.13936

Irwin, G. R. (1957). Analysis of stresses and strains near the end of a crack traversing a plate. *Journal of Applied Mechanics*, *24*(3), 361–364. https://doi.org/10.1115/1.4011547

Jonasson, J., Danielsson, H., & Serrano, E. (2024a). Fracture energy of birch in tension perpendicular to grain: Experimental evaluation and comparative numerical simulations. *Wood Science and Technology*, *58*(5), 1925–1949. https://doi.org/10.1007/s00226-024-01595-6

Jonasson, J., Persson, P., & Danielsson, H. (2024b). Mitigating footfall-induced vibrations in cross-laminated timber floor-panels by using beech or birch. *Journal of Building Engineering*, *86*, 108751. https://doi.org/10.1016/j.jobe.2024.108751

Kunecký, J., Štembera, V., Kloiber, M., Hataj, M., & Sebera, V. (2024). Optimization of CZM parameters of Norway spruce tested in mode I using multistart simplex method. *Engineering Fracture Mechanics*, *310*, 110430. https://doi.org/10.1016/j.engfracmech.2024.110430

Lai, G., & Plönning, S. (2019). *Fracture characteristics of acetylated birch - Experimental and numerical studies* [Master's thesis, Division of Structural Mechanics, LTH].

MATLAB. (2022). *Version 7.10.0 (r2022b).* The MathWorks Inc.

Matérn, B. (1986). *Spatial Variation* (D. Brillinger, S. Fienberg, J. Gani, J. Hartigan & K. Krickeberg, Eds.; Vol. 36). Springer. https://doi.org/10.1007/978-1-4615-7892-5

Nordtest. (1993). *Wood: Fracture energy in tension perpendicular to the grain.*

Obernosterer, D., Jeitler, G., & Schickhofer, G. Birch for engineered timber products: Part II. In: In *World Conference on Timber Engineering (WCTE 2023).* Oslo, Norway, 2023, 615–620. https://doi.org/10.52202/069179-0084

Pawitan, Y. (2013). *In all likelihood: Statistical modelling and inference using likelihood* (Paperback edition). Oxford University Press.

Persson, K. (2000, December). *Micromechanical modelling of wood and fibre properties* [Doctoral Thesis, Division of Structural Mechanics, LTH]. https://doi.org/10.13140/RG.2.1.1389.7685

Regis, R. G., & Shoemaker, C. A. (2005). Constrained Global Optimization of Expensive Black Box Functions Using Radial Basis Functions. *Journal of Global Optimization*, *31*(1), 153–171. https://doi.org/10.1007/s10898-004-0570-0

Reiterer, A. (2001). The influence of temperature on the mode I fracture behavior of wood. *Journal of Materials Science Letters*, *20*(20), 1905–1907. https://doi.org/10.1023/A:1012878312492

Reiterer, A., Sinn, G., & Stanzl-Tschegg, S. (2002). Fracture characteristics of different wood species under mode I loading perpendicular to the grain. *Materials Science and Engineering: A*, *332*(1-2), 29–36. https://doi.org/10.1016/S0921-5093(01)01721-X

Reiterer, A., Stanzl-Tschegg, S. E., & Tschegg, E. K. (2000). Mode I fracture and acoustic emission of softwood and hardwood. *Wood Science and Technology*, *34*(5), 417–430. https://doi.org/10.1007/s002260000056

Riberholt, H., Enquist, B., Gustafsson, P. J., & Jensen, R. B. (1992, April). *Timber beams notched at the support.* Division of Structural Mechanics, LTH.

Ristinmaa, M., & Ottosen, N. S. (2005). *The mechanics of constitutive modeling.* Elsevier. https://doi.org/10.1016/B978-0-08-044606-6.X5000-0

Shahriari, B., Swersky, K., Wang, Z., Adams, R. P., & De Freitas, N. (2016). Taking the human out of the loop: A review of bayesian optimization. *Proceedings of the IEEE*, *104*(1), 148–175. https://doi.org/10.1109/JPROC.2015.2494218

Stanzl-Tschegg, S., Tan, D.-M., & Tschegg, E. (1995). New splitting method for wood fracture characterization. *Wood Science and Technology*, *29*(1). https://doi.org/10.1007/BF00196930

Stefansson, F. (2001). *Fracture analysis of orthotropic beams: Linear elastic and nonlinear methods* [Licentiate Thesis, Division of Structural Mechanics, LTH].

Sveriges Lantbruksuniversitet. (2022). *Skogsdata 2022* (tech. rep.). Unknown.

Thelandersson, S., & Larsen, H. J. (Eds.). (2003). *Timber engineering.* J. Wiley.

Todorović, M., Koetsier, M., Simović, N., Glišović, I., & Pavlović, M. (2023). Determination of mode I fracture properties of European spruce. *Wood Research*, *68*(2), 334–347. https://doi.org/10.37763/wr.1336-4561/68.2.334347

Van Rossum, G., & Drake Jr, F. L. (1995). *Python reference manual.* Centrum voor Wiskunde en Informatica Amsterdam.

Wang, T., Wang, Y., Crocetti, R., & Wålinder, M. (2022a). In-plane mechanical properties of birch plywood. *Construction and Building Materials*, *340*, 127852. https://doi.org/10.1016/j.conbuildmat.2022.127852

Wang, T., Wang, Y., Crocetti, R., & Wålinder, M. (2022b). Influence of face grain angle, size, and moisture content on the edgewise bending strength and stiffness of birch plywood. *Materials & Design*, *223*, 111227. https://doi.org/10.1016/j.matdes.2022.111227

Yoshihara, H., & Kawamura, T. (2006). Mode I fracture toughness estimation of wood by DCB test. *Composites Part A: Applied Science and Manufacturing*, *37*(11), 2105–2113. https://doi.org/10.1016/j.compositesa.2005.12.001

Part II

Appended publications

Paper I

Wood Science and Technology
https://doi.org/10.1007/s00226-024-01595-6

ORIGINAL

Fracture energy of birch in tension perpendicular to grain: experimental evaluation and comparative numerical simulations

Johannes Jonasson[1] · **Henrik Danielsson**[1] · **Erik Serrano**[1]

Received: 14 April 2024 / Accepted: 19 August 2024
© The Author(s) 2024

Abstract

The present work has experimentally determined the specific fracture energy of the hardwood species silver birch (*Betula pendula*), which in recent times has caught increased attention for utilization in structural applications. The single-edge-notched beam loaded in three-point-bending was utilized for evaluating the fracture energy with the work-of-fracture method. In addition to birch, Norway spruce (*Picea abies*) was utilized as a reference material. The effect of two different geometries of the fracture area for each species was evaluated—one triangular and one rectangular fracture area. It should be noted that the geometry of the fracture area did influence the evaluated fracture energy, and this influence was not consistent between species. This was likely in part due to manufacturing difficulties with the triangular fracture area. In addition to the experimental testing, a numerical 2d-model including linear strain-softening behavior was used for comparative simulations. The numerical 2d-models showed reasonable agreement with the experimental results regarding the global load vs. displacement response, despite their relative simple nature. The specific fracture energy for the spruce specimens was evaluated to 221 J/m^2 and for the birch specimens to 656 J/m^2. Consequently, the present work implies a marked increase in specific fracture energy for birch, compared to spruce. This increase in specific fracture energy could potentially have a large influence on the failure behavior of birch when used in structural applications which is something that needs to be considered in future work.

✉ Johannes Jonasson
johannes.jonasson@construction.lth.se

Henrik Danielsson
henrik.danielsson@construction.lth.se

Erik Serrano
erik.serrano@construction.lth.se

[1] Division of Structural Mechanics, Department of Construction Sciences, Lund University, P.O. Box 118, 221 00 Lund, Sweden

Published online: 28 August 2024

Introduction

For structural applications in Europe, and more specifically the Nordic countries, Norway spruce (*Picea abies*) is the dominant wood species utilized. However, in Europe, there exists a significant amount of hardwood. For example, in Sweden and Finland, birch (*Betula pendula*) makes up 13% of the forest stock (SLU 2022), whereas in central Europe, beech represents a substantial amount of the forest stock. Currently, birch is primarily used in the pulpwood industry and for manufacturing furniture, but in recent years, the interest of extending the fields of application to also include structural use has increased. Due to global warming and the altered growth climate that follows, only relying on a single wood species in the construction industry might not be feasible long-term. However, to enable a potential diversification in the construction industry by utilizing birch, a better understanding of the mechanical behavior and the fracture properties of birch is required.

Elastic behavior of wood

A significant portion of research dealing with structural applications reports on the elastic mechanical behavior of softwoods in general, and Norway spruce in particular. The literature is however scarse when it comes to hardwoods for structural applications, including silver birch. Large and extensive research on the mechanical behavior of wood and wood-based materials has been carried out by e.g., Kollman et al. (1968, 1975) and Niemz et al. (2023). Some parts of the literature that are oriented towards hardwoods focus on North American wood species. For example, Bodig and Jayne (1982), present various mechanical properties of both hardwoods and softwoods, however, all are species native to North America. Some mechanical properties for both silver birch and Norway spruce can be found in the work of Hearmon (1961) in addition to other hardwood and softwood species. The elastic parameters of different wood species were studied by Dahl (2009), where a complete set of elastic parameters for Norway spruce is presented, based on the findings from different sources. Heräjärvi (2004) studied the static bending properties of Finnish birch wood, which were examined together with their dependency on the density. In addition, the possibilities of utilizing birch in engineered wood products, such as glued- and cross laminated timber, have been evaluated by e.g., Jeitler et al. (2016) and Obernosterer and Jeitler (2020), and the results were found promising. Determination of mechanical parameters for birch plywood has been carried out by Wang et al. (2022a, 2022b). In addition, an extensive experimental study on bending strength and stiffness of birch timber boards has been carried out by Lemke et al. (2023).

Collins and Fink (2022) studied the tensile strength parallel to grain of birch on small-scale specimens. Sixty planks were initially sawn from 30 different trees, from which 70 smaller timber boards were acquired. Defect-free parts could then be identified from the 70 timber boards. These defect-free parts were then used for manufacturing small-scale specimens, which were designed as dog bone shaped specimens for determining the ultimate tensile strength.

Fracture behavior of wood

In addition to the elastic behavior of wood-based structures, the behavior at failure, often characterized by fracture in wood, is of particular importance to ensure structural safety. When considering the fracture characteristics of materials, these are often evaluated in terms of the specific fracture energy G_f, i.e., the energy required to create a unit area of traction-free surface. Although the specific fracture energy is very influential on the fracture behavior of solids, it is not the only governing factor. When speaking of fracture, the *material brittleness* is a commonly used term. The material brittleness is not only governed by the specific fracture energy, G_f, but also by the stiffness, E, and the ultimate strength, f, of the material. The material brittleness is often characterized with the so called characteristic length. The characteristic length, denoted l_ch, is determined according to $l_\mathrm{ch} = \frac{EG_\mathrm{f}}{f^2}$.

Evaluating the fracture energy is not a new endeavour, and different experimental methods have been developed for this very purpose. Such methods were originally developed and utilized for determining the fracture energy of steel and concrete but have with time been adopted and modified for testing wood. Some examples of such methods are the double cantilever beam (DCB), the tapered double cantilever beam (TDCB), compact tension (CT) specimens and the single-edge-notched beam (SENB) loaded in three-point-bending. All methods have their respective strengths and weaknesses, but in general, the SENB is simple and convenient to use, since it does not require any monitoring of the crack-opening width (de Moura and Dourado 2018).

Wood is often considered a quasi-brittle material, in contrast to perfectly brittle materials, such as glass (Smith et al. 2003). Usually, the peak load for quasi-brittle materials is preceded by a non-linear behavior. However, unlike brittle materials, which usually experience sudden catastrophic failure, quasi-brittle materials experience toughening mechanisms in the fracture process zone (FPZ), e.g., micro-cracking and fiber-bridging in wood. As a consequence, quasi-brittle materials usually experience strain-softening behavior. As such, to accurately evaluate the fracture energy of wood using non-linear fracture mechanics, it is important that stable crack propagation is achieved during experimental testing. Here, stable crack propagation refers to the ability to accurately capture the strain-softening response of the specimens used in the previously mentioned experimental methods (DCB, TDCB, CT and SENB specimens), without experiencing sudden large load-drops. A method suitable for this is described in the standard NT BUILD 422 (Nordtest 1993). The standard, which specifies a method for determining the specific fracture energy in wood in tension perpendicular to grain, is named the Nordtest method, and was originally proposed by Gustafsson (1988). It is a powerful method in the sense that only the applied force and displacement of a SENB specimen have to be recorded. In addition, the Nordtest method works well for sufficiently small wooden specimens, since this ensures that the only source of energy dissipation is the creation of a crack. For smaller specimens, the fracture process zone can be quite large in comparisons to the absolute specimen size. Under such conditions, methods based on linear elastic fracture mechanics, such as the R-curve concept, break down, and are not feasible for evaluation of the specific fracture energy.

Wood, which usually is considered an orthotropic material, is often characterized by its three principal directions; L, the longitudinal direction of the fibers, R, the radial direction and T, the tangential direction, with respect to the growth rings. Consequently, six different crack propagation systems can be identified. These systems are denoted LR, RL, TL, LT, RT and TR, where the first letter denotes the direction normal to the crack plane and the second letter denotes the crack propagation direction, see Fig. 1. A crack in any of the first four systems is generally governed by cell fracture, whereas the latter two are governed by cell separation (Conrad et al. 2003).

In practice, wooden structural elements often have to be modified with respect to their geometry, by for example introducing holes or notches. Such geometrical modifications typically introduce stresses that act perpendicular to the fiber direction (Thelandersson and Larsen 2003), creating a risk of fracture occurring along the grain, i.e., fracture in the TL or RL-propagation system. To better understand the effect of utilizing birch in such applications, it is important to characterize the fracture behavior in these crack propagation systems. Previous research indicates that the TL-direction generally seems to have a lower fracture energy for several wood species (Reiterer et al. 2002), and as such, the TL-direction is the focus of the present work.

The fracture behavior of Norway spruce has previously been evaluated by Ostapska and Malo (2020) and Reiterer et al. (2002). In both works, the fracture behavior was evaluated by means of a wedge splitting test, from which the fracture energy and the stress intensity factor were determined. The fracture energy in the TL-direction was determined by Reiterer et al. (2002), Reiterer and Stanzl-Tschegg (2002) and Dourado et al. (2015), using SENB specimens. In addition, the fracture behavior of both Norway spruce and birch was evaluated by Tukiainen and Hughes (2013, 2016). Forsman et al. (2021) evaluated the fracture energy of birch and spruce in the TL-direction by means of the Nordtest method. In the Nordtest method, a rectangular fracture area is prescribed, but Forsman et al. (2021) used a triangular fracture area to achieve sufficient stability of the load–displacement curve during experimental testing. Numerous studies have been conducted with regards to how a triangular fracture area affects the fracture toughness in testing of materials such as metals,

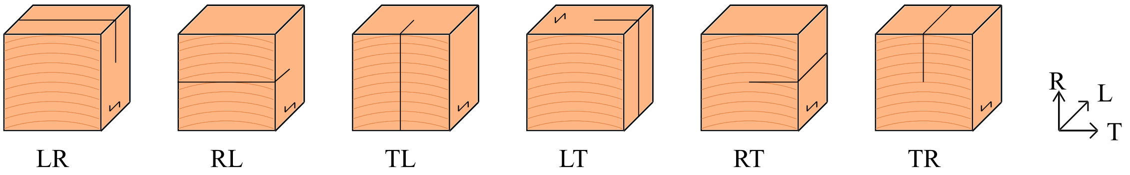

Fig. 1 Different crack propagation systems in wood. The first letter denotes the direction normal to the crack plane, and the second the direction of crack propagation

composites and ceramics (Dlouhý and Boccacini 2001; Sheikh et al. 2015). However, to the author's best knowledge, comparisons between a rectangular and triangular fracture area have not been carried out for the materials in the present work; spruce and birch.

In Eurocode 5 (EN 2004), a few design criteria are based on concepts from fracture mechanics, although this is not explicitly stated in the code. One example is the design criterion with respect to splitting for beams with connections loaded perpendicular to grain. The design criterion employs a single material characteristic value regardless of strength class and wood species. Consequently, if birch would be used to a greater extent for structural applications, its fracture behavior and fracture energy should be considered, and different standardized values should potentially be adopted to ensure a material-efficient design practice.

Establishing mechanical parameters, such as the fracture energy, is also important in the field of numerical simulations. It is well-known that accurate material characteristics are crucial to be able to achieve accurate numerical models which can produce reliable results. Determining mechanical parameters on the clearwood or small-scale specimen level, and then using said parameters for simulations at the structural level is a common approach in engineering science. As such, if the fracture behavior could be established on the clearwood level, for birch, this behavior could then be utilized at a structural level in numerical models of load-bearing applications, to evaluate the effect of using birch. Such numerical models often, in turn, serve as a base for development of design criteria, and it is thus of great importance to establish representative input parameters to said models.

Aim and objective

Accelerating the use of hardwoods, particularly birch, in the construction industry can provide both structural and environmental benefits, such as enhanced biodiversity in forestry. However, to increase the use of birch in structural applications, its mechanical properties must be well understood.

The primary aim of the present paper is to further develop the understanding of the fracture behavior of birch, using the Nordtest method to evaluate the specific fracture energy. A secondary aim is to assess the difference in evaluated fracture energy when using different geometries for the fracture surfaces—herein a rectangular and a triangular fracture area. With previous work indicating increased material brittleness in birch, compared to spruce, modifications to the experimental method might be needed to achieve a stable post-peak behavior of the load–displacement response, which is crucial for reliable evaluation of test results. In turn, the present work could lead to a better understanding of the fracture behavior of birch, which could aid in optimizing design processes where birch is utilized.

The remainder of the paper is structured as follows. Section "Materials and methods" introduces the experimental method used for evaluating the fracture energy, the tested materials, a description of the post-processing of the experimental data, and lastly a brief description of the numerical modeling approach applied. Section "Results and discussion" presents the results, together with a

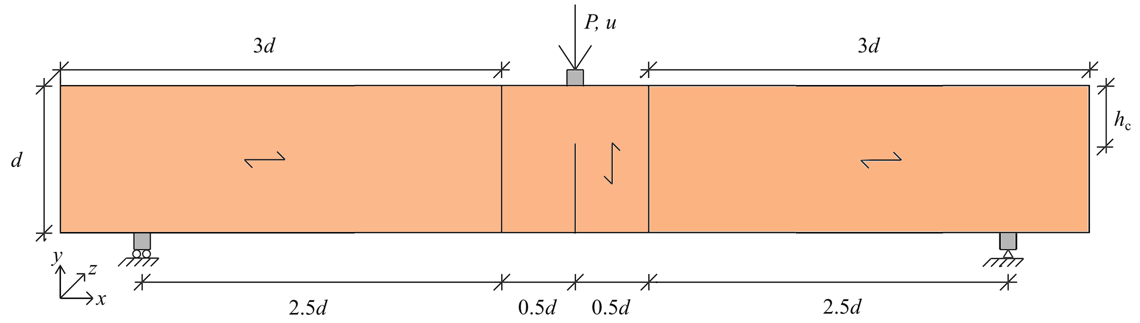

Fig. 2 Schematic two-dimensional illustration of the Nordtest set-up. The beam depth is equal to d and h_c denotes the ligament length

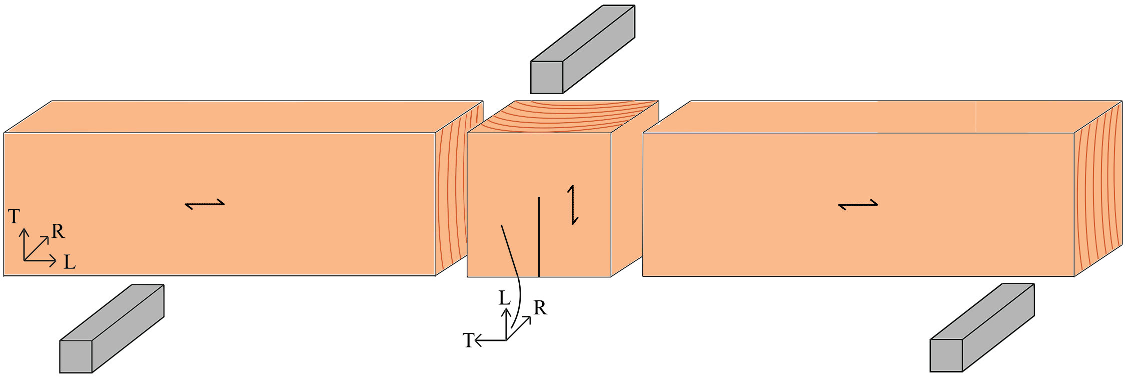

Fig. 3 Exploded view of the SENB specimen. Dimensions according to Fig. 2

discussion. Lastly, in Section "Conclusions and outlook", conclusions and suggestions for further studies are presented.

Materials and methods

Evaluation of specific fracture energy

In the Nordtest method, a wood beam is loaded in three-point-bending until failure, see Figs. 2 and 3. The beam is assembled from three parts; two identical lateral pieces and one middle piece. In the middle piece, a notch is sawn just before testing, to ensure stability and crack-initiation at the mid-section of the beam. The lateral pieces are oriented with their fiber direction in the beam's longitudinal direction, and the middle piece is oriented to achieve the desired crack propagation system. In the present work, this corresponds to the TL-propagation system, see Fig. 1. The beam is loaded in a displacement controlled setting and the load, P, and the corresponding displacement, u, are recorded. The aim is to capture the complete load versus displacement response, including the descending part after the peak load has been reached, until zero load at complete failure of the specimen. The specific fracture energy of the specimen can then be calculated as follows (Nordtest 1993):

$$G_{\mathrm{f}} = \frac{W + mgu_0}{A_{\mathrm{c}}} \tag{1}$$

where

$$m = 5/6 \cdot m_{\mathrm{tot}} + 2 \cdot m_{\mathrm{prism}} \tag{2}$$

and m_{tot} is the mass of the test specimen and m_{prism} is the mass of the steel prism on top of the beam, see Fig. 3. W equals the total work done to fracture the specimen, i.e., the area under the load–displacement curve. A_c is the fracture area of the specimen, which is different for the rectangular and triangular fracture surfaces, respectively, see Fig. 4. u_0 is the load-point displacement at complete failure, and g is the gravitational acceleration.

Experimental testing

SENB specimens

Two wood species, spruce and birch, and two different geometries of the fracture area were used in the four test series of this study, see Tables 1 and 2. The different geometries of the fracture surfaces are illustrated in Fig. 4. The triangular fracture area has a ligament length, h_{c}, of 10 mm, whereas the rectangular fracture area has a ligament length of 8 mm. In the Nordtest standard, the beam height, d, is prescribed to 60 mm. However, in the present work a beam height of $d = 20$ mm was adopted for two reasons: (i) the raw material used for creating the birch specimen did not

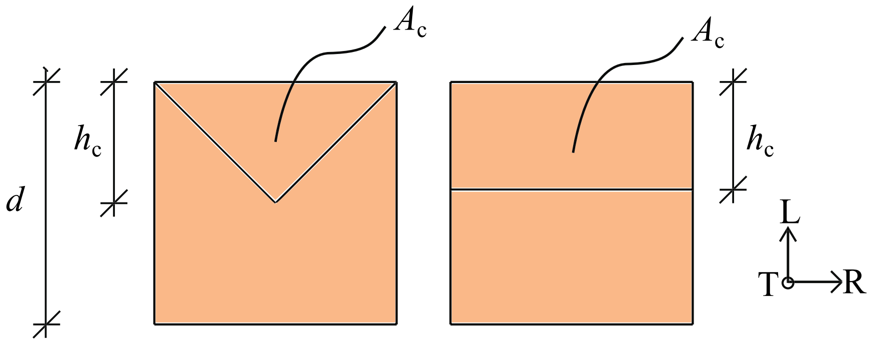

Fig. 4 The two different fracture surfaces used in the present work

Table 1 Spruce test series

Spruce	S43	TS43
No. of specimens	20	19

Table 2 No. of birch specimens from each birch timber piece

Birch	B02	B03	B04	B05	B06	TB08	TB09	TB10	TB11
No. of specimens	5	5	5	2	4	4	7	5	4

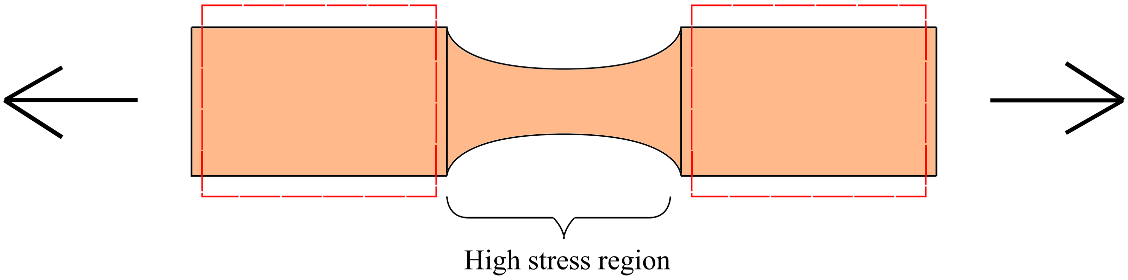

Fig. 5 Schematic illustration of the dog bone specimens and where the material tested in the present work was extracted from. After sawing/planing, birch specimens were only created from the areas marked by dashed red squares (color figure online)

allow for larger dimensions and (ii) to improve post-peak stability and thus ensuring proper evaluation of the fracture energy. A smaller specimen entails a larger relative size of the FPZ in comparison to the specimen size, in turn leading to a more ductile behavior during testing. In addition, it has previously been shown by Persson et al. (1993) that, for larger specimen sizes, the effect of plastic dissipation affects the evaluated fracture energy. However, for a sufficiently small specimen size, the plastic dissipation becomes negligible.

The specimens made of Norway spruce were manufactured from structural timber of strength class C24. Timber boards of nominal size 45 × 90 mm^2 were initially planed and sawn length-wise into sticks with a cross-sectional area of 20 × 20 mm^2. The sticks with the growth-ring orientations most appropriate for evaluating the fracture energy in the TL-direction were further used for creating the middle pieces for the SENB specimens, whereas the remaining sticks were utilized to create the lateral pieces. Lateral pieces of spruce were used for the spruce series as well as for the birch series. The lateral pieces were sawn to nominal lengths of 60 mm and the middle pieces were sawn into cubes, with nominal dimensions of 20 × 20 × 20 mm^3.

In Table 1, S and TS denote spruce specimens with a rectangular and triangular fracture area, respectively. Initially, four different spruce timber boards were planed and split into nine sticks in total. The four boards were identified by the numbers 1–4, and the sticks within each board by the numbers 1–3. As such, all spruce specimens were extracted from the same stick, from the same timber board—in this case the third stick from the fourth timber board (thus the names S43 and TS43).

The material used for the birch specimens originated from Finland, where its tensile strength in the direction of the grain previously had been experimentally tested using dog bone specimens (Collins and Fink 2022). The broken specimens were acquired from Aalto University where the pieces in the best condition after testing were chosen. The pieces with the most optimal fiber orientation for testing in a TL-orientation, see Fig. 1, were selected for the Nordtest specimens in the present work. It should be noted that the specimens were extracted from the outer parts of the dog bone specimens, see Fig. 5. These outer parts have been clamped, but free from large stresses in comparison to the middle-section of the dog bone specimens.

Due to dimensional limitations, 20 specimens could not be acquired from a single dog bone specimen. Instead, between two and seven middle pieces for the SENB specimens according to Fig. 3 could be extracted from each dog bone specimen.

Consequently, one series of birch specimens included birch wood from four to five different dog bone specimens. The number of specimens acquired from each dog bone specimen is shown in Table 2. In this table, TB denotes a triangular fracture area and B a rectangular. Due to manufacturing problems, specimens B01 and B07 were unfit for further processing, and they were excluded from the study. In addition, one middle piece was excluded from each of the test series TS43 and TB10 due to erroneous notch preparation. In total, 82 specimens were created and testing was carried out on 80 specimens. In all other aspects, the approach for manufacturing the birch middle pieces was the same as for spruce; the pieces were planed into sticks with a nominal cross-sectional dimension of 20×20 mm^2 and then sawn into cubes with nominal dimensions of $20 \times 20 \times 20$ mm^3, cf. Figure 3.

All pieces, spruce and birch, were conditioned in a climate chamber with a relative humidity of 60% and a temperature of 20 ± 0.2 degrees Celsius until the change in weight was less than 0.1 g over 24 h. The parts were glued together with a commercial PVAc wood adhesive, and again conditioned in the same climate chamber. The dimensions and the weight of each birch specimen were determined to the nearest 0.1 mm and 0.1 g, respectively, and again conditioned until less than 0.1 g change in weight was observed over 24 h. Before testing, the positions for the supports were marked on all specimens to ensure repeatability of the test set-up to the greatest extent possible. When the specimens had been marked, they were placed in a ziplock bag in the climate room and taken to a small band-saw, where the notches were sawn. The band-saw had a blade with a measured thickness of 0.54 mm. Directly after sawing the notch, each specimen was placed back inside the ziplock bag.

To ensure the nominal notch geometries, special jigs were used. For the triangular notch, a jig which enabled the correct orientation of the specimen during cutting was used. As such, the first cut was made in this jig, followed by a 90-degree rotation of the specimen, followed by a second cut, creating the triangular notch geometry. In addition, an attached wood piece behind the saw blade was used, ensuring the intended nominal saw cut depth into the specimens.

Density and moisture content

The density was evaluated by measuring the dimensions and the weight of all specimens. All birch pieces were weighed before, during and after conditioning in the climate chamber, whereas the complete set of spruce pieces was weighed only before conditioning. A smaller set of the spruce pieces was then weighed during and after conditioning, to ensure moisture content equilibrium.

The moisture content (MC) was determined on specimens cut from the middle pieces, after testing. The oven drying method was used, with a temperature of 105 °C. The mean moisture content for each series is shown in Table 3.

Table 3 Mean measured density and moisture content of the four test series

	S43	TS43	B	TB
ρ (kg/m^3)	397.4 (0.033)	392.2 (0.015)	690.7 (0.019)	630.4 (0.074)
MC (%)	14.2 (0.019)	14.5 (0.013)	11.4 (0.034)	12.5 (0.012)

Coefficient of variation in parenthesis

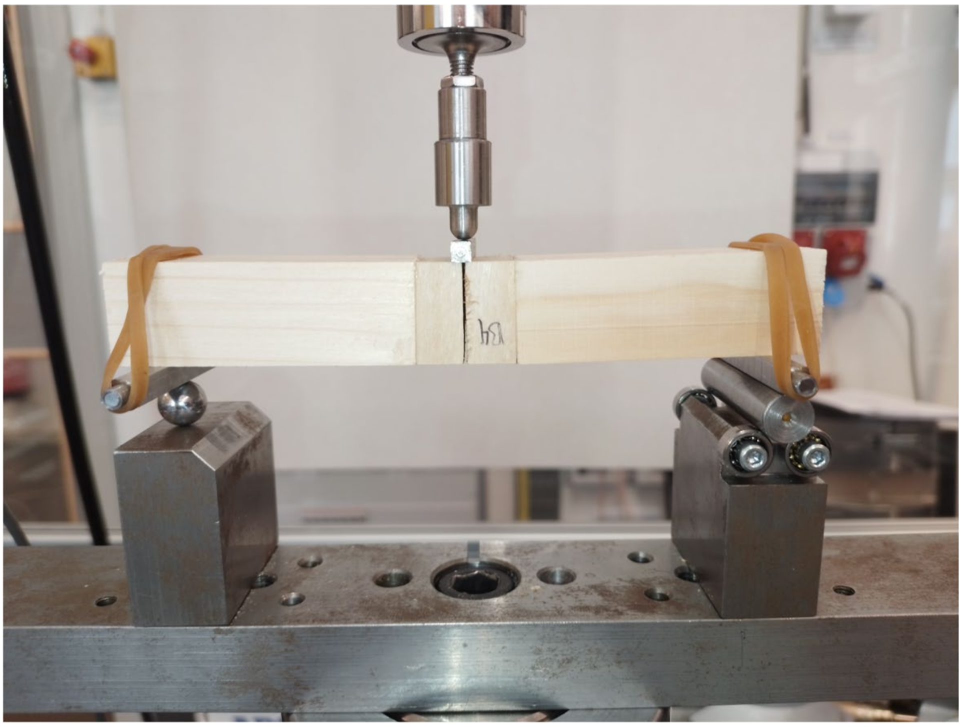

Fig. 6 Experimental test set-up

Testing procedure

The experimental testing of the 80 specimens was carried out in batches of five to ten specimens. The specimens were loaded in a displacement controlled manner in a MTS-machine, see Fig. 6.

During the testing of the specimens, a load cell with a capacity of 500 N was utilized. A total displacement of 5 mm was applied to the spruce specimens, whereas 7 mm was applied to the birch specimens. The rate of loading was set to a constant 0.75 mm/min, which resulted in the peak load being reached after roughly 90 s, and a total test duration of 400–600 s.

Due to the horizontal displacement of the beam at the roller support, which increases with the vertical displacement, some specimens experienced downfall from the test set-up before reaching the full prescribed displacement. To ensure that they were still comparable with respect to their fracture energy, the difference in fracture energy between the downfall specimens and the fully displaced specimens was examined; the difference was found to be negligible.

Post-processing of experimental data

Load–displacement curves were recorded with a sampling frequency of 128 Hz. Due to the high sampling rate, a sensitivity study on the influence of sampling frequency on the estimated fracture energy was carried out. This included the use of sampling frequencies from 0.25 to 128 Hz in the evaluation of fracture energy. It was found that a sampling frequency of 1 Hz was sufficient, and thus this frequency of included data points was used for the further post-processing of the recorded data.

Determination of fracture surface area

From Eq. 1, it is obvious that the area of the fracture surface is decisive in calculating the fracture energy. As such, it is of interest to determine the fracture area of each specimen with a sufficiently accurate approach. The area of the fracture surface was measured after the tests. With respect to the specimens that experienced downfall, explained in the previous section, these specimens had cracks that had propagated enough for the specimens to still be considered completely fractured, having a negligible ligament length left, and a low remaining load left (1–2% of the peak load). In the present work, the fracture area was measured with the program GNU Image Processing Program (GIMP) (The GIMP Development Team 2019). Initially, photos were captured of all fracture surfaces together with a ruler, for scale. The pictures were then imported into GIMP, and with the histogram function, the number of pixels in a certain selected area could be determined. By scaling the number of pixels to the ruler, the specimen fracture area could be determined. In Table 4, the nominal and mean measured areas are shown for all four series. As can be seen, the average area is fairly close to the nominal area for the two spruce series, however, the deviation is larger for the two birch series. Due to this, all analyses were carried out with respect to the measured area, A_{real}, to allow for proper evaluation of the fracture energy.

Evaluation of stability

Currently, there is no method in the Nordtest standard for evaluating the stability. In this paper, the method proposed by Forsman et al. (2021) has been utilized. The method defined a load drop parameter, LC, based on the magnitude of the largest load drop in relation to the maximum load:

Table 4 Nominal and mean measured fracture area (measured with GIMP) for the different test series

	A_{nom} (mm^2)	A_{real} (mm^2)
Spruce-rectangular	160 (–)	162.3 (0.036)
Spruce-triangular	100 (–)	100.1 (0.035)
Birch-rectangular	160 (–)	174.3 (0.075)
Birch-triangular	100 (–)	115.7 (0.069)

Coefficient of variation in parenthesis

Table 5 No. of specimens experiencing differently sized load-drops

	$LC \le 5\%$	$5\% < LC \le 10\%$	$10\% < LC \le 15\%$	$LC > 15\%$	Total
S	7	11	2	0	21
TS	5	12	1	1	20
B	17	3	0	0	20
TB	17	4	0	0	19

The analysis was carried out based on a sample frequency of 1 Hz

Fig. 7 Schematic example of a recorded load–displacement curve with illustration of how the displacement increases with zero load until contact is initiated (1) and nonlinearities that occur after initial contact (2)

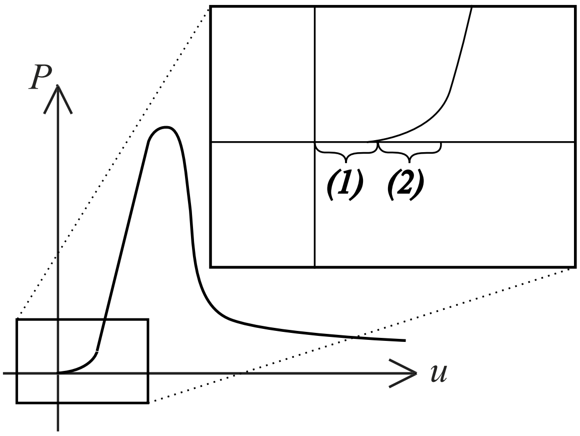

$$LC = |P_i - P_{i+1}|/P_{\max} \times 100 \tag{3}$$

In Eq. 3, P_i and P_{i+1} denote two subsequently recorded load data points, and $P_{\max}$ denotes the maximum load recorded. An arbitrary limit level of load-drop, LC, can be decided (e.g., 5, 10, 15, 20%) defining all curves exceeding this limit as being unstable. It is important to note that this method does not necessarily eliminate the arbitrariness regarding the definition of stability, however, to some extent it makes it quantifiable. Table 5 presents an overview of the distribution of load-drops found.

Load–displacement curves

An example of a recorded load–displacement curve is shown in Fig. 7. From the unprocessed load–displacement curves, two problems are evident. Firstly, the curve does not start with an initial load and displacement equal to zero, due to the fact that the recording of data is initiated before the beam actually is in contact with the loading equipment that applies the force. Secondly, it is apparent that some non-linearities occur at the onset of loading when the beam is establishing contact with the prism and the supports. To simplify the comparison between different tests, and between tests and numerical simulations, the initial non-linear part was removed and all curves were modified such that both the initial load and displacement were equal to 0.

For each curve, the non-linearity was dealt with by conducting successive linear regressions between two points. The distance between the two points was set to 10% of the maximum load, for each curve. For each such 10% interval, the coefficient of determination, R^2, was determined. The interval with the maximum R^2-value was chosen to represent the actual elastic stiffness of the specimen. Any point on the curve prior to this interval was replaced with a point coinciding with this stiffness. The value of the displacement at the intersection of this straight line and the x-axis could then be determined and subtracted from all recorded displacement values. With this methodology, the initial non-linear part of the curves becomes linear and all curves originate at (0,0). The effect on the evaluated fracture energy by using this approach to modify the curves was in most cases less than 1%, compared to evaluating the fracture energy, G_f, with the unprocessed data.

Numerical modeling

The calculation model used for the numerical simulations of the experimental Nordtest set-up is schematically shown in Fig. 8. Two-dimensional plane stress conditions were assumed and symmetry was utilized in the beams' middle-section, i.e., at the pre-defined crack path. The pre-defined crack path was modeled as a cohesive zone with non-linear springs, where the non-linear springs were modelled with a strain-softening behavior. The non-linear springs had an initial length of zero and were in their left-most degree of freedom (dof) connected to the beam, with the other node connected to the ground, using 'SPRING1' in the commercial FE-software ABAQUS (Dassault 2019). The springs could only transfer force in the horizontal direction. Two-dimensional, linear, plane stress elements (CPS3) were used, with an element size of 0.25 mm for the middle piece, and 1 mm for the lateral piece.

Mechanical parameters

The elastic parameters of spruce and birch have not been tested experimentally in the present work, and instead values were collected from the literature. The elastic parameters collected for birch were acquired from the works of Dinwoodie (2002)

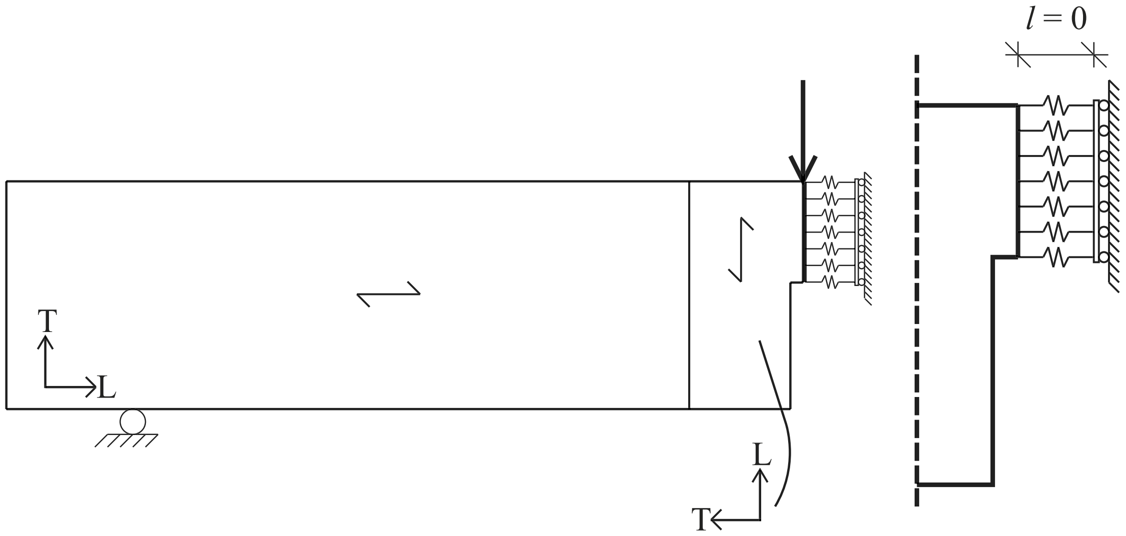

Fig. 8 Schematic illustration of the calculation model of the symmetric half of the SENB specimen (left) and close-up of the non-linear springs (right), with an initial length of zero

Table 6 Elastic parameters and tensile strength perpendicular to grain for spruce and birch, respectively

	E_L	E_T	ν_{LT}	G_{LT}	f_t
Spruce	10,991	435	0.48	682	3
Birch	16,300	620	0.51	910	7

Moduli and tensile strength in MPa, dimensionless Poisson's ratios

and are presented in Table 6 together with the corresponding values for spruce. The values used for spruce are from Dahl (2009), where mechanical parameters for Norway spruce were compiled from a number of sources. For the tensile strength perpendicular to the grain, f_t, a value of 7 MPa was used for birch, acquired from Kollman et al. (1968), and a value of 3 MPa for spruce (Danielsson 2013). These values were used as a starting point for the numerical simulations, but modified as needed to fit the elastic part of the load displacement curve, see Section "Results and discussion".

A generic linear strain-softening behavior is shown in Fig. 9. It should be noted that the displacement value δ_1 should theoretically equal 0, i.e., no deformation in the FPZ occurs until the tensile strength, f_t, has been reached. However, this is complicated in practice due to issues with convergence, and instead, a high initial stiffness, k_{init}, resulting in negligible elastic deformation at maximum stress is chosen. For a sufficiently high initial stiffness, the global load–displacement behavior is not affected. Here, a stiffness of $5 \cdot 10^{11}$ Pa/m was chosen after carrying out a sensitivity study with respect to the initial stiffness, see Section "Effect of initial stiffness and element size". The springs were modelled as ten times stiffer in compression compared to tension. The fracture energy for both wood species was acquired from the present work. Based on these parameters, linear strain-softening relations could be established for spruce and birch. The parameter δ_1, was determined according to

$$\delta_1 = \frac{f_t}{k_{init}} \tag{4}$$

and the parameter δ_2 according to

Fig. 9 Schematic illustration of a cohesive linear softening law used for simulating quasi-brittle fracture. Note that the figure is not drawn to scale

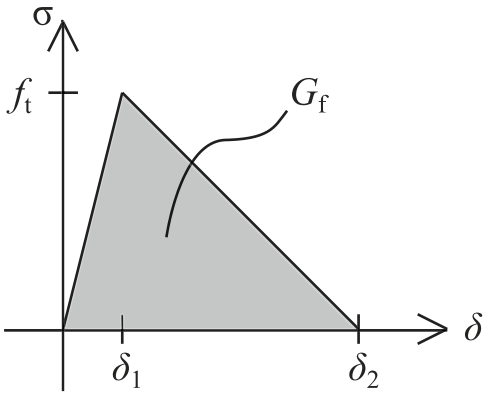

$$\delta_2 = \frac{2G_\mathrm{f}}{f_\mathrm{t}} \tag{5}$$

The strain-softening behavior of spruce has been determined before to some extent (Dourado et al. 2015, 2008; Stanzl-Tschegg et al. 1995). However, to the authors best knowledge, the literature does not contain any work that has determined the strain-softening behavior of birch. Consequently, the same shape of the strain-softening behavior of spruce has been utilized, but instead scaled with the tensile strength and fracture energy of birch.

The strain-softening behavior is usually expressed as a stress-displacement relation, see Fig. 9. As such, since the springs of the FE-model carry a force, and not a stress, the stress-displacement relation has to be converted to a force-displacement relation. Conveniently, this can be carried out by the relation

$$F_\mathrm{spring} = \sigma A_\mathrm{spring} \tag{6}$$

where σ is the tensile stress perpendicular to the grain, F_spring is the force in the spring, and A_spring its tributary area. For the model with a rectangular fracture area, all springs had the same tributary area, except the top- and bottom-springs, which had half the tributary area of the other springs. For the specimens with a triangular fracture area, the tributary area was different for each spring, due to the geometry of the notch, resulting in a linear variation of tributary area along the height of the fracture plane. The initial stiffness, k_init, was not modified to account for the varying width of the triangular fracture surface. This is motivated since k_init anyhow should be regarded as infinitely stiff.

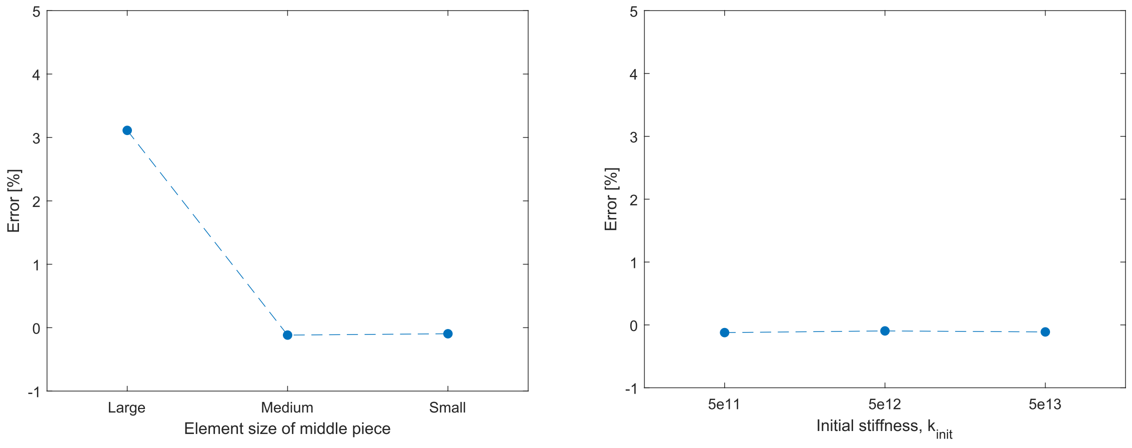

(a) (b)

Fig. 10 Relative error between input fracture energy and output fracture energy evaluated from external work in the FE-model for **a** different element sizes in the middle piece, and, **b** different values of the initial stiffness k_init for the medium element size

Effect of initial stiffness and element size

To evaluate proper initial stiffness, k_{init} and element size, a convergence study was carried out with regard to these parameters. The element sizes were 0.5 mm (large), 0.25 mm (medium) and 0.125 mm (small). The initial stiffness was tested for values of 5×10^{11} Pa/m, 5×10^{12} Pa/m, and 5×10^{13} Pa/m. The convergence study was carried out using the mechanical parameters for spruce presented in Table 6. The effect of the element size is shown in Fig. 10a, where the relative difference between the input fracture energy and the output fracture energy evaluated from the external work was determined for three different levels of mesh refinement and k_{init}. As is shown, the error reduces drastically from the large to medium element size, but next to nothing between the medium and small element size. As such, the medium mesh was deemed sufficient. As can be seen in Fig. 10b, the different values of initial stiffness, with the medium element size, did not markedly affect the same relative difference between input fracture energy and external work. Consequently, a stiffness of $5 \cdot 10^{11}$ Pa/m was deemed sufficient for subsequent analyses.

Results and discussion

Experimental results

In the present work, the Nordtest method was modified by introducing a triangular fracture area, in addition to the normally employed rectangular fracture area. The reason for this was due to previous work implying increased material brittleness in birch (Forsman et al. 2021), in turn resulting in reduced stability of the post-peak behavior. The load–displacement curves acquired from the experimental testing are shown in Fig. 11, together with a load–displacement curve from the numerical simulations. It is evident that the birch specimens showed a more stable post-peak behavior than the spruce specimens, see Table 5. Out of the 39 spruce specimens, 27 specimens had a maximum load-drop larger than 5%, whereas for the birch specimens the same number was only seven. No birch specimens, and only four spruce specimens, had a maximum load-drop larger than 10%. In addition, no apparent difference in stability could be identified between the rectangular and triangular fracture area, for either species. However, this might be a direct consequence of the size of the specimen, see e.g., Karihaloo (1995), since for sufficiently small specimens, post-peak instability should not be an issue.

The fracture energy of the spruce specimens in the present work was evaluated to 188 J/m^2 for the S43-series and 257 J/m^2 for the TS43-series, see Table 7. The individual results for each specimen are shown in Online Resource 1. The results are in accordance with previous findings in the literature. For example, the fracture energy of spruce, conditioned to a moisture content of 11–13%, was evaluated by means of linear elastic fracture mechanics to 150 J/m^2 by Dourado et al. (2015). Similiary, it was evaluated to 150 J/m^2, at a moisture content of 12–13%, by Stanzl-Tschegg et al. (1995), by means of a wedge splitting method. In another study (Reiterer et al. 2002), the fracture energy for spruce was evaluated to a slightly higher

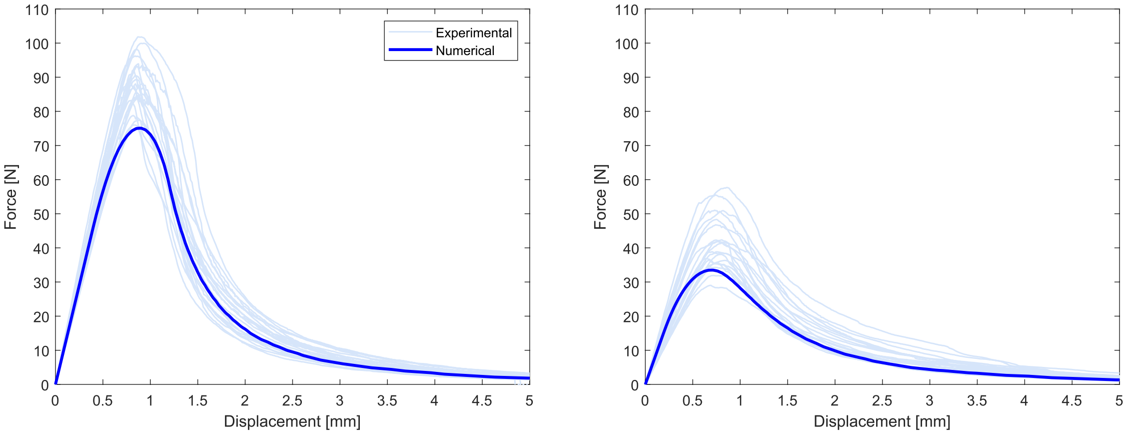

(a) Birch - rectangular notch.

(b) Birch - triangular notch.

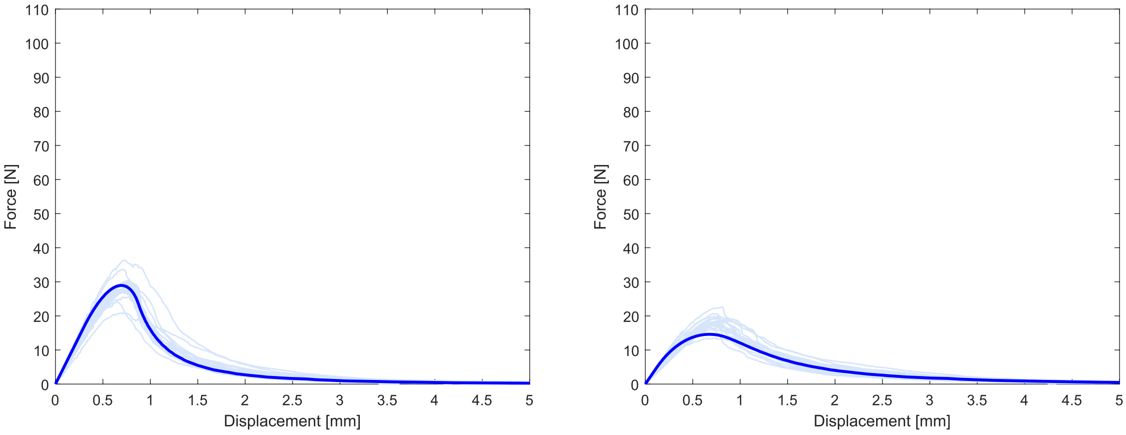

(c) Spruce - rectangular notch.

(d) Spruce - triangular notch.

Fig. 11 Numerical load–displacement curves plotted in conjunction to experimental load–displacement curves. Legend valid for all plots

Table 7 Evaluated fracture energies for the different test series

	Rectangular	Triangular	All
Spruce	188 (11%)	257 (14%)	222 (20%)
Birch	700 (17%)	611 (19%)	657 (19%)

All fracture energies are evaluated with the measured fracture area, as described in Section "Experimental testing". Fracture energy in J/m^2. Coefficient of variation in parenthesis

value; 213 J/m^2 with a moisture content of around 12%. Slightly higher values of the fracture energy for spruce has been established by e.g., Riberholt et al. (1992) and Stefansson (2001), where a fracture energy of 298 and 283 J/m^2 was acquired, respectively.

A clear outlier can be identified for the S43 series. This outlier corresponds to specimen S4320, (see Online Resource 1), and did have a slight deviation in fiber orientation compared to the other specimens. It is however difficult to assess the exact reason for this deviation, but one explanation could be that there was a nearby knot in the timber board, in turn causing deviation in the fibers.

The fracture energies for the birch series, B and TB, were evaluated to 700 and 611 J/m^2, respectively, see Table 7. Forsman et al. (2021) determined the fracture energy of birch for five different series, each conditioned in different relative humidity. Four out of five series were either very wet or very dry, and as such not comparable to the present work. However, one series had a moisture content of 13.6%, which is close to the MC in the present work. For this moisture content, the fracture energy was evaluated to 460 J/m^2. Compared to this, the values acquired in the present work are markedly higher. It should however be noted, a larger quantity of specimens has been evaluated in the present work. In addition, the discrepancy between these values could in part be explained by the natural variation of mechanical properties in wood.

Effect of density and moisture content

The density in relation to the fracture energy for all specimens, both spruce and birch, is shown in Fig. 12. The density of the spruce specimens showed a small variation, see Table 3. The coefficient of variation in specific fracture energy for the S43- and TS43-series was 3.3% and 1.5%, respectively. This can most likely be explained by the fact that all spruce specimens originated from the same timber

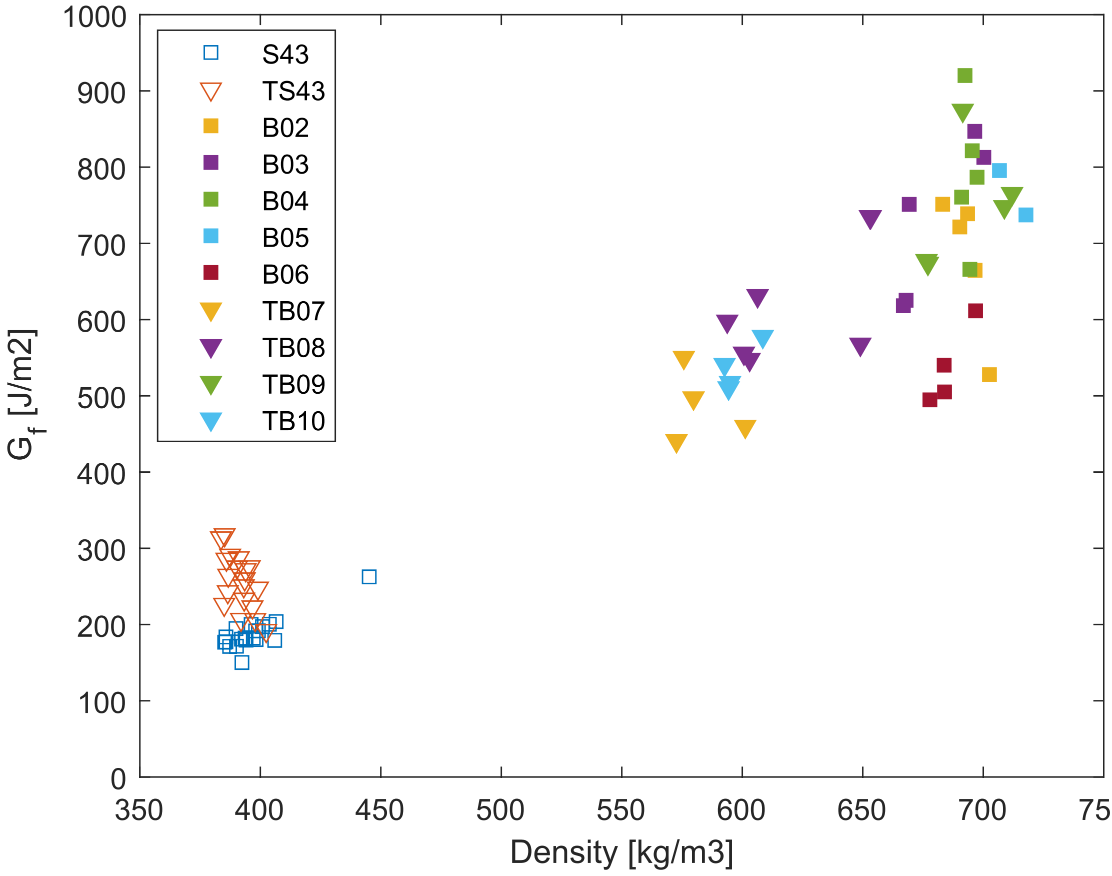

Fig. 12 Fracture energy in relation to density for all specimens

board. As such, all spruce specimens were extracted in a perfectly sequential order from the same timber piece, with the exception of the exclusion of specimens containing knots and/or other imperfections. For the two spruce series, the only large deviation in density was from the previously mentioned outlier, S4320, which did have a quite high density compared to the other specimens (see Fig. 12).

The birch specimens were, in contrast to the spruce specimens, created from nine different timber pieces. The B-series was created from four timber pieces, and the TB-series from five timber pieces. However, the B-series still does display a very low CoV in density, only 1.9%. In comparison, the TB-series displays the largest CoV in density of all series, at 8.9%. This makes it difficult to draw any conclusions with regards to how the density and the fracture energy are correlated, since only one series had a larger variation in density. As a comparison, the work by Forsman et al. (2021) evaluated the fracture energy with the same method as in the present work. In comparison, the mean density of birch was evaluated to 647 kg/m^3, which is similar to the density for all specimens in the present work (660 kg/m^3).

In addition to density, the moisture content (MC) was evaluated for all specimens, since previous work (Reiterer et al. 2002; Tukiainen and Hughes 2016; Forsman et al. 2021) indicates that there is a dependency between the MC and the fracture energy. The relation between MC and fracture energy from the specimens in the present work is shown in Fig. 13. The mean values of MC of the S43 and TS43-series were 14.2% and 14.5%, respectively. The previously mentioned outlier with regard

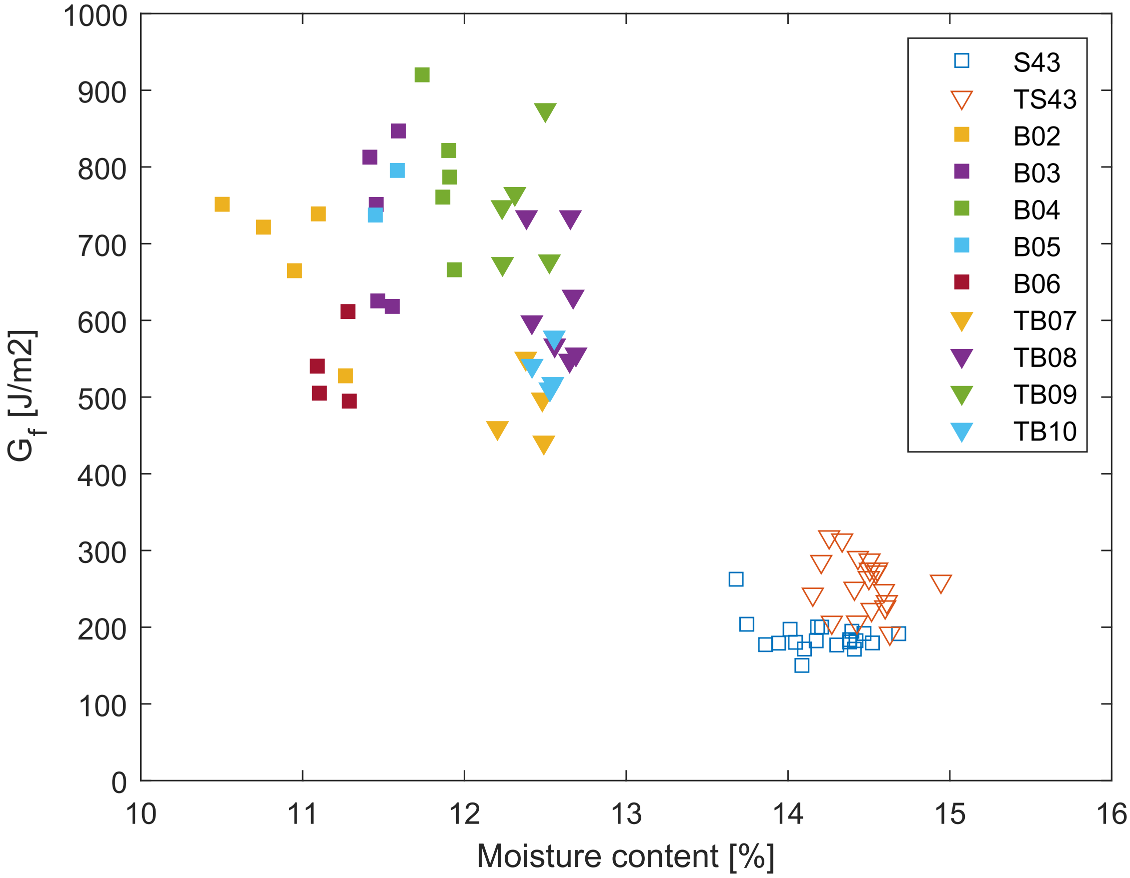

Fig. 13 Fracture energy in relation to the moisture content for all specimens

to density, S4320, was also a slight outlier with regard to moisture content. It did have the lowest moisture content of all specimens in the series S43. Both the S43 and TS43-series showed a low variation in moisture content, as shown in Table 3. The B-series had a mean moisture content of 11.4% and the TB-series a mean moisture content of 12.5%. The coefficient of variation for the B-series was almost as low as for the spruce series—3.4%, whereas for the TB-series it was lower than both of the two spruce series: 1.2%.

The dependency between moisture content and fracture energy seems in general to be more pronounced for larger differences in moisture content. For a moisture content in common structural applications, i.e., 8–16%, the change in fracture energy seems to be relatively small, based on previous research (Tukiainen and Hughes 2016; Forsman et al. 2021; Reiterer and Stanzl-Tschegg 2002). Hence, the small difference in moisture content between species should not affect the comparison in fracture energy between species.

Effect of notch geometry and fracture area

As is evident from Fig. 14 and Table 7, the effect of the notch geometry on the evaluated fracture energy is not systematic between spruce and birch specimens. For the spruce specimens, the triangular fracture area yields an increase in the mean value of the evaluated fracture energy, whereas for the birch specimens, the triangular

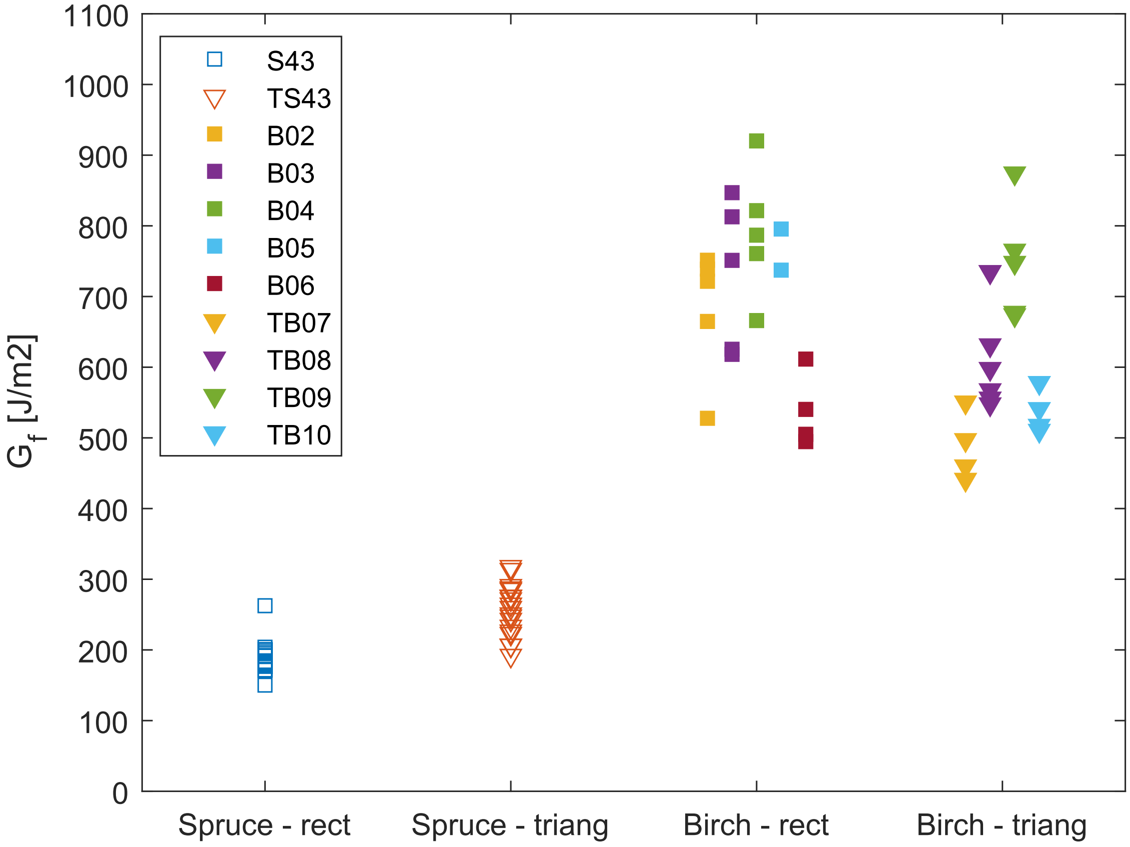

Fig. 14 Evaluated fracture energy for the different test series

fracture area instead yields a reduction. A factor that could influence this is potentially the annual ring orientation.

The annual ring orientations for the two spruce series were not perfect. For the spruce specimens with a rectangular fracture area, an orientation very similar to a perfect TL-system was acquired. However, for the spruce specimens with a triangular fracture area, the deviation from a pure TL-system was roughly 17–18°. For the birch specimens, the deviation from a pure TL-system seemed to be smaller than for the spruce specimens, and no consistent effect on the fracture energy could be identified. However, identifying the annual ring orientation was somewhat more difficult for the birch specimens.

The fracture energy in the present work was not evaluated with the nominal area, but instead with the measured fracture area, A_{real}, as measured with GIMP, cf. Section 2. As seen in Table 4, A_{real}, for the spruce specimens was fairly close to the nominal area. However, for the birch specimens, the deviation in mean of A_{real}, compared to the nominal area, was much larger. In addition, the variation in A_{real} was higher for the birch specimens compared to the spruce specimens. This is likely an artefact from the manufacturing process. In addition, it should be noted, that the variation in A_{real} for the triangular fracture area (see Table 4), is higher for both the spruce and birch specimens, compared to the specimens with a rectangular fracture area, which might imply additional uncertainties when manufacturing the specimens with the triangular fracture area.

When manufacturing specimens with the triangular fracture area, the sawing of the triangular notch is the most crucial moment. Since two cuts are needed to create the triangular notch, several difficulties are introduced. After the first cut is made, the specimen is rotated 90° around its longitudinal axis, and cut a second time. If alignment, orientation and rotation is not executed with high precision, the second cut might not enter the specimen in the same plane as the first cut. As a consequence, multiple cracks could propagate instead of the intended single crack, possibly resulting in a greater value of the evaluated fracture energy. However, this does not seem to be a systematic error occurring in the present work; if it was, a systematic increase in evaluated fracture energy would likely have been acquired for the specimens with a triangular fracture area.

For both the spruce and birch specimens, a *t*-test showed a significant difference between the means of the fracture energy between the series with a triangular vs. rectangular fracture area. The *p*-value for the *t*-test between the two spruce series was $1.06 \cdot 10^{-8}$, implying a significant difference between the two series. For the birch-series the *p*-value was 0.02, still implying a difference in mean between the two series.

Experimental versus numerical load displacement curves

In addition to the experimental testing, a small set of simplified numerical simulations was carried out in the present work, where the Young's modulus in the tangential direction (E_{T}) of the middle piece was manually fitted to ensure that the elastic region of the numerical load–displacement curves matched the experimental elastic region well. E_T was manually fitted to 1000, 620, 350 and 200 MPa, for the B-, TB, S-, and TS-series, respectively. The numerical load–displacement curves corresponding to these values of E_T combined with the other mechanical parameters in Table 6 and the fracture energy in Table 7 are shown in Fig. 11. As can be seen, the numerical model is in reasonable agreement with the experimental load–displacement curves, capturing also the influence of the shape of the fracture area. To achieve a well fitting elastic region for the specimens with a triangular fracture area, the tangential Young's modulus has to be markedly lower compared to the specimens with a rectangular fracture area. This is explained by the fact that the numerical model for the specimens with a triangular fracture area is based on the same 2d-geometry as the specimens with a rectangular fracture area. Consequently, without lowering the value of E_T, the stiffness of the model with triangular fracture area is too high, especially close to the lower edge of the fracture area. As such, it is important to note that the simulations carried out in the present work, need further work, potentially by creating three dimensional models, or by modifying the two-dimensional models in such a way that the stiffness of the specimens with a triangular fracture area is properly accounted for.

In addition, the peak load is slightly too low for all series except for the spruce specimens with a rectangular fracture area. This implies that the tensile strength values that have been adopted from the literature might be too conservative in comparison to the tensile strengths of the tested material, both for spruce and birch.

Conclusion and outlook

In the present work, the specific fracture energy for birch and spruce was evaluated by means of the Nordtest method. In addition, the effect of different notch geometries on the evaluation of the specific fracture energy was studied. Following the previous discussion, the main conclusions of the work are:

- The specific fracture energy was evaluated to 221 J/m^2 for the spruce specimens, and to 656 J/m^2 for the birch specimens, averaged over all specimens of the respective species.
- When evaluating the stability of the tests in terms of the suggested load drop criterion, the spruce specimens seem to be markedly more unstable compared to the birch specimens.
- An influence on evaluated fracture energy of the shape of the fracture area was found.
- With a low variation in density for three out of four test series, it is difficult to draw any conclusions with regards to how the density and fracture energy are correlated.
- For the specimen size adopted in the present work, the triangular fracture area was not necessary, sufficient stability could be achieved with a rectangular fracture area.
- With what seems to be a marked increase in fracture energy for birch, compared to spruce, current design codes might need revision and rework to account for

> this. In addition, the increase in fracture energy can potentially indicate higher load-carrying capacity in e.g., connections, or beams with notches or holes.

Since determining the specific fracture energy of birch still is a novel area, it would be beneficial to evaluate the fracture energy of birch grown in different geographical locations, but also in different parts of a single tree, to properly assess how much the fracture energy varies. In addition, studying the effect on the fracture energy from e.g., distance to pith and annual ring orientation would be interesting.

Future numerical work could also use the results of the experimental tests to determine the softening behavior of birch, with an optimization method. This could extend the use of the SENB method to not only determine the specific fracture energy, but also to determine the softening behavior. Since the softening behavior is partly governed by the tensile strength, a calibration of such models would also yield an estimation of the tensile strength of birch in tension perpendicular to grain.

In Section "Materials and methods", it was mentioned that the effect of plastic dissipation on the evaluation of fracture energy is negligible for sufficiently small specimens. However, this effect has previously only been evaluated for specimens with a rectangular fracture area. It would be of interest to quantify this effect in the specimens with a triangular fracture area as well, since the plastic effects might be different due to the different specimen geometry.

Supplementary Information The online version contains supplementary material available at https://doi.org/10.1007/s00226-024-01595-6.

Acknowledgements The financial support from FORMAS for the project Strength and fracture analysis of laminated wood-based structural elements (Grant 2023-01161), the Södra Foundation for Research, Development and Education (Grant 2021-283), the ÅForsk Foundation (reference number 22-50) and the Crafoord Foundation (reference number 20220805) are gratefully acknowledged.

Author contributions JJ: Conceptualization, methodology, software, investigation, validation, writing—original draft, laboratory work. HD: Conceptualization, methodology, investigation, writing—review and funding. ES: Conceptualization, methodology, investigation, writing—review and funding.

Funding Open access funding provided by Lund University.

Data availability Data made available upon request.

Declarations

Conflict of interest The authors declare no potential Conflict of interest with respect to the research, authorship, and/or publication of this article.

Open Access This article is licensed under a Creative Commons Attribution 4.0 International License, which permits use, sharing, adaptation, distribution and reproduction in any medium or format, as long as you give appropriate credit to the original author(s) and the source, provide a link to the Creative Commons licence, and indicate if changes were made. The images or other third party material in this article are included in the article's Creative Commons licence, unless indicated otherwise in a credit line to the material. If material is not included in the article's Creative Commons licence and your intended use is not permitted by statutory regulation or exceeds the permitted use, you will need to obtain permission directly from the copyright holder. To view a copy of this licence, visit http://creativecommons.org/licenses/by/4.0/.

References

Bodig J, Jayne BA (1982) Mechanics of wood and wood composites. Van Nostrand Reinhold, New York

Collins S, Fink G (2022) Mechanical behaviour of sawn timber of silver birch under compression loading. Wood Mater Sci Eng 17(2):121–128. https://doi.org/10.1080/17480272.2020.1801836

Conrad PCM, Smith DG, Fernlund G (2003) Fracture of solid wood: a review of structure and properties at different length scales. Wood Fiber Sci 35(4):570–584

Dahl K (2009) Mechanical properties of clear wood from Norway spruce. PhD Thesis, Department of Structural Engineering, Norwegian University of Science and Technology

Danielsson H (2013) Perpendicular to grain fracture analysis of wooden structural elements: models and applications. PhD thesis, Division of Structural Mechanics, Lund University

Dassault (2019) Abaqus/CAE

de Moura MFSF, Dourado N (2018) Wood fracture characterization, 1st edn. CRC Press, Boca Raton

Dinwoodie J (2002) Timber: its nature and behaviour. CRC Press, London

Dlouhý I, Boccacini AR (2001) Reliability of the chevron notch technique for fracture toughness determination in glass composites reinforced by continuous fibres. Scr Mater 44:531–537. https://doi.org/10.1016/S1359-6462(00)00601-1

Dourado N, Morel S, de Moura MFSF, Valentin G, Morais J (2008) Comparison of fracture properties of two wood species through cohesive crack simulations. Compos A 39(2):415–427. https://doi.org/10.1016/j.compositesa.2007.08.025

Dourado N, de Moura MFSF, Morel S, Morais J (2015) Wood fracture characterization under mode I loading using the three-point-bending test. Experimental investigation of *Picea abies* L. Int J Fract 194:1–9. https://doi.org/10.1007/s10704-015-0029-y

EN 1995-1-1:2004 (2004) Eurocode 5: design of timber structures: part 1-1: General—common rules and rules for buildings

Forsman K, Fredriksson M, Serrano E, Danielsson H (2021) Moisture-dependency of the fracture energy of wood: a comparison of unmodified and acetylated scots pine and birch. Holzforschung 75(8):731–741. https://doi.org/10.1515/hf-2020-0174

Gustafsson PJ (1988) A study of strength of notched beams. In: Proceedings CIB-W18 meeting 21, Paper CIB-W18/21-10-1, Parksville, Canada

Hearmon RFS (1961) An introduction to applied anisotropic elasticity. Oxford University Press, London

Heräjärvi H (2004) Static bending properties of Finnish birch wood. Wood Sci Technol 37:523–530. https://doi.org/10.1007/s00226-003-0209-1

Jeitler G, Augustin M, Schickhofer G (2016) BIRCH | GLT+CLT: mechanical properties of glued laminated timber and cross laminated timber produced with the wood species birch. In: Proceedings of world conference on timber engineering (WCTE 2016), August 22–25, Vienna Austria, Article MS1-07:2

Karihaloo BL (1995) Fracture mechanics and structural concrete. Longman Scientific and Technical, Harlow

Kollman FFP, Kuenzi EW, Stamm AJ (1968) Principles of wood science and technology 1: solid wood. Springer, Berlin

Kollman FFP, Kuenzi EW, Stamm AJ (1975) Principles of wood science and technology 2: wood based materials. Springer, Berlin

Lemke U, Johansson M, Ziethén R, Briggert A (2023) New criteria for visual strength grading of sawn timber from birch grown in Sweden. In: Proceedings of world conference on timber engineering (WCTE 2023), June 19–22 2023, Oslo, Norway https://doi.org/10.52202/069179-0102

Niemz P, Teischinger A, Sandberg D (2023) Springer handbook of wood science and technology. Springer, Cham

Nordtest (1993) Wood: fracture energy in tension perpendicular to the grain. Technical Standard

Obernosterer D, Jeitler G (2020) Birch for engineered timber products. In: Proceedings of world conference on timber engineering (WCTE 2020), August 9-12 2021, Santiago, Chile, Article WPC0203

Ostapska K, Malo KA (2020) Wedge splitting test of wood for fracture parameters estimation of Norway spruce. Eng Fract Mech 232:107024. https://doi.org/10.1016/j.engfracmech.2020.107024

Persson K, Gustafsson PJ, Petersson H (1993) Influence of plastic dissipation on apparent fracture energy determined by a three-point bending test. Report TVSM-7084, Division of Structural Mechanics, Lund University

Reiterer A, Sinn G, Stanzl-Tschegg SE (2002) Fracture characteristics of different wood species under mode I loading perpendicular to the grain. Mater Sci Eng, A 332(1):29–36. https://doi.org/10.1016/S0921-5093(01)01721-X

Reiterer A, Stanzl-Tschegg SE (2002) The influence of moisture content on the mode I fracture behavior of sprucewood. J Mater Sci 37:4487–4491. https://doi.org/10.1023/A:1020610231862

Riberholt H, Enquist B, Gustafsson PJ, Jensen R (1992) Timber beams notched at the support. Report TVSM-7071, Division of Structural Mechanics, Lund University

Sheikh S, M'Saouboi R, Flasar P, Schwind M, Persson T, Yang J, Llanes L (2015) Fracture toughness of cemented carbides: testing method and microstructural effects. Int J Refract Met Hard Mater 49:153–160. https://doi.org/10.1016/j.ijrmhm.2014.08.018

SLU (2022) Skogsdata 2022. Technical report. https://www.slu.se/globalassets/ew/org/centrb/rt/dokument/skogsdata/skogsdata_2022_webb.pdf. Accessed 13 Aug 2024

Smith I, Landis E, Gong M (2003) Fracture and fatigue in wood. John Wiley and Sons, West Sussex

Stanzl-Tschegg SE, Tan DM, Tschegg E (1995) New splitting method for wood fracture characterization. Wood Sci Technol 19:31–50. https://doi.org/10.1007/BF00196930

Stefansson F (2001) Fracture analysis of orthotropic beams: linear elastic and non-linear methods. Licenciate thesis, Division of Structural Mechanics, Lund University

The GIMP Development Team (2019) GIMP. https://www.gimp.org

Thelandersson S, Larsen HJ (2003) Timber engineering. John Wiley and Sons, New York

Tukiainen P, Hughes M (2013) The fracture behavior of birch and spruce in the radial-tangential crack propagation direction at the scale of the growth ring. Holzforschung 67(6):673–681. https://doi.org/10.1515/hf-2012-0139

Tukiainen P, Hughes M (2016) The effect of temperature and moisture content on the fracture behaviour of spruce and birch. Holzforschung 70(4):369–376. https://doi.org/10.1515/hf-2015-0017

Wang T, Want Y, Crocetti R, Wålinder M (2022a) Influence of face grain angle, size, and moisture content on the edgewise bending strength and stiffness of birch plywood. Mater Des 223:111227. https://doi.org/10.1016/j.matdes.2022.111227

Wang T, Want Y, Crocetti R, Wålinder M (2022b) In-plane mechanical properties of birch plywood. Constr Build Mater 340:127852. https://doi.org/10.1016/j.conbuildmat.2022.127852

Publisher's Note Springer Nature remains neutral with regard to jurisdictional claims in published maps and institutional affiliations.

Paper II

Estimation of mode I fracture parameters in wood using likelihood-based inference

Johannes Jonasson[1], Johan Lindström[2], Henrik Danielsson[1], and Erik Serrano[1]

[1]Department of Construction Sciences, Lund University, Sweden.

[2]Centre for Mathematical Sciences, Lund University, Sweden.

Abstract

Despite a recent increased interest in utilizing the hardwood birch in structural applications, knowledge with respect to failure and fracture behaviour is still scarce. Failure and fracture behaviour need to be well understood, in order to ensure a safe and material-efficient design practice. The fracture behaviour is mainly governed by three material parameters: stiffness, strength and specific fracture energy. The strength and the fracture energy also govern the softening behaviour, which describes how a material absorbs energy as cracks propagate. In the present work, we characterize all three relevant fracture parameters through a single experimental test by minimising different cost functions. Two popular cost functions often used in finite element model updating (FEMU) are reformulated in the context of maximum likelihood theory. It is shown that neither cost function can recover the variability found in the experiments. However, the mean behaviour is recovered fairly well for both cost functions. This study contributes with new knowledge with respect to the fracture behaviour of birch, which enables further simulations of the behaviour of load-bearing structures at a larger, semi-structural, or structural scale.

1 Introduction

1.1 Fracture in wood

In recent years, the interest in utilizing birch in structural applications has been growing (Jonasson et al., 2024b; Obernosterer et al., 2023; Wang et al., 2022a, 2022b). This is in part due to higher stiffness and strength, compared to conventionally used wood species, such as Norway spruce. However, increased stiffness and strength might be followed by increased material brittleness, which might markedly affect the failure behaviour of load-bearing structures. Thus, if birch is to be utilised to a greater extent in structural applications, the failure behaviour and the brittleness need to be well understood to ensure a safe and material-efficient design practice.

Wood is a material which exhibits large variations in constitutive behaviour in different orientations, and as a consequence, the fracture behaviour can be rather complex. In general, the constitutive behaviour of wood is described in terms of three principal directions: the fibre direction, denoted L, the tangential direction, denoted T, and the radial direction, denoted R. Based on these directions, six different crack propagation systems can be identified in wood: LR, RL, TL, LT, RT and TR. In these systems, the first letter denotes the direction normal to the crack plane, whereas the second letter denotes the direction of crack propagation. Cracks propagating in the TL- and RL-systems might occur when tensile stresses arise perpendicular to the grain, which are common in beams with holes or notches, or in wooden joints (Thelandersson & Larsen, 2003, Chap 7). To properly understand how such structural solutions behave when utilizing birch instead of Norway spruce, the fracture behaviour needs to be well understood.

The fracture behaviour of birch has not been exhaustively studied, but efforts have been made to characterize it. For example, Tukiainen and Hughes (2013, 2016) carried out studies of the fracture behaviour of birch in the RT and TR crack propagation systems. In addition, both Jonasson et al. (2024a) and Forsman et al. (2021) used single-edge-notched beam (SENB) specimens to evaluate the specific fracture energy of birch with the Nordtest method (Nordtest, 1993) for mode I loading in the TL crack propagation system. In general, the conclusion seems to be that birch has a substantially higher fracture energy compared to spruce. However, the fracture energy is not the only important material parameter to consider; the stiffness and strength are also important in the context of fracture.

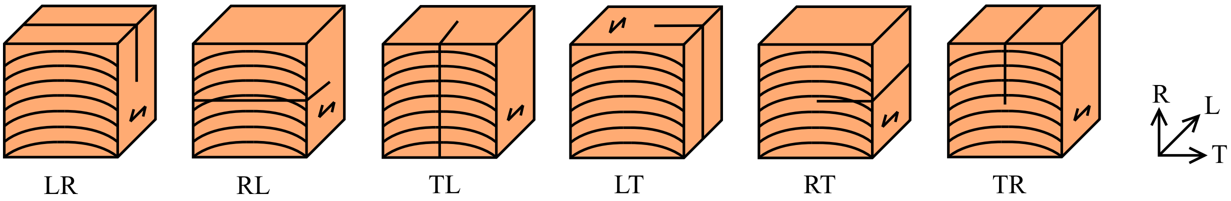

Figure 1: The six different crack propagation systems in wood.

The *characteristic length* is a quantity that characterizes the ductility, i.e. the inverse of the brittleness, according to:

$$l_{\mathrm{ch}} = \frac{EG_{\mathrm{f}}}{f_{\mathrm{t}}^2} \tag{1}$$

where E is the modulus of elasticity, G_{f} is specific the fracture energy and f_{t} is the tensile strength. Here, Equation 1 relates to the behaviour of the material in pure tension (mode I). To determine the stiffness and tensile strength experimentally, a direct tension test can be carried out. To determine the fracture energy, SENB specimens loaded in three-point-bending is a well-established experimental method. The SENB method has been adapted for wood specifically in the so-called Nordtest method (Nordtest, 1993). The Nordtest method is very convenient to use, mainly due to two factors: firstly, it only requires recording of the displacement and the force, and secondly, it can be used for small specimens, without affecting the evaluated fracture energy. Using smaller specimens is important to ensure stable crack propagation, meaning that no snap-back behaviour or sudden load-drops occur in the force-displacement curves. Comparatively, the R-curve concept and similar methods based on linear elastic fracture mechanics (LEFM) break down when the fracture process zone (FPZ) is large in comparison to the characteristic size of the specimen, which violates the fundamental assumptions of LEFM. As such, methods based on LEFM are not suitable for smaller quasi-brittle specimens which exhibit a large FPZ in relation to the specimen size. This has previously been shown by e.g. Dourado et al. (2008). In addition, if larger specimens would be used, enabling the use of LEFM theory, the evaluation of the fracture energy may be incorrect due to plastic dissipation in the bulk material outside of the FPZ (Persson et al., 1993).

1.2 Finite element model updating

Finite element (FE) models play a crucial part in engineering sciences when it comes to understanding, developing, calibrating, and validating material models. Calibration of numerical models after experiments is an inverse problem (Aster et al., 2013, Chap 1), and when FE models are used the procedure is commonly called "finite element model updating" (FEMU) in the literature (Chen et al., 2024). FEMU is most commonly based upon minimising some difference between the experimental and numerical responses, such as load-displacement curves or strain fields. The minimisation is often carried out with mathematical optimisation procedures, such as the simplex method (Bondsman & Peplow, 2024; Kunecký et al., 2024), gradient-based methods, genetic algorithms (Dourado et al., 2008), particle swarms (Mthembu et al., 2011) or Bayesian optimisation (BO) strategies (Do & Ohsaki, 2022). The latter is a well-established method for optimizing expensive-to-evaluate cost functions, which generally is the case for FEMU, where the FE model has to be continuously evaluated during the optimisation process. In addition, several studies (Raviolo et al., 2023, 2024) have indicated that BO is a powerful optimisation procedure in the context of FEMU, requiring a relatively small amount of FE evaluations compared to e.g. genetic algorithms.

Efforts to estimate constitutive and cohesive parameters in wood by inverse parameter estimation or FEMU have been carried out for several decades, even though these names have not explicitly been used. For example, Boström (1992) estimated the strain-softening behaviour in wood using methods of non-linear fracture mechanics. He showed that the softening behaviour of Scots pine could be determined directly from experimental tests, such as direct tension or direct shear tests, without the use of FE models. Howver, this typically requires small specimen and a stiff testing machine.

More recent work on parameter estimation has been carried out by De Moura et al. (2008) and Dourado et al. (2008, 2015), where an inverse problem was formulated to determine the cohesive law for various wood species. By adopting an optimisation approach which minimises the difference between the numerical and the experimental load-displacement curves through a genetic optimisation algorithm, the optimal softening behaviour could be established. However, the obtained softening behaviour was deterministic. For a material like wood, which exhibits large variability with respect to the constitutive parameters, it would be beneficial if such variability could be captured by the optimisation procedure.

A similar approach was considered by Kunecký et al. (2024), where a multi-start simplex method was used to minimise the integral of the absolute difference between the experimental and numerical load-displacement curves to determine the softening parameters of spruce. A rather distinct drawback with this method is the amount of FE calculations it required: more than 100 000. In cases where the FE model is expensive to evaluate, it follows that the cost function is also expensive to evaluate. In such circumstances, performing tens of thousands of function evaluations might prove unfeasible due to computational demands.

1.3 Aim and objectives

It is clear that the increased stiffness and strength in birch might contribute to improvements in load-bearing structures. However, to properly assess if such structures can be improved, it is quintessential to properly understand the fracture behaviour. In the present work, we use FEMU in conjunction with likelihood-based inference to estimate a non-deterministic set of fracture parameters for two European wood species: Norway spruce and birch. Two commonly adopted force-based cost functions in FEMU are reformulated based on the theory of likelihood inference. It is shown that neither of these two cost functions can accurately recover the variance of the experimental load-displacement curves.

2 Theoretical background

2.1 Bayesian optimisation

As outlined in the Introduction, Bayesian optimisation is a well-established method for optimizing cost functions that are expensive to evaluate (Garnett, 2023), and has been utilised in a number of works to establish constitutive behaviours in various settings. For example, Kuhn et al. (2022) determined material parameters in small strain crystal plasticity using a Bayesian optimisation procedure. Karandikar et al. (2022) estimated constitutive parameters in the Johnson-Cook flow stress model by using a modified Bayesian optimisation procedure, and Do and Ohsaki (2022) used Bayesian optimisation to establish constitutive parameters in cyclic elasto-plastic loading.

Bayesian optimisation can be viewed as a sequential optimisation algorithm, where an initial (potentially empty) data-set, $\mathcal{D}_i$, is sequentially updated at each iteration. At each iteration i, the cost function, denoted $f(\mathbf{x})$, is sampled at a new point, $\mathbf{x}_i$, and the corresponding function value, y_i, is evaluated. The choice of which point to sample is made by combining the knowledge from all previous iterations through a so-called *acquisition function*, $\alpha(\mathbf{x})$. The acquisition function is often constructed based on a Gaussian process (GP), denoted $g(\mathbf{x})$, which approximates the cost function. The sequential procedure is continued until termination which in BO often is a max budget with respect to the total number of iterations, denoted $n_{\max}$. In Algorithm 1, the Bayesian optimisation procedure is conceptually illustrated through a pseudo-code algorithm.

Algorithm 1 Pseudo-algorithm for Bayesian optimisation.

```
Input: $f(\mathbf{x})$, $\mathcal{D}_i$, $\alpha(\mathbf{x})$, $n_{\max}$, $n_{\text{pre}}$
  Sample $n_{\text{pre}}$ points $\mathbf{x}_i,\ i = 1, \ldots, n_{\text{pre}}$
  Create $\mathcal{D} = \bigcup_{i=1}^{n_{\text{pre}}} \{\mathbf{x}_i, f(\mathbf{x}_i)\}$
  $i \leftarrow n_{\text{pre}}$
  while $i < N_{\max}$ do
      Use $\mathcal{D}$ to create GP approximation, $g(\mathbf{x})$, and acquisition function $\alpha(\mathbf{x})$.
      $x_{i+1} \leftarrow \operatorname{argmin} \alpha(\mathbf{x})$      ▷ Choose next point to sample based on acquisition function.
      $y_{i+1} \leftarrow f(\mathbf{x}_{i+1})$      ▷ Evaluate cost function at next sample point.
      $\mathcal{D} \leftarrow \mathcal{D} \cup \{x_{i+1}, y_{i+1}\}$      ▷ Update data-set.
      $i \leftarrow i + 1$
  end while
```

2.2 Gaussian process regression

A Gaussian process, g, is a stochastic process which is completely defined by its mean function and its covariance function, according to

$$g \sim \mathcal{GP}(m(\mathbf{x}), k(\mathbf{x}, \mathbf{x}')) \tag{2}$$

where $m(\mathbf{x})$ is the mean function and $k(\mathbf{x}, \mathbf{x}')$ is the covariance function. Here, $\mathbf{x}$ and $\mathbf{x}'$ denote two (potentially different) feature vectors in the feature space with n_{dim} elements. In the general case, the arguments to the covariance function may be a number of feature vectors collected in a matrix, $\mathbf{X}$, such that

$$\mathbf{X} = \begin{bmatrix} \mathbf{x}_1 & \mathbf{x}_2 & \dots & \mathbf{x}_n \end{bmatrix}^\intercal \tag{3}$$

Here $\mathbf{X}$ is a $n \times n_{\text{dim}}$ matrix with one of the n feature vectors on each row. As such, the covariance function $k(\mathbf{X}, \mathbf{X})$ evaluates the covariance for all combinations of rows in $\mathbf{X}$ resulting in an $n \times n$ covariance matrix Σ where the element at location i, j is the covariance between feature vectors i and j or

$$k(\mathbf{X}, \mathbf{X}) = \Sigma \tag{4}$$

$$k(\mathbf{x}_i, \mathbf{x}_j) = \Sigma_{ij} \tag{5}$$

Different types of covariance functions will be described later in this section.

A single observation of the process, denoted y_i, may be distorted by independent and identically distributed Gaussian noise, denoted ε:

$$y_i = g(\mathbf{x}_i) + \epsilon, \;\; \epsilon \sim \mathcal{N}(0, \sigma_n^2) \tag{6}$$

An observation set, $\mathcal{D}_i$, thus consists of the set of an observed feature vector and the corresponding observed function value, such that $\mathcal{D}_i = \{\mathbf{x}_i, y_i\}$. All observed feature vectors may then be collected in a matrix, denoted $\mathbf{X}$, see Equation 3. The corresponding function values may be collected in a column vector, denoted $\mathbf{y}$:

$$\mathbf{y} = \begin{bmatrix} y_1 & y_2 & \dots & y_n \end{bmatrix}^\intercal \tag{7}$$

The collection of feature vectors in $\mathbf{X}$ is called *training points*, and $\mathbf{y}$ is called *training values*. Further, we assume that we have a set of feature vectors for which we wish to use the observations to infer their corresponding function values. These feature vectors are collected in a matrix $\mathbf{X}_*$, and denoted *test points*. The unknown function values are collected in a column matrix, $\mathbf{g}_*$, and denoted *test values*. The test values are approximations of the true cost function, such that $\mathbf{g}_* \approx f(\mathbf{x}_*)$. For simplicity, we will assume that we only have a single test point, such that $\mathbf{X}_* = \mathbf{x}_*$ is a single point, and $\mathbf{g}_* = g(\mathbf{x}_*)$ is the corresponding function value. Assuming a prior mean of zero, the joint distribution of the Gaussian process for both the training points and the single test point is:

$$\begin{bmatrix} \mathbf{y} \\ g_* \end{bmatrix} \sim \mathcal{N}\left(\mathbf{0}, \begin{bmatrix} \mathbf{K}_y & k(\mathbf{X}, \mathbf{x}_*) \\ k(\mathbf{X}, \mathbf{x}_*)^\mathsf{T} & k(\mathbf{x}_*, \mathbf{x}_*) \end{bmatrix}\right), \quad \mathbf{K}_y = k(\mathbf{X}, \mathbf{X}) + \sigma_n^2 \mathbf{I} \tag{8}$$

Here $\bullet^\mathsf{T}$ denotes the transpose of a matrix or vector. $\mathbf{K}_y$ is thus of dimension $n \times n$, $k(\mathbf{X}, \mathbf{x}_*)$ of dimension $n \times 1$, and $k(\mathbf{x}_*, \mathbf{x}_*)$ of dimension 1×1, i.e. scalar. Based on the joint Gaussian distribution, the posterior Gaussian distribution for g_* is:

$$g_* | \mathbf{X}, \mathbf{y}, \mathbf{x}_* \sim \mathcal{N}(\mu(\mathbf{x}_*), \sigma^2(\mathbf{x}_*)) \tag{9}$$

where

$$\mathbb{E}[g_* | \mathbf{X}, \mathbf{y}, \mathbf{x}_*] = \mu(\mathbf{x}_*) = k(\mathbf{X}_*, \mathbf{X}) \mathbf{K}_y^{-1} \mathbf{y} \tag{10a}$$

$$\mathbb{V}[g_* | \mathbf{X}, \mathbf{y}, \mathbf{x}_*] = \sigma^2(\mathbf{x}_*) = k(\mathbf{x}_*, \mathbf{x}_*) - k(\mathbf{x}_*, \mathbf{X}) \mathbf{K}_y^{-1} k(\mathbf{X}, \mathbf{x}_*) \tag{10b}$$

The above expressions are valid for making predictions at a single point, but are also valid for multiple points when $\mathbf{x}_*$ is replaced with a matrix of feature vectors instead of a single feature vector.

The covariance function is commonly called *the kernel.* All stationary kernels may be expressed as a function of some measure of distance between points and may be isotropic or anisotropic. For anisotropic kernels, the measure of distance can be expressed as

$$r = \sqrt{(\mathbf{x} - \mathbf{x}')^\mathsf{T} \mathbf{A} (\mathbf{x} - \mathbf{x}')} \tag{11}$$

where $\mathbf{A}$ is a positive semi-definite matrix. If $\mathbf{A}$ is diagonal, the kernel is so-called *axis-aligned*, and the distance is scaled by a length-scale in the direction of each axis, such that $\mathbf{A} = \mathrm{diag}(\mathbf{l})^{-2}$. For isotropic kernels, the length-scale is the same in every direction, such that $\mathbf{A} = l^{-2}\mathbf{I}$.

Perhaps the most commonly used kernel is the squared-exponential (SE) or Gaussian kernel, which may be expressed as a function of the distance r:

$$k(r) = \sigma_v^2 \exp\left(-\frac{1}{2}\frac{r^2}{\rho^2}\right) \tag{12}$$

where σ_v^2 is the signal variance and ρ is a general length-scale parameter. In the following ρ has been set to one since the length-scale already is included in $\mathbf{A}$. The SE kernel is infinitely differentiable, and thus results in an infinitely smooth process, and as such it might not be suitable to model physical behaviour (Rasmussen & Williams, 2006, Chap 4). In addition, it can yield problems with singularities when two observed points are very close to each other (Goulet, 2020, Chap 8). Singularities are however not a problem in most cases, as long as the previously introduced Gaussian noise, ϵ, is employed in the construction of the posterior distribution.

Another popular choice of kernel is the Matérn family of kernels (Matérn, 1986), which can be modeled with different levels of smoothness. The most general definition of a Matérn kernel is:

$$k(r) = \sigma_v^2 \frac{2^{1-\nu}}{\Gamma(\nu)} \left(\sqrt{2\nu} r\right)^{\nu} K_{\nu} \left(\sqrt{2\nu} r\right) \tag{13}$$

where ν is the so called *smoothness* parameter, $\Gamma(\nu)$ is the Gamma function and K_ν is a modified Bessel function of the second kind. The smoothness parameter describes how many times the kernel is differentiable, and when $\nu \to \infty$, the previously described SE kernel is recovered. One of the most common choices for the smoothness parameter is half integers, such that $\nu = k + \frac{1}{2}$ with $k \in \mathbb{Z}$. By choosing the smoothness parameter as a half integer, the Matérn kernel assumes a convenient polynomial form, which in turn avoids the costly Bessel function. Rasmussen and Williams (2006, Chap 4) state that two values of ν are of extra interest in practical applications, namely $\nu = \frac{3}{2}$ and $\nu = \frac{5}{2}$, which yield the following two forms of the Matérn kernel:

$$k_{\nu=3/2}(r) = \sigma_v^2(1 + \sqrt{3}r)\exp(-\sqrt{3}r) \tag{14a}$$

$$k_{\nu=5/2}(r) = \sigma_v^2(1 + \sqrt{5}r + \frac{5}{3}r^2)\exp(-\sqrt{5}r) \tag{14b}$$

It is common to denote the noise parameters, σ_v and σ_n together with the length-scale parameters in $\mathbf{A}$ as *hyper-parameters* and they are usually collected in a vector $\boldsymbol{\lambda} = [\sigma_v \ \sigma_n \ A_{kk}]$. The hyper-parameters are determined by minimising the negative log likelihood of the Gaussian process, defined as

$$\log p(\mathbf{y}|X, \boldsymbol{\lambda}) = -\frac{1}{2}\mathbf{y}^{\mathsf{T}}\mathbf{K}_y^{-1}\mathbf{y} - \frac{1}{2}\log|\mathbf{K}_y| - \frac{n}{2}\log 2\pi \tag{15}$$

2.2.1 Acquisition function

As previously mentioned, Bayesian optimisation may be viewed as a sequential optimisation procedure, which uses the current state of knowledge of the cost function to decide where to sample it next. The choice of the next sampling point is in Bayesian optimisation often used interchangeably with the term *acquisition function.* The most important role of the acquisition function is arguably to approximate the true cost function and its uncertainty. In the present work we adopt the lower confidence bound (LCB) acquisition function, which is formulated as

$$\alpha(\mathbf{x}_*) = \mu(\mathbf{x}_*) - \sqrt{\beta}\sigma(\mathbf{x}_*) \tag{16}$$

where $\mu(\mathbf{x}_*)$ and $\sigma(\mathbf{x}_*)$ are the posterior mean and standard deviation of the GP approximation of the cost function, see Equations 10a and 10b. In addition, β is a scale factor scaling the importance of the

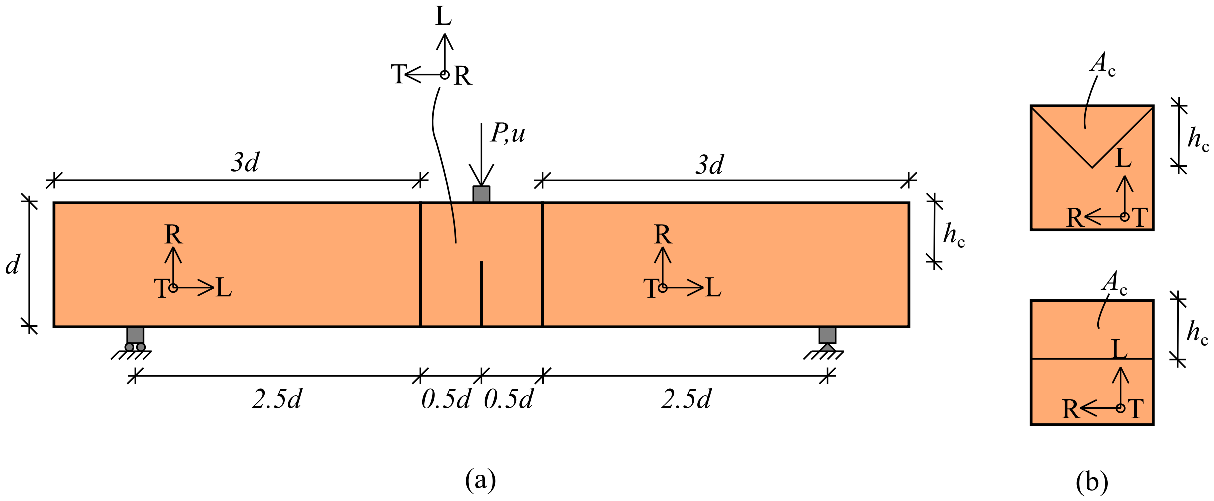

Figure 2: Schematic illustration of the SENB specimen (a) and the two different geometries of the fracture surface (b). In the present work, $d = 20$ mm.

uncertainty (the variance) of the Gaussian process. Thus, it is possible to weigh exploration of high uncertainty regions higher by increasing β.

2.2.2 Termination criteria

The most common termination criterion in Bayesian optimisation is a limited budget of simulations, which is natural when the simulations are very cost-expensive. Another alternative is to stop iterating when the projected best value is no longer likely to improve the best function value by a certain threshold. This may be quantified through the following residual:

$$r = |\frac{y^* - \mu(\hat{\mathbf{x}}_*)}{y^* + \varepsilon_{\text{tol}}}| \leq \varepsilon_{\text{tol}} \tag{17}$$

where y^* is the smallest function value observed thus far, and $\mu(\hat{\mathbf{x}}_*)$ is the smallest function value as projected by the acquisition function at the current iteration. In the present work, we employ the above termination criterion, in combination with a max number of allowable iterations.

2.3 Experimental approach and finite element modelling

The experimental results used in the present work were reported in Jonasson et al. (2024a), where the specific fracture energies of Norway spruce and birch were evaluated according to the Nordtest method, see Figure 2. In the Nordtest method (Nordtest, 1993), a single-edge-notched beam with a pre-sawn notch is loaded in three point bending. A rectangular fracture surface is most commonly adopted in the procedure, however, to ensure post-peak stability during testing, a triangular fracture surface is sometimes employed (Forsman et al., 2021) for brittle materials. The size of the beam, characterised by the measurement d, is in the standard prescribed to 60 mm, but in the present work a dimension of

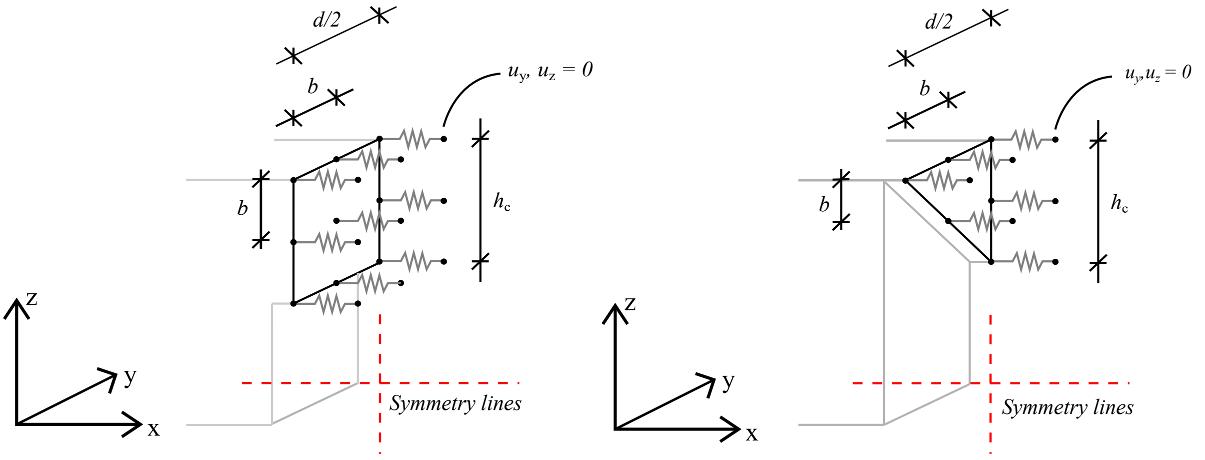

(a) (b)

Figure 3: Schematic illustration (quarter symmetry) of the fracture surfaces for the two notch geometries. b is the FE size, d is the width of the cross-section, and h_{c} is the ligament length.

$d = 20$ mm was adopted. This smaller size was used due to dimensional limitations of the raw birch material, which did not allow for larger dimensions. As previously discussed, this should not affect the evaluated fracture energy when employing non-linear fracture mechanics theory. The two different fracture surfaces are shown in Figure 2b and Figure 3. Based on the tests, the fracture energy could be evaluated using the work-of-fracture method based on the recorded load-displacement (P-u) curves. For a more detailed description of the experimental procedure, the reader is referred to Jonasson et al. (2024a).

The FE modelling was carried out with three-dimensional models, where first-order tetrahedrons were used (C3D4). A cohesive zone modelling approach was implemented by using non-linear springs (SPRING1) to model the strain-softening behaviour in the FPZ. The non-linear springs were located along the pre-defined crack path, see Figure 3. In general, the strain-softening behaviour is modeled by a function which is monotonically decreasing, e.g. linear or bi-linear softening. In the present work, only linear softening has been considered. A stress-deformation σ-w relation with a linear softening can be uniquely determined by three parameters: the tensile strength, f_{t}, the specific fracture energy, G_{f} and the initial stiffness, k_{init}, see Figure 4. The displacement values w_1 and w_2 may be determined through the following expressions:

$$w_1 = \frac{f_{\mathrm{t}}}{k_{\mathrm{init}}} \tag{18a}$$

$$w_2 = \frac{2G_{\mathrm{f}}}{f_{\mathrm{t}}} \tag{18b}$$

The initial stiffness should in theory be infinite, since no crack separation should occur until the tensile strength is reached. However, in practice this is rarely feasible due to problems with convergence. As such, k_{init} was instead chosen to be sufficiently large, such that the global load-displacement behaviour

Table 1: Elastic moduli [MPa] for birch and spruce.

		E_{L}	E_{R}	E_{T}	G_{LR}	G_{LT}	G_{RT}
Birch	Dinwoodie (2000)	16 300	1 110	620	1 180	910	190
Spruce	Dinwoodie (2000)	10 700	710	430	500	620	23

Table 2: Poisson's ratio [-] for spruce and birch.

		ν_{LR}	ν_{LT}	ν_{RL}	ν_{RT}	ν_{TL}	ν_{TR}
Birch	Dinwoodie (2000)	0.49	0.43	0.034	0.78	0.018	0.38
Spruce	Dinwoodie (2000)	0.38	0.51	0.03	0.51	0.025	0.31

was not affected.

In addition to the fracture behaviour, certain mechanical parameters also affect the global load-displacement response of the specimens. To determine which parameters had a large effect on the global response of the specimens, a sensitivity study was carried out and the only parameter that did display a large effect was E_{T}. All other elastic parameters had a negligible effect when varied within a reasonable range. The remaining stiffness moduli and Poisson's ratios were chosen based on the findings of the works of Dinwoodie (2000), and are presented in Tables 1 and 2. With this in mind, three parameters were subject to optimisation for the linear softening: the specific fracture energy, G_{f}, the tensile strength, f_{t}, and the elastic stiffness in the tangential direction, E_{T}.

2.4 Formulation of minimisation problem

For the linear softening introduced in Section 2.3, the optimisation problem can be formulated as

$$\begin{cases} \hat{\mathbf{x}} = & \operatorname{argmin} f(\mathbf{x}) \\ \text{s.t.} & w_2 > w_1 \end{cases} \tag{19}$$

where $\mathbf{x} = \{G_{\mathrm{f}}, f_{\mathrm{t}}, E_{\mathrm{T}}\}$ and the constraint will automatically be enforced due to the aforementioned formulation.

The choice of the cost function, $f(\mathbf{x})$, is often non-trivial in mathematical optimisation. In the

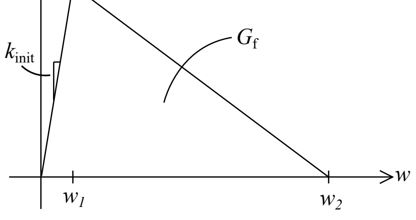

Figure 4: Stress-deformation relation with linear softening parametrised by f_{t}, G_{f}, and k_{init}.

present work, and in much of the previous work on inverse parameter estimation and FEMU (Bondsman & Peplow, 2024; De Moura et al., 2008; Do & Ohsaki, 2022; Dourado et al., 2008; Karandikar et al., 2022; Kuhn et al., 2022; Kunecký et al., 2024), some difference between the physical process and the FE model is minimised. A rather straight-forward choice, which often is used in FEMU, is the least square error between some experimental and numerical physical quantity. When the optimisation is carried out with respect to the global force-response, it is in the FEMU community often referred to as FEMU-F (Chen et al., 2024). Such a cost function may be formulated as follows:

$$f(\mathbf{x}) = \sum_{i=1}^{N} (P_{\text{num},i}(\mathbf{x}) - P_{\text{exp},i})^2 \tag{20}$$

where N is the number of discretisation points of the load-displacement response and $P_{\text{num},i}$ and $P_{\text{exp},i}$ are numerical and experimental force, recorded at discretisation point i. It is also common to introduce a modified version of the same cost function, such that

$$f(\mathbf{x}) = \sum_{i=1}^{N} \left(\frac{P_{\text{num},i}(\mathbf{x}) - P_{\text{exp},i}}{P_{\text{norm},i}} \right)^2 \tag{21}$$

where $P_{\text{norm},i}$ is some normalisation factor. The normalisation factor can for example be considered to be the point-wise standard deviation for the different discretisation points, or simply the measured force at the given discretisation points. For the former case, $P_{\text{norm},i} = \sigma_{\text{exp},i}$, and for the latter, $P_{\text{norm},i} = P_{\text{exp},i}$.

2.5 Reformulation of cost functions based on maximum likelihood theory

In statistical modelling, *likelihood-based inference* is a common approach to make predictions based on a certain set of observations that has been carried out. In such inference, the *likelihood*, is of central importance. The likelihood, denoted $L(\mathbf{x})$, is a function of the parameters, $\mathbf{x}$, of the statistical model, and conveys how likely different parameter values are to have generated the observed data. Computations are often performed using the log-likelihood, $l(\mathbf{x}) = \log L(\mathbf{x})$. If a statistical likelihood is defined, a point estimate of the parameters that yields the maximum value of the log-likelihood can be acquired through *maximum likelihood estimation* (MLE). This point estimate is denoted $\hat{\mathbf{x}}$. In addition, it is possible to assess the uncertainty in the optimal parameters through the so-called *observed Fisher information*, given that certain regularity conditions are fulfilled (Pawitan, 2013, Chap 2). The observed Fisher information is equal to the inverse of second derivative of the negative log-likelihood, evaluated at the MLE (Pawitan, 2013, Chap 8). The variance of the optimal set of parameters may now be formulated as

$$\mathbb{V}(\hat{\mathbf{x}}) = I(\hat{\mathbf{x}})^{-1} \tag{22}$$

where I is the observed Fisher information matrix:

$$I(\hat{\mathbf{x}}) = -\frac{\partial^2 l(\mathbf{x})}{\partial \mathbf{x}^2}\bigg|_{\mathbf{x}=\hat{\mathbf{x}}} \tag{23}$$

That is, given a reasonable assumption about the statistical model, it is also possible to reason about the uncertainty in the optimal set of parameters, through the Fisher information. To this end, we assume two different statistical models in order to model the observation error between the numerical and experimental load-displacement curves. The first model assumes the following observation error:

$$\epsilon_{ik} \sim \mathcal{N}(0, \sigma^2) \tag{24}$$

Here, ϵ_{ik} is the observation error in the i:th discretisation point, and describes the difference between the force from the FE-model and the force in the k:th experimental load-displacement curve, in the same discretisation point. Furthermore, the output from the FE-model in a specific discretisation point, s_i, is denoted $p(s_i; \mathbf{x})$, and is thus a function of the discretisation points for a given set of parameters $\mathbf{x}$. As such, it is assumed that the observation error is normally distributed with a zero mean, and constant standard deviation across all discretisation points. The log-likelihood of this observation model can thus be determined to:

$$l_1(\mathbf{x}) = -\frac{n_k n_i}{2}\log(2\pi) - \frac{n_k n_i}{2}\log\sigma^2 - \frac{1}{2\sigma^2}\sum_i (y_{ik} - p(s_i; \mathbf{x})) \tag{25}$$

Here, n_i is the number of discretisation points and n_k is the number of experimental load-displacement curves. Furthermore, the ML-estimate for the variance, σ^2, is (Casella & Berger, 2002, Chap 7):

$$(\sigma^2)^* = \frac{\sum_{ik}(y_{ik} - p(s_i; \mathbf{x}))}{n_i n_k} \tag{26}$$

which yields the following expression for the log-likelihood if additive terms in Equation 25 are ignored:

$$l_1(\mathbf{x}) = -\frac{n_k n_i}{2}\log\left(\sum_{ik}(y_{ik} - p(s_i; \mathbf{x}))^2\right) \tag{27}$$

The derivation of the second cost function is based on the following statistical model of the observation error:

$$\epsilon_{ik} \sim \mathcal{N}(0, \sigma_i^2) \tag{28}$$

The log-likelihood for this distribution is given by

$$l_2(\mathbf{x}) = -\frac{n_k n_i}{2}\log(2\pi) - \sum_i \frac{n_k}{2}\log\sigma_i^2 - \sum_i \frac{1}{2\sigma_i^2}\sum_k (y_{ik} - p(s_i;\mathbf{x})) \tag{29}$$

with the following ML-estimate of the variance, σ^2:

$$(\sigma_i^2)^* = \frac{\sum_k (y_{ik} - p(s_i;\mathbf{x}))}{n_k} \tag{30}$$

This in turn yields the following expression for the log-likelihood if the additive terms are ignored:

$$l_2(\mathbf{x}) = -\sum_i \frac{n_k}{2}\log\left(\sum_k (y_{ik} - p(s_i;\mathbf{x}))^2\right) \tag{31}$$

Here, n_i is the number of discretisation points of the load-displacement curves and n_k is the number of load-displacement curves. To maintain a minimisation problem we minimise the *negative* log-likelihood $-l(\mathbf{x})$, instead of maximizing the log-likelihood, $l(\mathbf{x})$. The negative log-likelihood is thus the cost function, previously defined as $f(x)$. For the rest of this paper, when we refer to the cost functions, we will refer to them as cost function l_1 and l_2.

As can be seen, neither of these log-likelihoods correspond directly to the most popular force-based cost functions in FEMU, see Equations 20 and 21. Consequently, the cost functions in Equations 20 and 21 are not proper likelihoods, and can thus not be assumed to properly recover the variance in experimental tests through the observed Fisher information. In contrast, given that the assumptions about the observation error in Equations 24 and 28 are accurate, they should yield a proper estimate of the variance. However, the assumptions that these cost functions are based on are most likely incorrect.

Equations 24 and 28 assume that the observed error is independently distributed. This is highly unlikely, since two different discretisation points located next to each other are likely to have a similar observed error. As such, Equation 24 is inaccurate due to the assumption of an independent and identical observation error regardless of discretisation point, and Equation 28 is inaccurate due to the assumption of independent observation errors. In addition, both cost functions are dependent on the degree of discretisation, through the summation over the discretisation index i. Despite these shortcomings, in the present work we adopt these common (but reformulated) FEMU cost functions, to evaluate the possibility to accurately capture the variance with them.

2.6 Bayesian optimisation in combination with FE-analyses

The optimisation procedure which minimises the cost functions has been implemented as a Python program to be used in conjunction with Abaqus (Dassault, 2019). A flow-chart of the entire optimisation procedure is shown in Figure 5. This flowchart is equivalent to the Algorithm presented in Algorithm 1. Initially, the following inputs have to be defined:

Table 3: Lower and upper bounds of the parameter domain for the optimisation procedure.

	f_t [MPa]		G_f [J/m^2]		E_T [MPa]	
	Lower	Upper	Lower	Upper	Lower	Upper
Spruce	1.0	5.0	100.0	500.0	100.0	500.0
Birch	2.0	14.0	200.0	1400.0	200.0	1400.0

- The number of function evaluations to be carried out during pre-sampling, before starting the BO procedure, denoted n_pre. In the present work, we have used $n_\text{pre} = 5$.
- The total number of maximum allowable iterations for the BO procedure, denoted n_max. In the present work, we have used $n_\text{max} = 100$.
- The allowable tolerance, ε_tol, according to Equation 17. In the present work, we have used $\varepsilon_\text{tol} = 1 \cdot 10^{-6}$.
- The acquisition function, $\alpha(\mathbf{x})$. In the present work, we have used the LCB function according to Equation 16, with $\beta = 3$.
- The lower bound, $\mathbf{x}_\text{min}$, and the upper bound, $\mathbf{x}_\text{max}$, i.e. the domain of interest. The lower and upper bounds used are shown in Table 3.

Following the inputs, the pre-sampling phase starts. In this phase, random combinations of the material parameters, within the allowable bounds, are sampled through latin hypercube sampling. For each sample, the cost function, and therefore also the finite element model, is evaluated. After the pre-sampling phase has finished, the BO procedure starts. The procedure starts by fitting a Gaussian process to the function evaluations observed thus far. This is carried out through the optimisation of the hyper-parameters of the GP through the log-likelihood described in Equation 15. Next, the posterior distribution, i.e. the mean and the variance in Equation 10a, of the GP is calculated. From the posterior mean and variance of the GP, the acquisition function, Equation 16, can be constructed. The next point to sample is then determined by minimising the acquisition function, which is carried out with the function *minimise* in SciPy. The cost function can then be evaluated in this point and subsequently added to the observations $\mathcal{D}$. The iteration count is increased and the procedure repeats either until convergence is acquired through Equation 17, or until the max number of iterations has been reached.

2.7 Estimation of posterior predictive distributions

After convergence has been reached, the following procedure is adopted to estimate the posterior predictive distributions for the parameters. First, the optimal set of parameters established in the optimisation procedure corresponds to the mean value of a normal distribution. Secondly, the variance of the parameters is computed with the observed Fisher information, Equation 23:

$$\mathbb{V}(\hat{\mathbf{x}}) = -\left(\frac{\partial l^2(\mathbf{x})}{\partial \mathbf{x}^2}\bigg|_{\mathbf{x}=\hat{\mathbf{x}}} \right)^{-1} \tag{32}$$

The estimation of the second derivative around the MLE, i.e. the Hessian matrix, was carried out by fitting a quadric surface to the points located around the minimum. Initially, 10 points were included in the fitting of the quadric surface. Points were then iteratively added to the fitting process until the covariance matrix became positive definite. Now, it should be noted that $\mathbb{V}(\hat{\mathbf{x}})$ is the uncertainty for the parameters based on all observed curves. The predictive uncertainty for a single curve is thus $n_k\mathbb{V}(\hat{\mathbf{x}})$. With this approach, the logarithm of the optimal set of parameters could for each series be assumed to be approximately normally distributed, such that

$$\log \mathbf{x} \sim \mathcal{N}(\log \hat{\mathbf{x}}, \Sigma_{\log \hat{\mathbf{x}}}),\ \ \Sigma_{\log \hat{\mathbf{x}}} = n_k\mathbb{V}(\hat{\mathbf{x}}) \tag{33}$$

where $\hat{\mathbf{x}}$ are the optimal parameters for each series shown in Table 4, $\mathbb{V}(\hat{\mathbf{x}})$ is the covariance matrix evaluated around the optimal set of parameters (Equation 32), and n_k is the number of experimentally obtained curves.

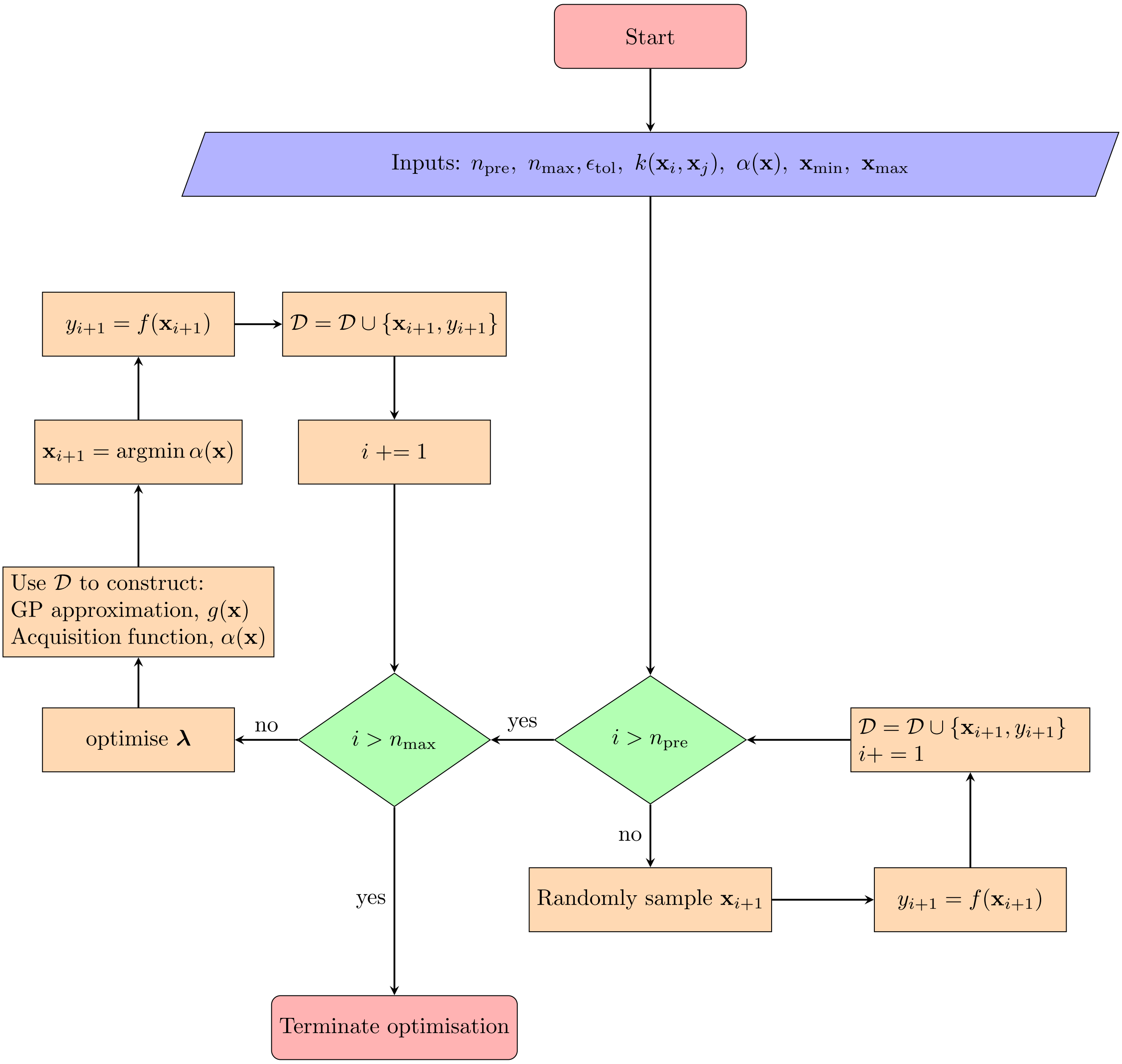

Figure 5: Flowchart of the parameter estimation procedure.

3 Results and Discussion

3.1 Effect of mesh discretisation

To ensure results independent of the finite element discretisation in the form of increment size and element size, a convergence study was carried out for the SENB specimens shown in Figure 2. For a convergence study of the 2d-models, the reader is referred to Jonasson et al. (2024a). For different increment sizes and element sizes, the error between the input specific fracture energy and the external specific work was determined as

$$\epsilon_{G_\mathrm{f}} = \frac{G_\mathrm{f,out} - G_\mathrm{f,inp}}{G_\mathrm{f,inp}} \tag{34}$$

where

$$G_\mathrm{f,out} = \frac{W}{A_c} = \frac{\int P(u)\ du}{A_c} \tag{35}$$

where W is the external work from the finite element model, A_c is the fracture surface, and $G_\mathrm{f,inp}$ is the specific fracture energy input to the model. Consequently, $G_\mathrm{f,out}$ and $G_\mathrm{f,inp}$ should be close to equal, given a sufficiently small element size. It should however be noted, that since the entire beam is loaded in bending, the beams' cross-section will be subject to both tensile and compressive forces, and as a consequence, some springs will be in tension and some in compression. This means that *at least* the very top row of springs will always be in compression for equilibrium to hold in bending. The springs in

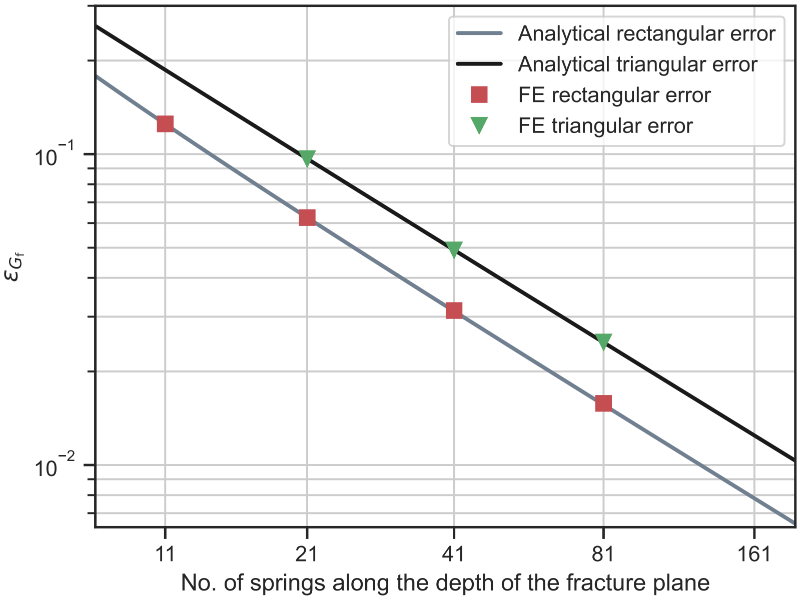

Figure 6: Convergence study of the mesh dependent error.

the top row will thus never dissipate any energy, since by definition, the springs are only dissipative in tension. The error from this model artefact was calculated analytically, and is shown in Figure 6 for the specimens with a rectangular fracture surface and a triangular fracture surface, respectively.

The numerical convergence study was carried out using five different element sizes, previously denoted b, in the fracture plane, see Figure 3: 2 mm, 1 mm, 0.5 mm, 0.25 mm and 0.125 mm. It is apparent that the error from the discretisation of the fracture surface follows the analytically calculated error well. In addition, the convergence appears to be quadratic in the number of springs along the fracture path, see Figure 6. The error is also larger for the specimens with a triangular fracture surface, which is a direct consequence of the different geometries. For the specimens with a triangular fracture surface, the springs that are never in tension makes up a larger relative part of the entire fracture surface, compared to the specimens with rectangular fracture surface.

3.2 Estimated fracture parameters

For both cost functions, l_1 and l_2, the optimisation was rather straight-forward and the optimal set of parameters was established in less than 100 iterations. The estimated parameters $(G_\mathrm{f}, f_\mathrm{t}, E_\mathrm{T})$ are presented in Table 4, for the two different cost functions. The specific fracture energy as acquired with the work-of-fracture method is also shown, for comparison.

In addition to the mean values, the uncertainty in the optimised parameters was assessed with the method described in Section 2.6. With this approach, approximate normal distributions were acquired for each cost function, and for each experimental series. From the two acquired distributions, 1000 samples were generated. Based on f_t and G_f from these samples, the corresponding stress-deformation (σ-w) relations could be calculated, together with the corresponding uncertainty. These relations are shown in the left column of Figures 7 and 8, for cost functions l_1 and l_2, respectively. For ten randomly selected (out of the 1000) relations, the corresponding global load-displacement (P-u) response was calculated. These ten global load-displacement curves are shown in comparison to the experimental load-displacement curves and envelopes in the right columns of Figures 7 and 8. As can be seen, some variance is captured in certain series: mainly for the spruce specimens with a rectangular fracture surface. However, for this series, the variability recovered is mostly centered around the peak load. The variability in the initial elastic part and the part where the load decreases are not matching the experimental variance well. For all other series, the variability is not recovered accurately.

As seen in Table 4, the tangential stiffness, E_T, of the spruce specimens ranges between 233 and 244 MPa, showing reasonable agreement regardless of cost function and regardless of notch geometry. Compared to previous studies, which report values between 420 and 430 MPa (Dahl, 2009; Dinwoodie, 2000; Ehrhart et al., 2015; Vasic, 2000), the values acquired in the present work are somewhat lower. However, this discrepancy is still within a reasonable range when considering the inherent, large variability in the constitutive behaviour of wood.

For the birch specimens, the values of E_{T} are slightly more scattered, both between series, and between cost functions. However, all values are relatively close to values reported by previous studies (Bartolucci et al., 2020; Dinwoodie, 2000; Engelhardt et al., 2024; Hörig, 1935), where the values range between 620 and 640 MPa. The difference in estimated E_{T} between the birch specimens with a rectangular fracture surface and a triangular fracture surface can in part likely be explained by the fact that only four to five birch specimens were extracted from the same original timber board, as reported in Jonasson et al. (2024a). In contrast, all spruce specimens were extracted from the same timber board. It is therefore reasonable that the scatter between series is larger for the birch specimens.

The estimated tensile strength, f_{t}, is quite similar between the two spruce series, ranging from 2.21 MPa up to 3.22 MPa. This is in relatively good agreement with previous studies that report values of 2.7 MPa (Forsman et al., 2020) and 2.8 MPa (Dahl, 2009). However, there is a large discrepancy in estimated tensile strength between the two cost functions. This is likely explained by the fact that the second cost function, l_2, assigns less weight to regions with high variance. The region around the peak-load is largely governed by the tensile strength. As seen in the global force-displacement responses in the right columns in Figures 7 & 8, the peak behaviour is always captured more accurately by the first cost function, l_1. This is also true for the birch series. This argument is also strengthened by the fact that the part close to zero load in the end of the global load-displacement curves are generally captured more accurately with cost function l_2, compared to cost function l_1. When the load approaches zero, the variance also decreases, and as such, this region is assigned more weight in cost function l_2.

The estimated fracture energy for the spruce specimens with a rectangular fracture surface is quite similar to the fracture energy acquired with the work-of-fracture method (Jonasson et al., 2024a). For cost function l_1, the fracture energy was estimated to be 8.5% less than when evaluated with the work-of-fracture method. For cost function l_2, the fracture energy was evaluated to 5.3% higher than with the work-of-fracture method. For the spruce specimens with a triangular fracture surface, the fracture energy was evaluated to 0.4% less with cost function l_1, and 4.7% higher with cost function l_2 compared to the estimated fracture energy with the work-of-fracture method. All values acquired for the fracture

Table 4: Estimated fracture parameters based on the FEMU method with two different cost functions, and the conventional work-of-fracture method.

	$l_1(\mathbf{x})$			$l_2(\mathbf{x})$			Work-of-fracture
	G_{f} [J/m^2]	f_{t} [MPa]	E_{T} [MPa]	G_{f} [J/m^2]	f_{t} [MPa]	E_{T} [MPa]	G_{f} [J/m^2]
Spruce rect	172	3.06	238	198	2.21	241	188
Spruce tri	256	3.22	233	269	2.38	244	257
Birch rect	747	8.37	761	789	6.56	735	700
Birch tri	700	7.39	551	735	4.49	656	611

energy for the spruce specimens are well in line with previous studies, which generally report values between 150 and 300 J/m^2 (Dourado et al., 2015; Forsman et al., 2020; Jonasson et al., 2024a; Reiterer, 2001; Reiterer et al., 2002; Stefansson, 2001).

For the birch specimens with a rectangular fracture surface, the fracture energy estimated with cost function l_1 is 6.7% higher than the fracture energy estimated with the work-of-fracture method. With cost function l_2, the fracture energy is estimated to be 12.7% higher than with the work-of-fracture method. For the birch specimens with a triangular fracture surface, the estimate is 20.3% higher with cost function l_1 in contrast to the work-of-fracture method, and with cost function l_2 it is estimated to be 14.6% higher than with the work-of-fracture method. This discrepancy, which is larger for the birch specimens, in contrast to the spruce specimens, might be a consequence of not loading the birch specimens to a sufficiently large displacement. The birch specimens were loaded with a total displacement of 7 mm, and at this point, the average birch series had a residual load of 1 N. It would however been unfeasible from a time perspective to load the specimens until a load of 0 N had been reached.

4 Conclusions

In this work, the fracture behaviour of Norway spruce and birch has been characterised using a FEMU framework in conjunction with Bayesian optimisation and experimentally obtained load-displacement curves from SENB specimens. Two commonly adopted cost functions in FEMU have been reformulated in the context of likelihood-based inference. Based on this reformulation, the possibility to recover the variance from the experimental load-displacement curves has been assessed. It is shown that neither cost function can accurately recover the variance due to the underlying assumptions in the statistical model being inaccurate. The main contributions of the present work are the following:

- Neither of the two commonly adopted cost functions in the context of FEMU, here denoted l_1 and l_2, can recover the variance in the experimental load-displacement curves.
- It is more difficult to recover the peak pehavior of the experimental load-displacement curves accurately with cost function l_2 compared to cost function l_1. This is a consequence of cost function l_2 assigning more weight to regions with low uncertainty.
- The fracture behaviour of Norway spruce and birch has been established through the characterisation of three important fracture parameters: E_T, G_f and f_t.
- As a consequence of establishing f_t and G_f for spruce and birch, the corresponding linear softening behaviour has also been established for both wood species.

Despite these contributions, there is still a lot of further work that has to be carried out in order to fully understand the fracture behaviour of birch. For example, it is only the specific fracture energy

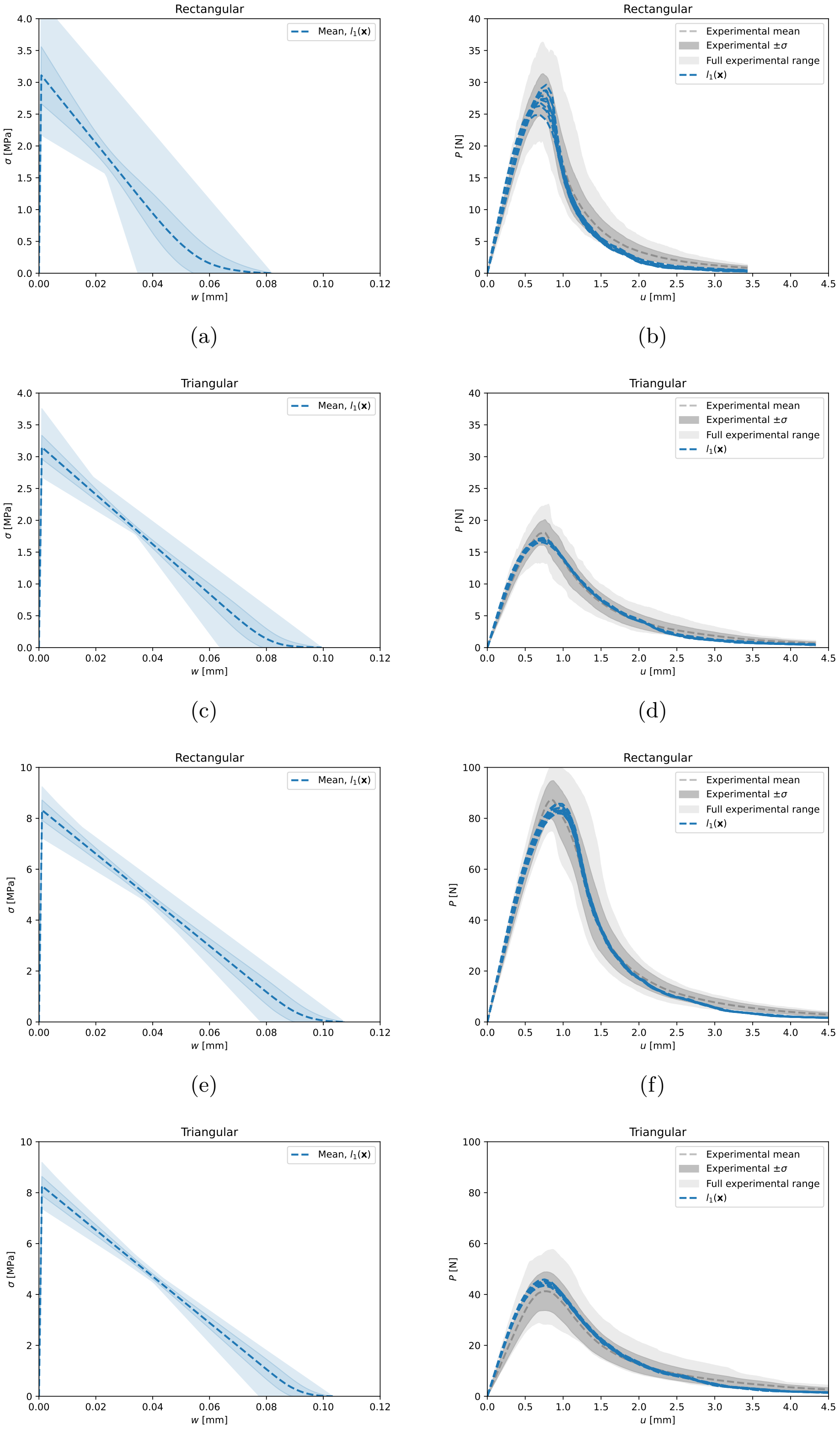

(a) (b)

(c) (d)

(e) (f)

(g) (h)

Figure 7: Linear softening behaviours for all experimental series (left column) based on estimated parameters with cost function l_1, and the corresponding global load-displacement curves in comparison to the experimental load-displacement curves (right column). Note that the scales of the axes are different.

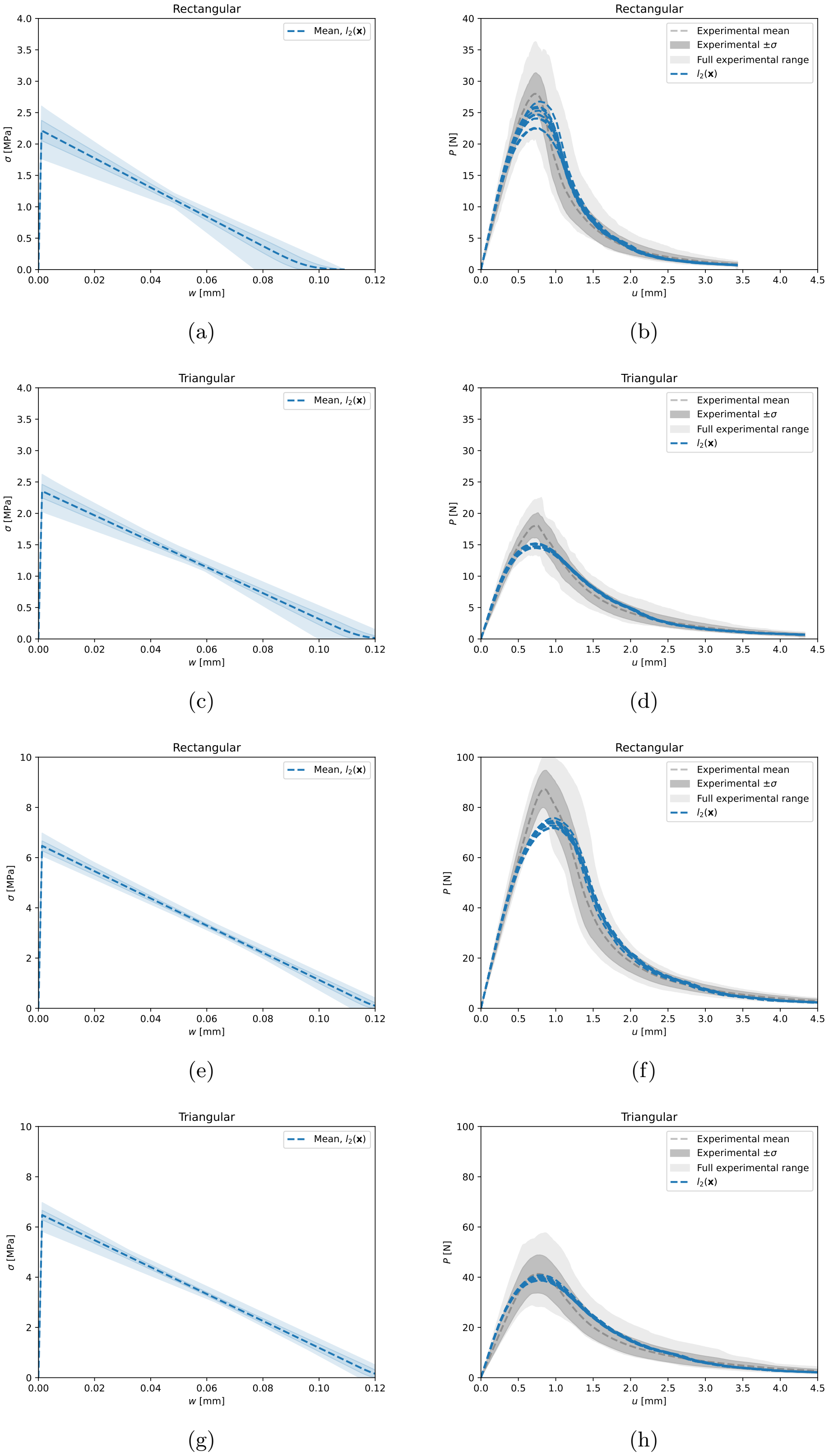

(a) (b) (c) (d) (e) (f) (g) (h)

Figure 8: Linear softening behaviours for all experimental series (left column) based on estimated parameters with cost function l_2, and the corresponding global load-displacement curves in comparison to the experimental load-displacement curves (right column). Note that the scales of the axes are different.

which has been experimentally validated in the present work. It would be greatly beneficial to further validate the procedure by experimentally validating all three parameters.

In the present work, only one crack propagation system (TL) and one mode of loading (mode I) has been considered. It would be of great benefit to establish the behaviour in more crack propagation systems, and other modes of loading.

It is also clear that neither cost function implemented in the present work can accurately recover the experimental variance. As such, formulating a cost function based on more accurate assumptions of the statistical model is necessary, in order to accurately assess the variance. If this is done, the approximate multivariate normal distributions acquired can be propagated to a structural or semi-structural level, where the fracture behaviour of load-bearing structures using birch can be properly assessed, and accounting for the natural variability inherent in wood.

Declarations

Acknowledgements – The financial support from FORMAS for the project Strenght and fracture analysis of laminated wood-based structural elements (grant 2023-01161), from the Nils & Dorthi Troëdsson foundation (grant number 1025/21), and from the Crafoord foundation is greatly acknowledged.

Contribution statement – Johannes Jonasson: Conceptualisation, Methodology, Software, Investigation, Validation, Writing - Original draft, Laboratory work. Johan Lindström: Conceptualisation, Methodology, Software, Investigation, Validation, Writing - Review. Henrik Danielsson: conceptualisation, Methodology, Investigation, Writing - Review and Funding. Erik Serrano: Conceptualisation, Methodology, Investigation, Writing - Review and Funding.

Conflict of interest – The authors declare no potential conflicts of interest with respect to the research, authorship, and/or publication of this article.

References

Aster, R. C., Borchers, B., & Thurber, C. H. (2013). *Parameter estimation and inverse problems*. Elsevier. https://doi.org/10.1016/C2009-0-61134-X

Bartolucci, B., De Rosa, A., Bertolin, C., Berto, F., Penta, F., & Siani, A. M. (2020). Mechanical properties of the most common European woods: A literature review. *Frattura ed Integrità Strutturale*, *14*(54), 249–274. https://doi.org/10.3221/IGF-ESIS.54.18

Bondsman, B., & Peplow, A. (2024). Inverse parameter identification and model updating for Cross-laminated Timber substructures. *Journal of Building Engineering*, *95*, 110209. https://doi.org/10.1016/j.jobe.2024.110209

Boström, L. (1992). *Method for determination of the softening behaviour of wood and the applicability of a nonlinear fracture mechanics model* [Doctoral Thesis, Division of Building Materials, LTH].

Casella, G., & Berger, R. L. (2002). *Statistical inference* (2. ed.). Duxbury.

Chen, B., Starman, B., Halilovič, M., Berglund, L. A., & Coppieters, S. (2024). Finite element model updating for material model calibration: A review and guide to practice. *Archives of Computational Methods in Engineering*. https://doi.org/10.1007/s11831-024-10200-9

Dahl, K. B. (2009). *Mechanical properties of clear wood from Norway spruce* [Doctoral thesis]. Norges teknisk-naturvitenskapelige universitet, Fakultet for ingeniørvitenskap og teknologi, Institutt for konstruksjonsteknikk. https://ntnuopen.ntnu.no/ntnu-xmlui/handle/11250/236422

Dassault. (2019). *Abaqus/cae*.

De Moura, M., Morais, J., & Dourado, N. (2008). A new data reduction scheme for mode I wood fracture characterization using the double cantilever beam test. *Engineering Fracture Mechanics*, *75*(13), 3852–3865. https://doi.org/10.1016/j.engfracmech.2008.02.006

Dinwoodie, J. (2000). *Timber - Its Nature and Behaviour*. CRC Press. https://doi.org/10.4324/9780203477878

Do, B., & Ohsaki, M. (2022). Bayesian optimization for inverse identification of cyclic constitutive law of structural steels from cyclic structural tests. *Structures*, *38*, 1079–1097. https://doi.org/10.1016/j.istruc.2022.02.054

Dourado, N., De Moura, M. F. S. F., Morel, S., & Morais, J. (2015). Wood fracture characterization under mode I loading using the three-point-bending test. Experimental investigation of Picea abies L. *International Journal of Fracture*, *194*(1), 1–9. https://doi.org/10.1007/s10704-015-0029-y

Dourado, N., Morel, S., De Moura, M., Valentin, G., & Morais, J. (2008). Comparison of fracture properties of two wood species through cohesive crack simulations. *Composites Part A: Applied Science and Manufacturing*, *39*(2), 415–427. https://doi.org/10.1016/j.compositesa.2007.08.025

Ehrhart, T., Brandner, R., Schickhofer, G., & Frangi, A. (2015). *Rolling Shear Properties of some European Timber Species with Focus on Cross Laminated Timber (CLT): Test Configuration and Parameter Study*.

Engelhardt, M., Gilg, H. A., Richter, K., & Sanchez-Ferrer, A. (2024). Adhesion-related properties of silver birch (Betula Pendula Roth) wood as affected by hydrophilic extraction. *Wood Science and Technology*, *58*(1), 379–402. https://doi.org/10.1007/s00226-023-01526-x

Forsman, K., Fredriksson, M., Serrano, E., & Danielsson, H. (2021). Moisture-dependency of the fracture energy of wood: A comparison of unmodified and acetylated Scots pine and birch. *Holzforschung*, *75*(8), 731–741. https://doi.org/10.1515/hf-2020-0174

Forsman, K., Serrano, E., Danielsson, H., & Engqvist, J. (2020). Fracture characteristics of acetylated young Scots pine. *European Journal of Wood and Wood Products*, *78*(4), 693–703. https://doi.org/10.1007/s00107-020-01548-3

Garnett, R. (2023). *Bayesian Optimization* (1st ed.). Cambridge University Press. https://doi.org/10.1017/9781108348973

Goulet, J. (2020). *Probabilistic machine learning for civil engineers*. MIT press.

Hörig, H. (1935). Anwendung der Elastizitätstheorie anisotroper Körper auf Messungen an Holz. *Ingenieur-Archiv*, *6*(1), 8–14. https://doi.org/10.1007/BF02086407

Jonasson, J., Danielsson, H., & Serrano, E. (2024a). Fracture energy of birch in tension perpendicular to grain: Experimental evaluation and comparative numerical simulations. *Wood Science and Technology*, *58*(5), 1925–1949. https://doi.org/10.1007/s00226-024-01595-6

Jonasson, J., Persson, P., & Danielsson, H. (2024b). Mitigating footfall-induced vibrations in cross-laminated timber floor-panels by using beech or birch. *Journal of Building Engineering*, *86*, 108751. https://doi.org/10.1016/j.jobe.2024.108751

Karandikar, J., Chaudhuri, A., No, T., Smith, S., & Schmitz, T. (2022). Bayesian optimization for inverse calibration of expensive computer models: A case study for Johnson-Cook model in machining. *Manufacturing Letters*, *32*, 32–38. https://doi.org/10.1016/j.mfglet.2022.02.001

Kuhn, J., Spitz, J., Sonnweber-Ribic, P., Schneider, M., & Böhlke, T. (2022). Identifying material parameters in crystal plasticity by Bayesian optimization. *Optimization and Engineering*, *23*(3), 1489–1523. https://doi.org/10.1007/s11081-021-09663-7

Kunecký, J., Štembera, V., Kloiber, M., Hataj, M., & Sebera, V. (2024). Optimization of CZM parameters of Norway spruce tested in mode I using multistart simplex method. *Engineering Fracture Mechanics*, 110430. https://doi.org/10.1016/j.engfracmech.2024.110430

Matérn, B. (1986). *Spatial Variation* (D. Brillinger, S. Fienberg, J. Gani, J. Hartigan, & K. Krickeberg, Eds.; Vol. 36). Springer. https://doi.org/10.1007/978-1-4615-7892-5

Mthembu, L., Marwala, T., Friswell, M. I., & Adhikari, S. (2011). Finite element model selection using Particle Swarm Optimization. In T. Proulx (Ed.), *Dynamics of Civil Structures, Volume 4* (pp. 41–52). Springer New York.

Nordtest. (1993). *Wood: Fracture energy in tension perpendicular to the grain.* (Standard). Nordtest.

Obernosterer, D., Jeitler, G., & Schickhofer, G. (2023). Birch for engineered timber products: Part II. *World Conference on Timber Engineering (WCTE 2023)*, 615–620. https://doi.org/10.52202/069179-0084

Pawitan, Y. (2013). *In all likelihood: Statistical modelling and inference using likelihood* (Paperback edition). Oxford University Press.

Persson, K., Gustafsson, P.-J., & Petersson, H. (1993). *Influence of Plastic Dissipation on Apparent Fracture Energy Determined by a Three-Point Beding Test*. Division of Structural Mechanics, LTH.

Rasmussen, C. E., & Williams, C. K. I. (2006). *Gaussian processes for machine learning*. MIT Press.

Raviolo, D., Civera, M., & Zanotti Fragonara, L. (2023). A Comparative Analysis of Optimization Algorithms for Finite Element Model Updating on Numerical and Experimental Benchmarks. *Buildings*, *13*(12), 3010. https://doi.org/10.3390/buildings13123010

Raviolo, D., Civera, M., & Zanotti Fragonara, L. (2024). A Bayesian sampling optimisation strategy for finite element model updating. *Journal of Civil Structural Health Monitoring*. https://doi.org/10.1007/s13349-023-00759-5

Reiterer, A. (2001). The influence of temperature on the mode I fracture behavior of wood. *Journal of Materials Science Letters*, *20*(20), 1905–1907. https://doi.org/10.1023/A:1012878312492

Reiterer, A., Sinn, G., & Stanzl-Tschegg, S. (2002). Fracture characteristics of different wood species under mode I loading perpendicular to the grain. *Materials Science and Engineering: A*, *332*(1-2), 29–36. https://doi.org/10.1016/S0921-5093(01)01721-X

Stefansson, F. (2001). *Fracture analysis of orthotropic beams: Linear elastic and non-linear methods* [Licentiate Thesis, Division of Structural Mechanics, LTH].

Thelandersson, S., & Larsen, H. J. (Eds.). (2003). *Timber engineering*. J. Wiley.

Tukiainen, P., & Hughes, M. (2013). The fracture behavior of birch and spruce in the radial-tangential crack propagation direction at the scale of the growth ring. *hfsg*, *67*(6), 673–681. https://doi.org/10.1515/hf-2012-0139

Tukiainen, P., & Hughes, M. (2016). The effect of temperature and moisture content on the fracture behaviour of spruce and birch. *Holzforschung*, *70*(4), 369–376. https://doi.org/10.1515/hf-2015-0017

Vasic, S. (2000). *Applications of Fracture Mechanics to Wood* [Doctoral Thesis, University of New Brunswick, Faculty of Forestry and Environmental Management].

Wang, T., Wang, Y., Crocetti, R., & Wålinder, M. (2022a). In-plane mechanical properties of birch plywood. *Construction and Building Materials*, *340*, 127852. https://doi.org/10.1016/j.conbuildmat.2022.127852

Wang, T., Wang, Y., Crocetti, R., & Wålinder, M. (2022b). Influence of face grain angle, size, and moisture content on the edgewise bending strength and stiffness of birch plywood. *Materials & Design*, *223*, 111227. https://doi.org/10.1016/j.matdes.2022.111227